Study on photoluminescence quantum yields of atomically thin-layered two-dimensional semiconductors transition metal dichalcogenides

Nur Baizura Binti Mohamed

Abstract

Study on photoluminescence quantum yields of atomically thin-layered two-dimensional
semiconductors transition metal dichalcogenides

by

Nur Baizura Binti Mohamed, Ph.D.

Kyoto University, Japan (2018)

Advisor: Professor Kazunari Matsuda

Atomically thin-layered two-dimensional (2D) transition metal dichalcogenides (TMDs) with chemical formula of MX_2 (M = Mo, W, Re; X = S, Se), have been attracted and stimulated the research interests due to their intriguing electronic and optical properties, after the discovery of an atomically thick carbon material of isolated graphene in 2004. In order to confront with the natural energy shortage in the world, the intensive efforts have been forced to fulfill the demands on the technological applications such as electronic and optical devices. The emergent new materials and their technological applications are strongly required to fulfil these demands. As emergent of semiconducting materials with direct band gaps, for instance, the atomically thin MoS_2, $MoSe_2$, WS_2 and WSe_2, as well ReS_2 with superior and divergence electronic and optical properties would have high potential for these requirements, while the graphene without a natural band gap has limitations towards the optoelectronic devices applications.

The optical properties of TMDs have dominated by bound electron-hole pairs by the Coulomb interactions (excitons), as a consequence of extremely large exciton binding energy of almost 1 eV. The large binding energy comes from strong quantum confinement of electron and hole in the atomically thin space and reduced dielectric screening in the atomically thin materials. The large binding energy enables the stable excitons even at room temperature. The novel enhanced light absorption and spin-valley coupling are caused by the band nesting and broken inversion symmetry of monolayer TMDs, are contributed to the excitons in the

atomically thin layered materials. The exciton related optical properties are very crucial to be investigated for understanding the light-matter interaction, for instance, the light emission quantum yield and radiative lifetimes of elementary excitation, in the atomically thin layered materials.

In this thesis, I have developed the quantum yield (QY) method to evaluate the photoluminescence (PL) quantum yield of atomically thin-layered material, using absolute and relative QY methods, with respect to the assigned organic reference dye, 3-borylbithiophene derivative. The PL QY method not only is a very crucial parameter to determine the efficiency and performance of semiconductor light-emitting devices, it is also a sensitive probe to identify the changes in electronic structure. Due to that fact, I apply this PL QY method to identify the nature of electronic band gap of rhenium disulfide (ReS_2) which has been debated to-date. Then, I extend the study to more wider information on physics and details structure of monolayer MX_2, M = Mo, W; X = S, Se TMDs by combining the PL QY and PL decay time of these material. By that reasons, the radiative lifetime of exciton in monolayer MX_2 TMDs can be understand in the basis of long radiative lifetime at low temperature limit, the finite coherence area of several square nanometers and the populations of dark exciton states.

The development of this PL QY method of atomically thin-layered material can be significance to the new thin-material with unknown nature of electronic band gap and the specific potential optoelectronic devices; as well as the obtained results of intrinsic physical value of monolayer TMDs are expected to contribute to understanding of physics in light-matter interaction scope and application of atomically thin-layered material for the next future development.

Table of Contents

Chapter 1. Introduction

1.1. Background

Nanoscience is a study of extremely small things which is from only 1 to 100 nanometers (nm) in scale, which deals particularly with an atom or a molecule, by science fields such as, physics, chemistry, biology, materials science and engineering. The concept of nanoscience was firstly introduced by a physicist, Prof. Richard Feynman on 1959. Then, Prof. Norio Taniguchi defined a term of nanotechnology on 1974 [1]. In relative to confront and strive for the energy crisis as well as environmental problems, the materials and their applications for the renewable energy and low consumption energy device based on the nanotechnology are totally indispensable.
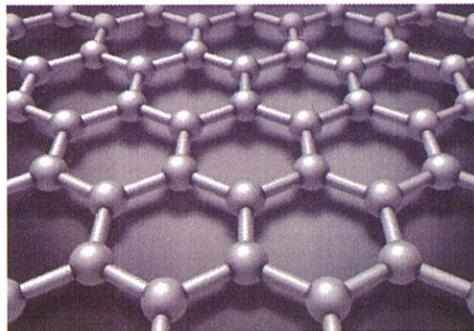
Figure 1.1 Structure of graphene.(Taken from wikipedia.com).

The discovery of graphene, as an one of the carbon-allotropes, which has intriguing and unique properties especially in quantum physics [2–8] has stimulate tremendous interests and researches in two-dimensional (2D) nanomaterials. It is expected that the behavior of electrons in their electronic transport in the 2D nanomaterials is much different from the conventional bulk materials due to the quantum effect. The 2D materials have promising potential candidates for nanoscale and flexible optoelectronic applications [9–14], photonics and energy storage [15–17]. Atomically thin-layered 2D semiconductors have attracted much interests from the view point of fundamental and potential application, after the advent and debut of isolated graphene exfoliated from bulk graphite using "scotch tape" method, by Andre Geim and Konstanstin Novoselov [2,18]. The isolated graphene is composed of a single layer of

carbon atoms bonded with a hexagonal structure, called the carbon honeycomb lattice with a sp^2-hybridized crystal structure [2,4] (Figure 1.1).
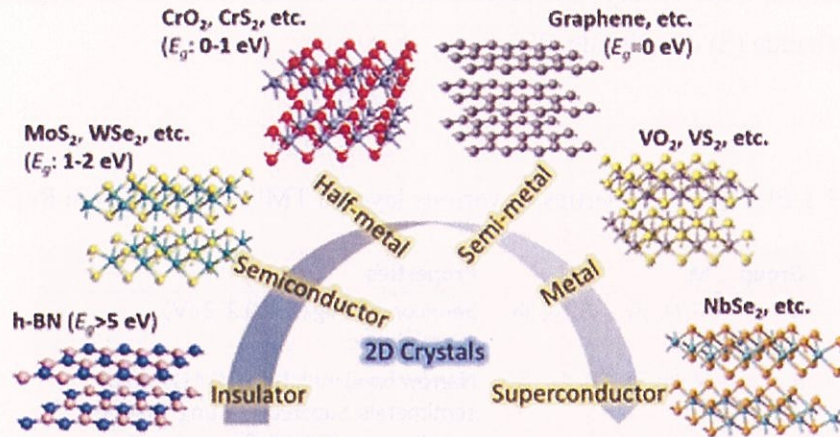
Figure 1.2 Variety of 2D crystals.(Taken from Ref. [19]).

Encourage from the emergence of graphene, other atomically thin-layered 2D crystals have been discovered and developed vigorously, for instance, hexagonal-boron nitride (h-BN) [20,21], transition metal dichalcogenides (TMDs)-e.g. MoS_2, WSe_2 [22–24], monochalcogenides-e.g. GeS, SnSe [25–27], black phosphorus (BP) [28,29] and so on. Figure 1.2 shows the classification of the atomically thin-layered materials as insulator, semiconductor, half/ semi-metal, metal and superconductor, depending on their energy band structures, with the energy gap, E_g of more than 5 eV, within $1 - 2$ eV and $0 - 1$ eV for insulator, semiconductor, and half/ semi-metal/ metal, respectively. These 2D layered materials have wide range of electronics band gap, various transparent properties, bio-compatibility [19] along with their own specific features, thus offer the variety of potential applications due to their attractive properties.

In particular, the family of atomically-thin layered 2D semiconductors TMDs materials consists of 40 different compounds with a chemical formula of MX_2, (M = Mo, W, Hf, Nb; X = S, Se, Te), where M and X represent of transition metal and chalcogen group, respectively. Table 1.1 exhibits 5 different groups of TMDs (group IV (4) – X (10)) with their electronic properties including the energy band gap (E_g), energy band structure, electrical conductivity, ρ

and magnetic properties. Most of them are semiconductor material with different band gap, and their magnetic properties is vary with regards to the combination of the chalcogen atom either sulfide (S), selenide (S) or telluride (Te).

Table 1.1 Electronic properties of various layered TMDs. (Taken from Ref. [16]).

Group	M	X	Properties
4	Ti, Hf, Zr	S, Se, Te	Semiconducting (E_g = 0.2~2 eV). Diamagnetic.
5	V, Nb, Ta	S, Se, Te	Narrow band metals (ρ ~10^{-4} Ω.cm) or semimetals. Superconducting. Charge density wave (CDW). Paramagnetic, antiferromagnetic, or diamagnetic.
6	Mo, W	S, Se, Te	Sulfides and selenides are semiconducting (E_g ~1 eV). Tellurides are semimetallic (ρ ~10^{-3} Ω cm). Diamagnetic.
7	Tc, Re	S, Se, Te	Small-gap semiconductors. Diamagnetic.
10	Pd, Pt	S, Se, Te	Sulfides and selenides are semiconducting (E_g = 0.4 eV) and diamagnetic. Tellurides are metallic and paramagnetic. $PdTe_2$ is superconducting.

ρ, in-plane electrical resistivity.

Group VI (6) layered TMDs have leading the research demands [10,15,30–32] due to their unique optical properties, such as direct band-gap semiconductor of its monolayer, with relatively intense photoluminescence (PL), instead of indirect band-gap semiconductor for their bulk counterparts [22,33]. These atomically thin layered materials were held together by strongly covalent bonded for their intra-layer (in-plane) atoms, but relatively weak van der Waals interaction between their consecutive adjacent layers [19,34]. This makes them easily cleave micromechanically from their bulk materials [18]. The atomically thin layered materials are identified by employing the combination measurements such as optical microscopy, Raman and PL spectroscopy, atomic-force microscopy and scanning electron microscopy [35–40].

In contrast to the family of TMDs, a member from the group VII TMDs was known to have anisotropic in-plane crystal structure and shows the anisotropic optical properties. Currently, Rhenium dichalcogenides, ReX_2 (X = S, Se) were extensively re-introduced to the research fields [41–47] due to their atomically thin-layered properties, instead of their bulk's

characters a few decades ago [48–56]. A reduced symmetry with distorted 1-Trigonal (1-T) structure [50,57] makes ReX_2 show the anisotropic optical responses, and hence offers potential applications on polarization-sensitive photodetectors and so on [44,45,56,58–61].

1.2. Motivation

Graphene is an attractive material, which this material has been reported to be a strongest material ever measured [62] and has high electron mobility ~ 10 000 $cm^2V^{-1}s^{-1}$ [2]. Unfortunately, graphene with lack of band gap in the core atomically thin-layered two-dimensional (2D) materials is not applicable for potential application of transistor and optical devices [63–66]. It is necessary to find other layered 2D materials with a finite band gap in order to fulfill deficiency of these properties. The transition metal dichalcogenides (TMDs) are foreseen to reciprocate the inadequacy currently.

The TMDs have proved to be the direct band-gap semiconductors in the thinnest monolayer limit [22,33]. The direct band-gap consequently enhances the optical transitions and light emission (luminescence) in the material. The luminescence efficiency defined as luminescence quantum yield is very crucial for technological applications such as light emission devices [67]. The strong Coulomb interaction between electron-hole pair results the formation of tightly bound exciton in this material, and the excitons contribute to the enhancement of oscillator strength in the system [31,68,69]. Despite owing to the direct band gap and large exciton binding energies [70,71], the quantum yield of as-exfoliated TMDs have been reported to range only 0.01 – 6 % [10,12,72–74] due to high defect states densities and large nonradiative recombination rates [33,74,75]. The luminescence quantum yield for the direct band gap semiconductor materials, along with the understanding how the luminescence reduction have been forced much more works of this TMDs.

The PL quantum yield which defines as the ratio of emitted photon numbers to the absorbed photon numbers, is a crucial parameter to determine the performance and efficiency of a semiconductor light-emitting devices, also a sensitive probe to the change in electronic structure. So the nature of the electronic band gap can be identify accordingly by this method.

1.3. Objectives of Study

In this thesis, I have studied the novel optical properties of atomically thin TMDs (MoS_2, $MoSe_2$, WS_2, WSe_2, and ReS_2) by photoluminescence (PL), Raman scattering, and differential reflectance spectroscopy [76,77]. I have focused the study on:

1. Develop a new PL quantum yield evaluation method specifically for atomically thin-layered material using both absolute and relative QY methods with respect to the assigned organic reference dye of 3-borylbithiophene derivative.

2. Apply the developed method of PL QY on thin-layered material to identify the electronic band gap nature of atomically thin-layered rhenium disulfide (ReS_2).

3. Combining the information on PL QY and PL decay of monolayer MX_2 (M = Mo, W; X = S, Se) TMDs to investigate the intrinsic physical value of exciton radiative lifetime and understand the details electronic structure of these materials.

1.4. Significance of the Study

The PL quantum yield of usual molecules and solutions are not suitable to be used to determine the PL QY of atomically thin-layered material, due to very small target of the sample in the range of less than micrometer length, and the low PL QY values as a results from high defect densities of this semiconductor material. Therefore, the new developed method to evaluate the PL QY of thin-layered material will be significance to a new thin-layered material with unknown and unclear electronic structure to determine their specific potential application as light-emitting device or long-range photodetector as a consequences from direct or indirect band gap semiconductor, respectively. Moreover, the information on intrinsic value such as exciton radiative lifetime of a semiconductor material, is critical to the physical understanding behind the phenomena happen and the special features own by the material itself. Thus, the next development and enhancement in optoelectronic device performance can be achieved and realized.

1.5. Thesis Outline

This chapter will be follow by Chapter 2, in which all the fundamental and literature reviews are introduced. In Chapter 3, I explain the method to evaluate the PL QYs of one of

the monolayer TMDs, WSe$_2$ using both absolute and relative QY method employing an assigned reference dye of 3-Borylbithiophene derivative. The exciton radiative lifetimes of TMDs are investigated in Chapter 4. In Chapter 5, the PL QYs as well as the indirect band gap nature of layered ReS$_2$ are studied. As a summary, a conclusion and outlook for future research works are provided in Chapter 6.

Chapter 2. Literature Review

2.1. Basics of Optical Properties

Nanomaterial sciences dealing with the structure on to the nanometer (nm), must be considered to the quantum mechanics, in which describe the electron as a particle and wave, called as wave-particle duality. As an overall knowledge, the electron behaves as a particle in classical physics, whereas behaves as a wave in the nano-scale structure, that only can be explained by quantum physics [78]. In the following sub-chapter, I will briefly explain the important terms involved in the fundamental physics of solids, and its advance in this study.

2.1.1. Electronic Band Structure and Effective Mass

Since the main topic in this thesis is related to the nanomaterial, thus I intentionally connected to the formalism of quantum mechanics. The total energy (E_{total}) of an electron is the sum of its potential and kinetic energies. In classical physics, the relationship will be expressed as Eq. 2.1:

$$E_{total} = \left(\mathbf{p}^2/2m\right) + U(\mathbf{r})$$ Eq. 2.1

where $U(\mathbf{r})$ describes the local potential energy of the particle at position $\mathbf{r}$ and the kinetic energy is given by the classical expression $E_{kinetic}= \mathbf{p}^2/2m$ in which m is the particle mass and $\mathbf{p}$ is the momentum [79]. From the requirement for conservation of energy and momentum, the electronic state is defined by "quantum numbers," as shown in Figure 2.1. Each set of quantum numbers results in a set of "wave functions", which describes the probability of finding an electron around a given location at a given time [79]. The principal quantum number (n) in Figure 2.1 determines the energy level occupied by the electron, and n is denoted as integral values of 1, 2, 3, etc. The l and m in Figure 2.1 are the Azimuthal and magnetic quantum number that indicates as the shape and orientation of orbitals in space, respectively, in which l can be denoted as "0 to n–1", and the m can take values from "l to $-l$", whereas the s, p, d, and f is the energy sublevel relates to the different orbitals [80].
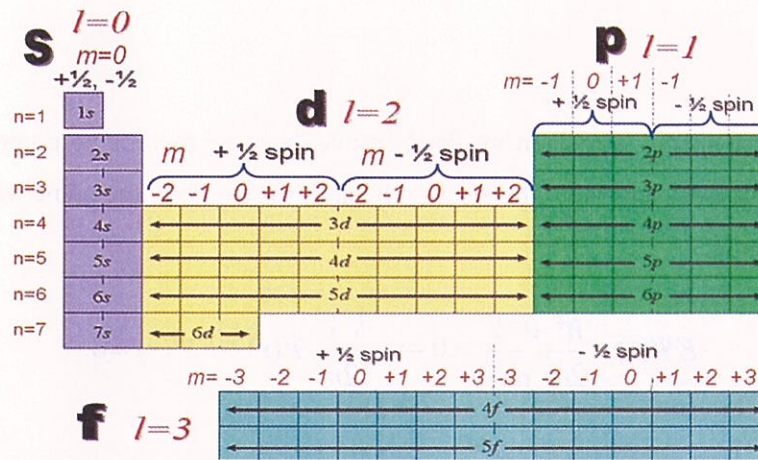
Figure 2.1 The quantum numbers, n (and angular momentum) relative to the elements in the periodic table. (Taken from www.upsc_quantumnumbers.youtube).

In principle, it is impossible to exactly measure the position (x) of an electron at a specific time (t), velocity (v) and energy (E) using the classical physics. Thus, only the way to determine all these things is the Heisenberg uncertainty principle [81], as denote by the Eq. 2.2 and Eq. 2.3 below:

$$\Delta x \Delta p \geq h \qquad \text{Eq. 2.2}$$

$$\Delta E \Delta t \geq h \qquad \text{Eq. 2.3}$$

where $\hbar = h/2\pi$, h is Planck's constant. To deals with this uncertainty, the particle should be described by a probability distribution (its wave function) using the fundamental equation of physics for describing quantum mechanical behavior, in the framework of Schrödinger equation [82] as below [79]:

$$i\hbar \frac{d\Psi}{dt} = -\frac{\hbar^2}{2m}\nabla^2 \Psi + U(\mathbf{r})\Psi \qquad \text{Eq. 2.4}$$

$$E\Psi(\mathbf{r}) = (-\frac{\hbar^2}{2m})\nabla^2 \Psi(\mathbf{r}) + U(\mathbf{r})\Psi(\mathbf{r}) \qquad \text{Eq. 2.5}$$

where Ψ is wavefunction, and ∇^2 is referred as the Laplacian and is the second spatial derivative of the function it operates on the wave function in this case.

In the 'free space', the electrons freely move, because there is no potential ($U(\mathbf{r}) = 0$) affecting the motion of electrons. The electron behavior is called as the plane wave [83]. Thus, Eq. 2.5 will become:

$$E\Psi(\mathbf{r}) + \frac{\hbar^2}{2m}\frac{d^2\Psi}{dx^2} = 0 \rightarrow -\frac{\hbar^2 k^2}{2m}\Psi(\mathbf{r}) + E\Psi(\mathbf{r}) = 0 \qquad \text{Eq. 2.6}$$

thus

$$E = \frac{\hbar^2 k^2}{2m} \qquad \text{Eq. 2.7}$$

The r is known as eigenvector of Eq. 2.6 and the energies E are the eigenvalues. The momentum of this wave is $p = \hbar k$, where k represents the electron momentum within a factor of $\hbar$ [84] and The electron energy has a parabolic dispersion with respect to k. Figure 2.2 shows the E-k diagram of electron in absence of a periodic potential (electron in "free-space").
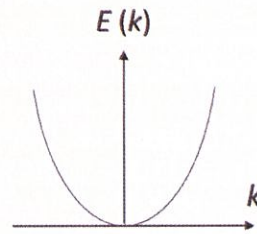
Figure 2.2 *E-k* diagram of electrons in "free-space".

In real world, the motions of electron are never free, because of the Coulomb attraction between the proton (positive) in the nucleus and the electrons (negative) [85]. Also in a solid, the atoms are being apart with a regular spacing, and the spacing is called the translational vectors of Bravais lattice [84]. The periodic potential has the property of

$$U(\mathbf{r}) = U(\mathbf{r} + \mathbf{R}) \qquad \text{Eq. 2.8}$$

where $\mathbf{R}$ is any Bravais lattice translation vectors [86,87]. So, the Eq. 2.5 of Schrödinger equation is modified to [87],

$$E\Psi(\mathbf{r}) = \left[-\frac{\hbar^2}{2m}\nabla^2 + U(\mathbf{r}) \right]\Psi = H\Psi \qquad \text{Eq. 2.9}$$

where H in Eq. 2.9 is denoted as the Hamiltonian operator. The eigenfunctions of electrons inside the bands, show that the electrons behave as a form of Bloch wave (Bloch

theorem) [79,83]. The Bloch theorem leads to a description of the electronic energy levels in a crystal (periodic potential) in terms of a family of continuous functions $E_n(k)$ with each continuous band indexed by n and having the periodicity of the reciprocal lattice [87], called Brillouin zone.

When the numerous numbers of atoms form the crystal lattice, the energy levels will split to the number of states and forms the energy "bands", as exhibit in Figure 2.3. There are no energy band states between the electron occupied and unoccupied bands as the forbidden energies. The energy difference between the electron occupied and unoccupied bands are referring to band gap, E_g which will determine whether a material is metal, semiconductor or insulator [85].
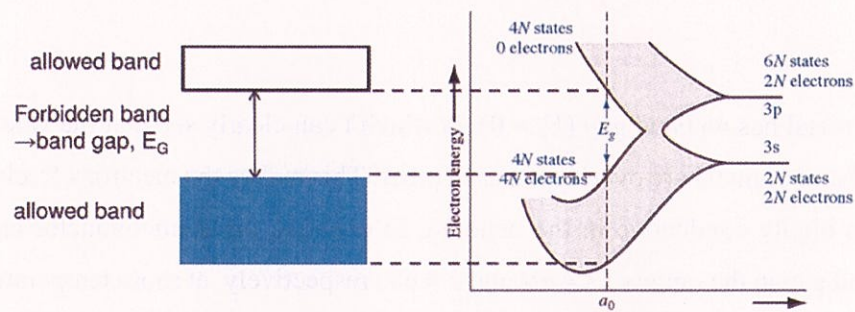
Figure 2.3 Energy dispersion curve of electrons, with the actual band structure calculated from the Schrödinger equation by solving for a crystal to get a complex series of allowed energy states according to the crystal momentum (k), with lattice constant (a) and series number of states (bands) (N). (Taken from Ref. [88]).

2.1.2.   Metal, Semiconductor and Insulator Materials

The classification of a material to be either metal, semiconductor or insulator is depends on the size of band gap and the number of electrons in the outermost band (conduction band) [85]. Figure 2.4 shows the typical band structures at absolute zero temperature ($T = 0$ K), with the dashed region denotes as filled band. The VB (CB) is valence (conduction) band, and E_g is an energy gap, defined as the energy difference between the valence band (occupied band) and conduction band (unoccupied band).
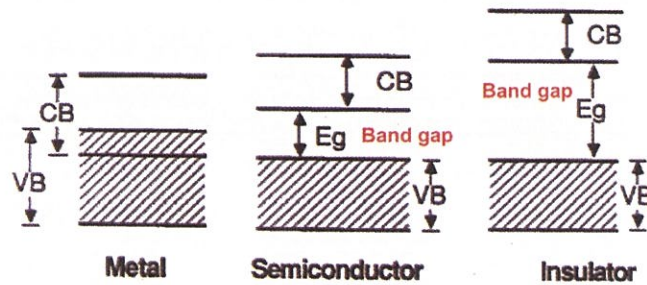
Figure 2.4 Types of materials; metal, semiconductor and insulator, at T = 0 K. Dashed region denote as occupied energy band. (Taken from Ref. [89]).

The metal has no band gap ($E_g = 0$), in which I can clearly see that the valence and the conduction band of metal are overlapped each other. This makes the electrons freely and easily mobile, thus highly conductive in the material. In contrast, the semiconductor and insulator have the band gap in the range of < 4 eV and > 4 eV, respectively, at room temperature [85,89]. The additional energy is required to excite the electrons to the unoccupied states to overcome the band gap in the semiconductors and insulators. In the insulators, the larger energy is required to excite the electrons from valence to conduction band, while obeying the Pauli Exclusion Principle (strictly one state for one electron) [90].

2.1.3.   Density of States (DOS) and Quantum Confinement

Heisenberg uncertainty principle is applicable to describe the natures of considerably small scale object or crystal depending on the size and dimensionality, as a consequence of the quantum confinement effect [36,89]. The electronic density of states (DOS) corresponds to the number of states per unit volume per unit energy interval; $g(E) = (1/V)(dN/dE)$, where V is a volume, dN is the number of electron quantum states within the energy interval, dE. According to the relation of $E = p^2/2m$ (classical physics) for potential energy in Eq. 2.1 and the Heisenberg uncertainty principle of Eq. 2.2, the E is referring to the confinement energy $E_{confinement}$ according to quantum mechanics. $E_{confinement}$ will be described as [91,92],

$$E_{confinement} = \frac{(\Delta p_x)^2}{2m} \sim \frac{\hbar^2}{2m(\Delta x)^2}$$

Eq. 2.10

where m is a mass of electron. If the confinement energy is comparable or larger than the kinetic energy of particle due to the thermal energy of $\frac{1}{2} k_B T$. The Eq. 2.10 becomes

$$\Delta x = \sqrt{\frac{\hbar^2}{m k_B T}}$$

Eq. 2.11

From Eq. 2.11, if Δx corresponding to the size of system is smaller than 10 nm at room temperature ($T = 300$ K), with an electron effective mass, $m^* = 0.1\ m_0$ (m_0 is electron rest mass), the quantum confinement effects become significant. Thus, in the atomically thin-layered materials with a thickness of less than 1 nm, the quantum confinement effect becomes extremely prominent for the electrons.

Figure 2.5 shows the dimensionality reduction for the semiconductor systems from 3D for bulk, to 0D for quantum dot, and the DOSs in each dimension are also shown. For the 3D system such as a bulk semiconductor, the DOS is proportional to the squared root dependence of $E^{1/2}$, while that in the 2D system shows a step-like DOS, as define by Eq. 2.12 and Eq. 2.13, respectively. Those in the quantum wires (1D) and dots (0D) exhibit the divergence and δ-function like DOS [89].

$$N(E) = \left(\frac{1}{2p^2}\right)\left(\frac{2m^*}{\hbar^2}\right)^{3/2} \sqrt{E}$$

Eq. 2.12

$$N(E) = \left(\frac{m^*}{p\hbar^2}\right)$$

Eq. 2.13
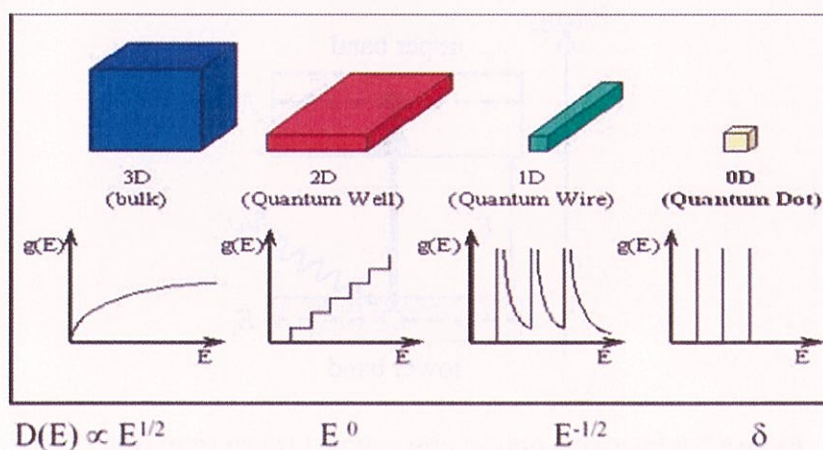
Figure 2.5 Reduction of dimensionality from the 3D (bulk) to 0D (quantum dot) of semiconductor systems, with the relation of the density of states (DOS) to the confinement energy. (Taken from Ref. [89]).

2.1.4.   Optical Transition

Optical transition in a solid corresponds to the excitation of electrons from band-to-band, so called interband transition, and can be explained by optical transition of interband absorption or interband luminescence, discussed as follow:

Interband Optical Absorption (Absorption)

The physical meaning of the absorption process is that an absorption of electromagnetic (EM) radiation occurs during the propagation of light, when the frequency of light is resonant with the transition frequency of electronic states in the material. In this case, the light will be attenuated as it progresses due to the absorption of photons by the materials [91].
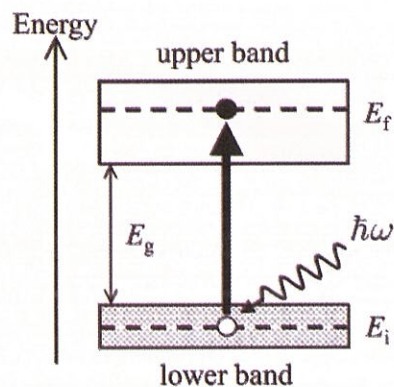
Figure 2.6 Interband optical absorption. (Taken from Ref. [91]).

Figure 2.6 shows the energy band diagram with two distinct bands; the upper band (E_f) – conduction band, and the lower band (E_i) – valence band, which is separated apart by the energy gap (E_g). By considering the energy and momentum conservation, the interband absorption of band-edge transition is described that an electron is excited to the conduction

band, by absorbing an incoming photon ($\hbar\omega \geq E_g$), thus left a hole at the valence band. This optical transition creates an electron-hole pair, called as exciton. This exciton (bound electron-hole pair) is an important quasiparticle, which strongly affects the optical properties of a semiconductor [91].
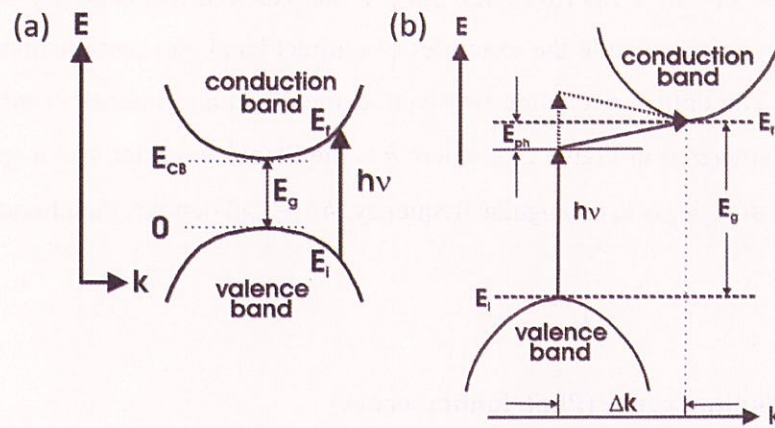

Figure 2.7 Direct and indirect band gap optical transition. (Taken from Ref. [93]).

	Direct bandgap	Indirect bandgap
Energy conservation	$E_f = E_i + hv$	$E_f = E_i + hv \pm E_{ph}$
Momentum conservation	$k = k_i = k_f$	$k_f = k_i + k_{ph}$

$E = \dfrac{hc}{\lambda} = hv = \hbar\omega \, ; \, \hbar = h/2\pi$	$E_g = E_f - E_i$	$\pm E_{ph} = $ (+) Phonon absorption
	$\Delta k = k_f - k_i$	(-) Phonon emission

Figure 2.8 Optical excitation process in the direct and indirect band gap transition (With f and i denote as final and initial).

Figure 2.7 show the two kinds of interband optical transitions which are direct and indirect band gap of semiconductors, with the y- and x-axis denote the energy (E) and momentum space (k). The direct band gap transition can only be realized if the conduction band minimum (CBM) and valence band maximum (VBM) are located at same momentum, k in the Brillouin zone as shown in Figure 2.7(a), thus described as $k = k_i = k_f$ (Figure 2.8), whereas the indirect band gap transition is involving by VBM and CBM with different location in k, thus denoted as Δk, as shown in Figure 2.7(b). The indirect band gap transition is governed by the

optical transition accompanied with phonon-assisted process, i.e. either phonon absorption or phonon emission to fulfill the momentum conservation, thus the conservation of energy is expressed as $E_f = E_i + hv \pm E_{ph}$ (in Figure 2.8). Examples of direct band gap semiconductors are GaAs, InP, and InAs, while the examples of indirect band gap semiconductors are Si, Ge and AlAs [93]. The optical excitation involved in the direct and indirect band gap transition processes is summarized in Figure 2.8, where h is the Planck constant, c is a speed of light, λ is a wavelength of light, ω is an angular frequency, hv $(=E_{ph})$ denotes the phonon energy.

Interband Luminescence (Photoluminescence)

Interband luminescence is the reverse process of the interband optical absorption, where an excited electron in the conduction band decays to the valence band, thus emitted a photon corresponding to the E_g. This process causes the reduction in number of electrons in the conduction bands and holes in the valence band, hence corresponds to the annihilation of electron-hole pair, known as radiative recombination of electron-hole pair [91]. Luminescence can occur on several processes, however, here I focusing on the photoluminescence (PL) process, i.e. re-emission of photon (light) after absorbing a photon by photoexcitation [91].
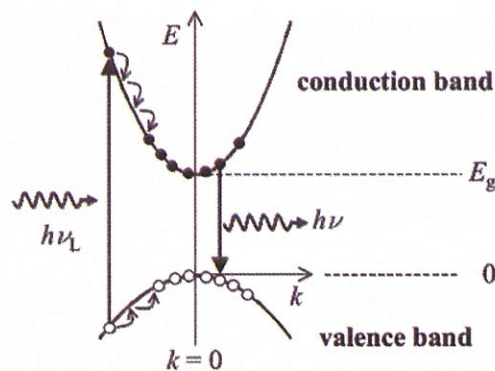

Figure 2.9 Schematic diagram of photoluminescence process in a direct band gap semiconductor. (Taken from Ref. [91]).

The physical processes containing in PL are more complicated than those of absorption, since the PL process is affected by the various energy states, such as impurity and defect state,

and so on. Here, for briefly understanding of the physics concept of PL, I describe simple mechanism with only two bands, the conduction and valence band as shown in Figure 2.9.

The electron in the valence band will be excited to the conduction band, by absorption of the energy of incoming light with hv_L, which is larger than the band gap energy, E_g. The electron in the conduction band will be in the higher energy state of the conduction band, but not stable for long time. The electron then quickly loses its excess energy by emitting phonon within several-hundred femtosecond timescale, and these steps can be seen as cascade of transitions within the conduction band, and still obeyed the laws of energy and momentum conservation [91]. After being in the lowest state in the conduction band, the electron will relax to valence band and recombined with the hole within nanosecond timescale, hence emitting a photon, hv. The rate of decay transition will be described in the next sub-chapter (2.1.6) of radiative lifetime.

2.1.5.   Quasiparticles (Exciton, Trion, and Biexcitons)

The concept of excitation waves in a crystal and a term of "exciton" were firstly introduced in early 1930 (1931-1936) by the Russian theorist Yakov Frenkel, and then invented further by the Swiss physicist Gregory Hugh Wannier and the English theorist Sir Nevil Francis Mott in the end of 1930s [79].
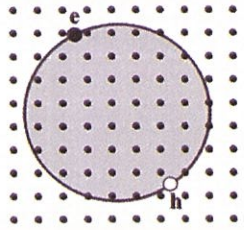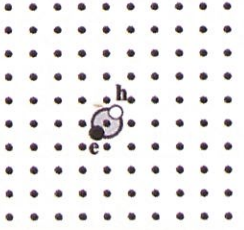
Figure 2.10 Exciton: electron-hole pair with a stable orbit around each other.

An exciton is electron (negatively charged particle) and hole (positively charged particle) pair bound by mutual Coulomb interaction between each other. The exciton can be viewed in the simplest picture of small hydrogenic system, in which the electron and hole are bound in a stable orbit around each other, as shown in Figure 2.10 [91,94]. Absorption of photon in interband absorption process creates an electron and hole in the conduction and valence band, respectively, and the oppositely charged particles can only be formed and

satisfied if the gradient of the conduction and valence band are at the same point of the Brillouin zone where the transition occurs, and have exactly same group velocities, $v_e = v_h$ [91].

There are two types of excitons, namely as Wannier-Mott and Frenkel excitons. The Wannier-Mott exciton is also called as free exciton and freely moving in the crystal, where the average distance between the bind electron and hole are much larger than the inter-atomic spacing, thus the binding energy for this exciton is only a few meV, which will be described after. In contrast, the Frenkel exciton is a tightly-bound exciton, which has very small distance between bound electron and hole, and smaller exciton size. The small exciton size causes the large binding energy with the range of several hundreds of meV. The difference between the two-types is summarized in Table 2.1

Table 2.1 The differences between Wannier-Mott and Frenkel excitons.

Wannier-Mott Excitons	Frenkel Excitons
• Schematic diagram: **Free exciton**	• Schematic diagram: **Tightly bound exciton**
• **Delocalized** – move freely throughout the crystal	• **Localized** – propagate through crystal by hopping from atom site to site
• **Large radius** – average separation of the electrons and holes much greater than interatomic spacing	• **Very small radius** – comparable to the interatomic spacing
• **Small binding energy** ~ few meV	• **Large binding energy** ~ hundreds meV (0.1 – several eV)

The radius of the exciton related to the inter-particle spacing, usually called exciton Bohr radius (a_B), is define as Eq. 2.14 [91,94]:

$$a_B = \frac{\hbar^2 \varepsilon}{\mu e^2}$$

Eq. 2.14

where ε and μ are the background dielectric constant and reduced mass of electron and hole, respectively, and e is the electron charge. The exciton binding energy (E_{bn}) with its quantum number, n is referring to the total energy used to separate the exciton into its constituent parts; one electron and one hole can be express in Eq. 2.15, Eq. 2.16 and Eq. 2.17,

$$E_{bn} = \frac{E_{b0}}{n^2}$$ Eq. 2.15

$$E_{xn} = E_g - E_{bn}$$ Eq. 2.16

$$E_B = \frac{\mu e^4}{2\hbar^2 \varepsilon^2} = \frac{\hbar^2}{2\mu a_B^2}$$ Eq. 2.17

where E_B is the exciton binding energy, E_{b0} is the binding energy of lowest exciton state, and E_{xn} is the exciton transition energy, which correspond to the energy difference between the energy gap, E_g and E_{bn} [91,94].

When the free electrons are residuals in the doped semiconductor, the excitons will interact and eventually bind with the surrounding charges, thus form a charged exciton called trion [95,96]. The trion can be either positive or negative trion, as the electron-hole and electron, or electron-hole and hole, are bounded, respectively, as shown in Figure 2.11. The exciton A and B is cause by the transition from two different valence band to the conduction band. In contrast, the trion A⁻ is the exciton (electron-hole pair) bound with other electron due to the collision or scattering while being excited, then emitted directly after that. There is another form of quasiparticle by many-body interactions of excitons, known as biexcitons, which dominate the photoluminescence (PL) spectra at low temperatures and high excitation densities with 2 pairs of exciton within two different momenta e.g. K and K' as shown in Figure 2.12 [97,98]. The simple overview of an exciton, trion and biexcitons is exhibited in Figure 2.12. All these quasiparticle are available due to their specific reasons in the two-dimensional (2D) atomically thin-layered semiconductor, transition metal dichalcogenides (TMDs), which will be investigated in this thesis.
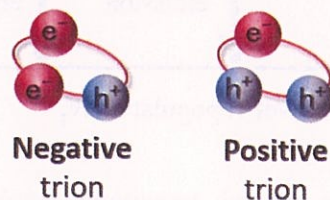
Figure 2.11 Positive and negative trion (charged exciton).
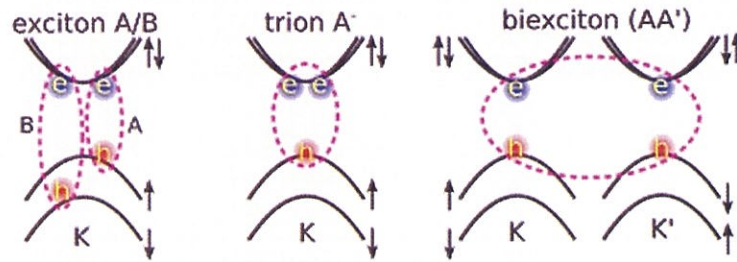
Figure 2.12 Simple overview of exciton, trion and biexciton in 2D semiconductor material of TMDs. (Taken from Ref. [99]).

2.1.6.   Einstein Coefficients and the Radiative Lifetime

The radiative lifetime is one of the important physical property in low-dimensional excitons which represents their optical transition rates, and also helps to understand the nature of the excitation, especially the photon emission; e.g. PL [100,101]. The excited atoms will emit light (photon) by spontaneous emission process, when the electrons in the excited state relax to the ground state. The radiative transition should be followed the Pauli exclusion principle, which the two excited atoms cannot be permitted in the same quantum state [91]. All the mentioned transitions can be demonstrated as 3 probability coefficients called the Einstein coefficients, which can be simplified by Figure 2.13 and Table 2.2.
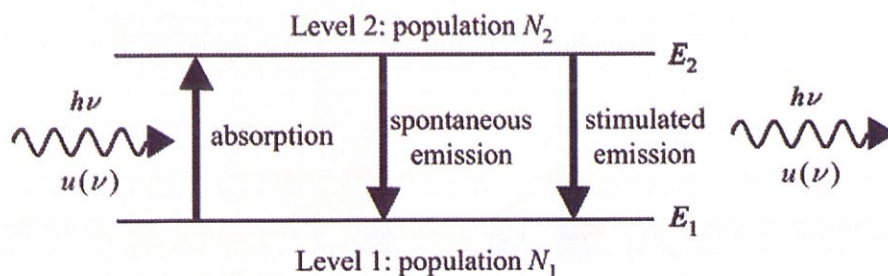
Figure 2.13 Schematic of the optical transitions explained by Einstein coefficients. (Reproduced from Ref. [91]).

Figure 2.13 shows three optical transitions processes of an elementary excitations, where hv denotes the photon energy, $u(v)$ is source of electro-magnetic wave with frequency (v), E_1 and E_2 are initial and final energy state, and N is the population of the atoms [91]. As previously mentioned in chapter 2.1.4, the absorption and emission occur when the electron is excited and decay, respectively, from one to another energy level by absorbing and emitting the photon, for the former and latter, respectively. The energy relationship can be express in equation below [91]:

$$hv = E_2 - E_1 \qquad \text{Eq. 2.18}$$

Table 2.2 Summary of Einstein coefficients and the processes involved [91].

Einstein Coefficient	Process Involved	Corresponding Population Rate Equations, N
A_{21}	Spontaneous emission	$\dfrac{dN_2}{dt} = -A_{21}N_2$ (1)
B_{12}	Absorption	$\dfrac{dN_1}{dt} = -B_{12}N_1 n(v)$ (2)
B_{21}	Stimulated emission	$\dfrac{dN_2}{dt} = -B_{21}N_2 n(v)$ (3)

Table 2.2 denotes the summary for the Einstein coefficients and the process involved, in which the subscript of 21 (12) means the transition from energy level 2 to 1 (vice versa). The appearance of $n(v)$ in Equation (2)((3)) denotes that, the absorption (emission) must be induced and stimulated by the incoming electromagnetic wave radiation [91]. The equation (1) in Table 2.2 can be rewrite as,

$$N_2(t) = N_2(0)\exp(-A_{21}t) \qquad \text{Eq. 2.19}$$
$$= N_2(0)\exp(-t/\tau)$$

where

$$\tau = \frac{1}{A_{21}}. \qquad \text{Eq. 2.20}$$

τ in Eq. 2.20 is called the radiative lifetime, and the relation of Eq. 2.19 and Eq. 2.20 can be described in Figure 2.14.
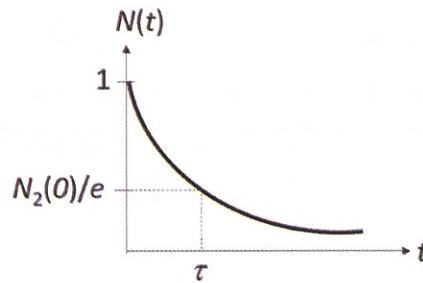
Figure 2.14 The exponential population decay curve.

I assume that the atoms are inside a close black box at temperature T. The atoms will directly interact to the blackbody radiation and the three optical transitions processes will occur. The relation of these processes will be governed by laws the Boltzmann's law in thermal-statistics physics as described in the equations below [91]:

$$B_{12}N_1u(v) = A_{21}N_2 + B_{21}N_2u(v)$$
Eq. 2.21

$$\frac{N_2}{N_1} = \frac{g_2}{g_1}\exp\left(-\frac{hv}{k_BT}\right)$$
Eq. 2.22

where g_1 and g_2 is degeneracies of levels 1 and 2, respectively. The energy spectrum of a blackbody source is given by the Planck formula [91],

$$u(v) = \frac{8\pi hv^3}{c^3}\frac{1}{\exp(hv/k_BT)-1}$$
Eq. 2.23

The equation below tells us that the probability for stimulated absorption and emission are the same apart from the degeneracies factors.

$$g_1B_{12} = g_2B_{21}$$
Eq. 2.24

$$A_{12} = \frac{8\pi hv^3}{c^3}B_{21}$$
Eq. 2.25

The behaviors of atoms in thermal equilibrium condition with blackbody radiation have been understood from the Eq. 2.24 and Eq. 2.25.

2.1.7.   Raman Scattering

Raman scattering spectroscopy is a critical method to determine, identify and analyze a material providing the information on chemical bonding, material structure, and the structural phase transition, which was firstly introduced by Sir C. V. Raman [102,103]. The Raman scattering is mainly due to interaction of incident of light (electromagnetic wave) with atom or molecule in the material, causes the excitation of lattice vibrations (phonons). In principle, a light with a specific energy interacting with the atoms or molecules cause the light scattering at the same energy (elastic scattering) with the incident light, called Rayleigh scattering and also the light scattering to different energy (inelastic scattering) by molecular vibrations, called Stokes (decrease in energy) and Anti-Stokes (increase in energy) scattering. These strong Stokes scattering will be used for spectroscope analysis as Raman scattering spectroscopy [104]. Figure 2.15 shows the examples of the Raman spectrum that contain the previous mentioned process, including Rayleigh scattering, Raman scattering – stokes and anti-stokes.
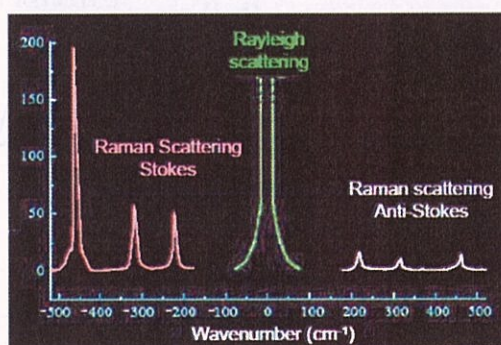
Figure 2.15 Example spectrum of Raman scattering. (Taken from Ref. [105]).

2.1.8.   Optical Anisotropic and Polarization

In general, there are three states of matter; gases, liquids and solids. For gases and liquid, since they have randomly arrangement of the atoms and no long-range order is present, the optical properties of the matters is the same in all directions, so called isotropic. The crystal solids with well-defined axes, can be either isotropic (cubic) or anisotropic (non-cubic), depending on spacing of atoms (lattice constants) in the structure. The anisotropic crystals have different vibrational frequencies in each directions, thus change in the refractive index between

the directions of incident light [91]. Explicitly, the optical properties of anisotropic crystal structure is absolutely depending on the direction of electromagnetic radiation propagation and the polarization state of the radiation [106]. Before I go deep on the optical anisotropy, I will briefly describe about the light as electromagnetic (EM) waves.

Figure 2.16 (a) shows the propagation of light as EM wave, with components of electric field (**E**) and magnetic field (**B**) in-phase and perpendicular with each other, and perpendicular to the propagation direction. As usual, to represent light, I just show the E (Figure 2.16(b-i)) since only the E is detected by eyes, a photographic film, a charge-couple-device (CCD) etc., as a consequence from the Maxwell's equation. The natural or ordinary light is behaving as unpolarized light, as shown in Figure 2.16(b-ii). The wavelength (λ) in Figure 2.16(a) can be defined as the distance between two crest, as shown in Figure 2.16(b-i).
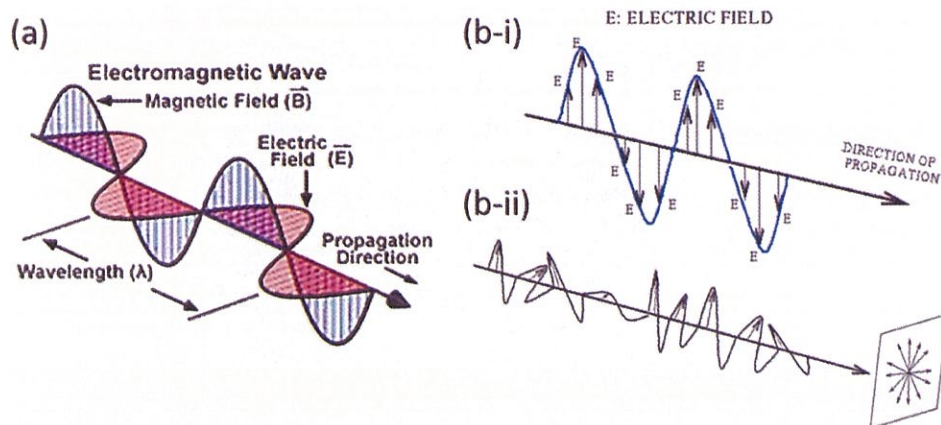
Figure 2.16 Light as EM waves with electric field (**E**) and magnetic field (**B**) components. (Taken from bigbangcentral.com, and hyperphysics.com).

There are three types of light polarization; linear, circular, and elliptical polarization, which are clarified depending on amplitude and phase shift of electric fields, [107] shown in Figure 2.17, and can be explained by: (a) the linear polarization is a plane polarized wave, in which the electric field vector oscillates in specific one plane; (b) the circularly polarization can be classified into either right-circularly polarized (clockwise) or left-circularly polarized (counter-clockwise) states, consisting two perpendicular plane waves with equal amplitude and phase difference of 45° as shown by Figure 2.17(b)-bottom panel; and (c) the elliptical

polarization consists of two perpendicular plane waves with unequal amplitude and phase difference of 90º.
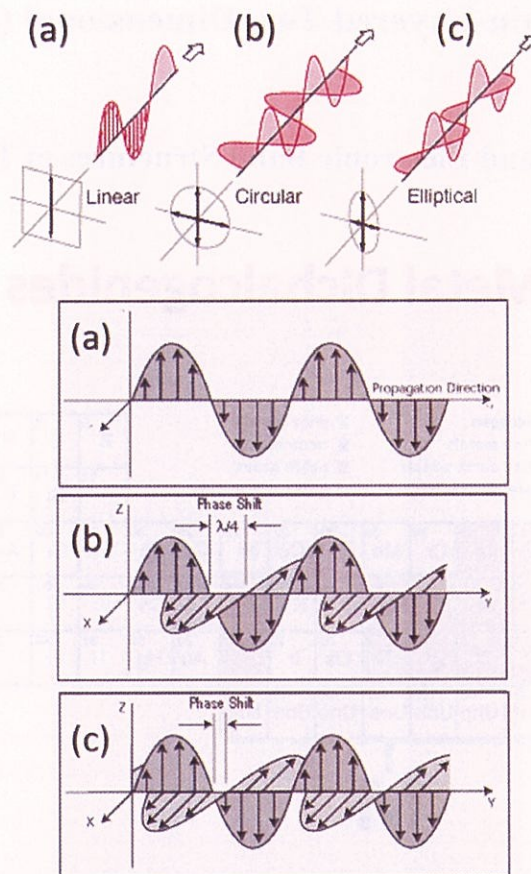
Figure 2.17 Three types of polarization; (a) linear, (b) circular, and (c) elliptical polarization. (Taken from hyperphysics.com (upper) and [108](bottom)).

2.2. Atomically Thin-Layered Two-Dimensional (2D) TMDs

2.2.1.   Crystal and Electronic Band Structures of TMDs
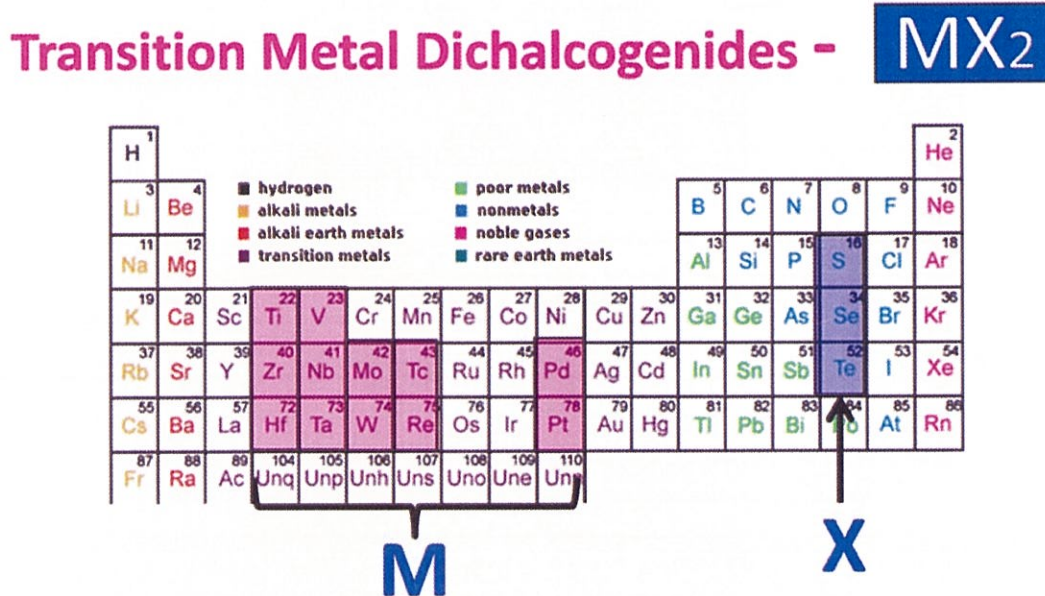
Figure 2.18 Components of TMDs in the overall periodic table. (Taken from Ref. [40]).

2D atomically thin-layered TMDs have attracted great research interest in recent years [33,70,109,110], having a thickness of a just few nanometers with fascinating technological potential [10,15]. TMDs is a material with chemical formula of MX_2 (M = transition metal atom and X = chalcogen atom), where the transition metal element can be either from group IV (4) (Ti, Zr, or Hf), group V (5) (V, Nb, or Ta), group VI (6) (Mo, W), or group X (10) (Pd or Pt), and the chalcogen element (Se, S, or Te), as shown in periodic table in Figure 2.18 [16,111]. In this thesis, I work-out with MoS_2, $MoSe_2$, WS_2, and WSe_2 from group VI and ReS_2 from group VII of TMDs.

Monolayer TMDs consist of three-layer sheets, sandwich of three-dimensionally bonded of X-M-X, which is different from the monolayer graphene with chemically bonded sp^2-carbon atoms in a hexagonal sheet. Figure 2.19 (a) shows the unit cell of most typical MoS_2. Each molybdenum (Mo) atom form the strong covalent bonds to six sulfur (S) atoms in a trigonal prismatic or octahedral structure, results in a 2D layer of three atoms thick (~ 5 – 8 Å)

with no dangling bonds on the basal plane [112]. The adjacent layers as shown in Figure 2.19 (b) are stacked by weakly van der Waals interactions to form bilayer, multilayer until bulk crystal in a variety of polytypes [68,111].
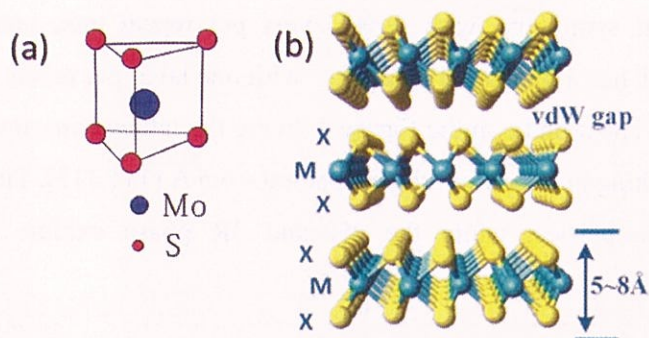
Figure 2.19 (a) Unit cell of MoS_2, and (b) crystal structure of TMDs. (Taken from Ref. (a) [110] and (b) [19]).
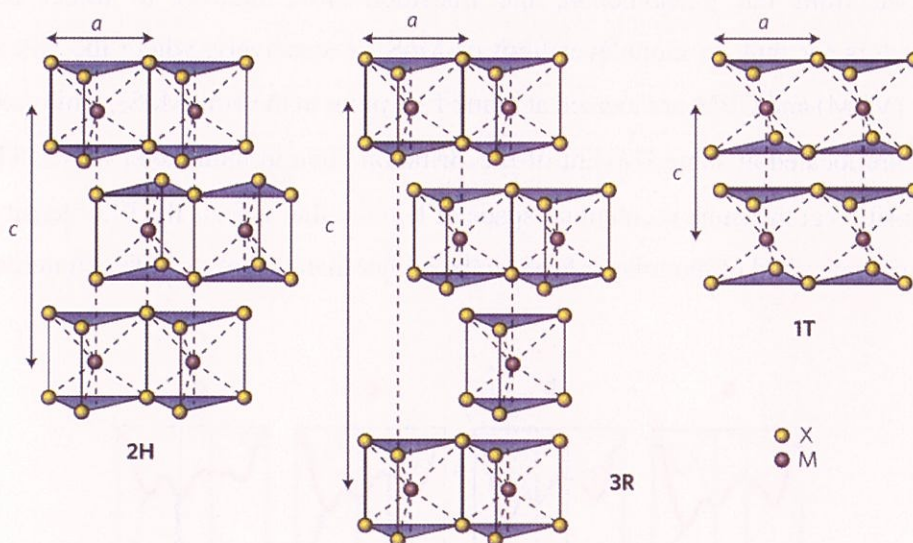
Figure 2.20 TMDs structure of polytypes, 2H (hexagonal symmetry), 3R (rhombohedral symmetry) and 1T (tetragonal symmetry). (Taken from Ref. [111]).

Figure 2.20 shows the polytypes TMDs structure with various metal atom coordination and stacking orders [111], indicated by 2H, 3R an 1T phase. The H, R, and T are denoted by hexagonal, rhombohedral and tetragonal (octahedral) symmetry, respectively, while 1, 2, and 3 are assigned to the number of layers correspond in a unit cell [112]. The 2H structure has a

hexagonal symmetry with two layers per repeat unit, and trigonal prismatic coordination; 3R has a rhombohedral symmetry, with three layers per repeat unit, and trigonal prismatic coordination, and 1T has a tetragonal symmetry with one layer per repeat unit, and octahedral coordination [111]. The a and c in the Figure 2.20 are the lattice constants in the range of 3.1 – 3.7 Å, and the stacking index for interlayer spacing ~ 6.5 Å [111,113]. The 1T phase of TMDs has the metallic properties, while the 2H and 3R phase exhibit the semiconducting properties [68,112].

Figure 2.21 shows the electronic band structure of $2H\text{-}MoS_2$, calculated by density functional theory (DFT) for bulk, quadlayer, bilayer and monolayer, with y- and x-axis corresponds to energy and momentum, respectively. The monotonic increased of indirect band gap (conduction band minimum, CBM) as decreasing the layer numbers can be observed [33]. Consequence from the phenomenon, the transition from indirect to direct band gap semiconductors for bulk to monolayer limit of MoS_2, respectively, where the valence band maximum (VBM) and CBM are located at Γ and Γ-K point in the bulk MoS_2, while both VBM and CBM are located at same K-point of the Brillouin zone in monolayer MoS_2. The direct optical transition at the same momentum space of K point thus affects the PL intensity as well as its PL quantum yield of monolayer MoS_2 to be higher than that of its bulk counterparts [22].
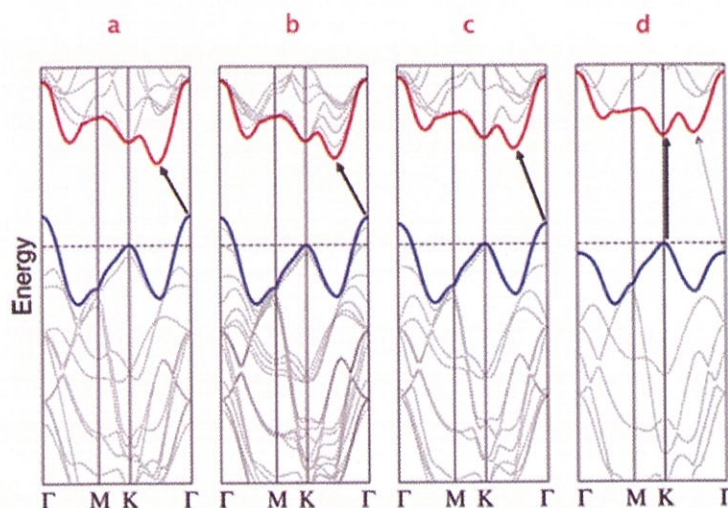
Figure 2.21 Electronic band structure of $2H\text{-}MoS_2$ by DFT calculation, for (a) bulk, (b) quadlayer, (c) bilayer, and (d) monolayer. (Taken from Ref. [33]).

2.2.2.   Photoluminescence (PL) Spectra

PL comes from the recombination process of electron and hole pair. The PL spectra can generally be detected if a material has a band gap, in which the emitted photon energy corresponds to the band gap of the material. The basic concept of the PL has been already discussed in the previous sub-chapter of optical transition (Chapter 2.1.4).

Figure 2.23(a) shows the PL spectra of MoS_2 sample with the y-axis shows the PL intensity as a function of photon energy. The large variation of PL intensity examined for MoS_2 sample in Figure 2.23(a) is due to the indirect band gap nature for 2L MoS_2 instead of direct band gap nature for 1L MoS_2. Figure 2.23(b) exhibits the normalized PL of MoS_2 as varying layer numbers from 1–6L. The three distinct peaks of A, B and I are assigned to the A, B exciton and indirect band gap peak, respectively. The spectral shapes were observed differently as changing the layer number that can be used as the fingerprint to determine the layer numbers of MoS_2. The different of PL spectral shape as changing layer number for WS_2 and WSe_2 are also reported previously [114].
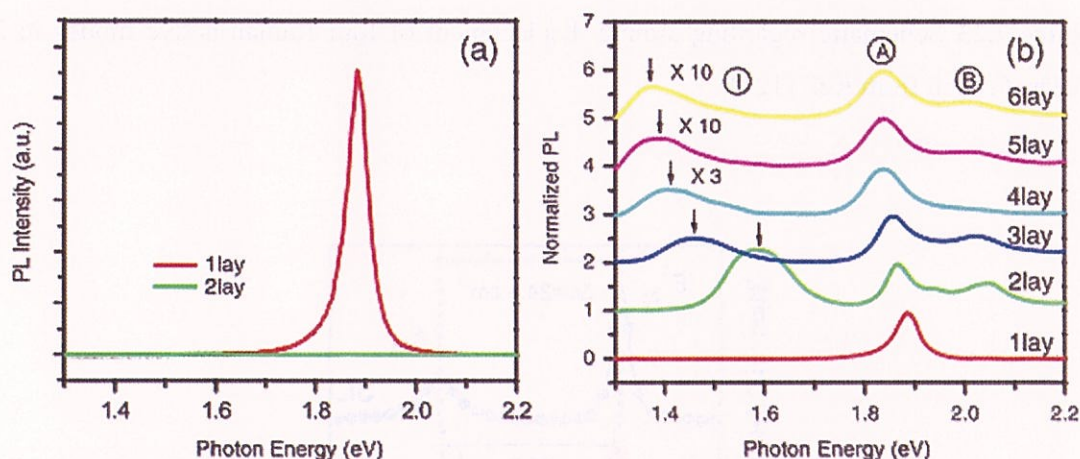
Figure 2.22 PL spectra of MoS_2. (Taken from Ref. [22]).

2.2.3.   Raman Spectra

Raman spectroscopy provides the fingerprint to identify the layer number of atomically thin-layered materials, as well as versatile method to explore the phonon modes in TMDs crystals [37,115–118]. The concept of Raman scattering has been explained in Chapter 2.1.7.

There are four optically active Raman modes, namely as A_1g, E_1g, E_2g and B_2g modes as shown in Figure 2.23, where A_1g and E_1g correspond to optical vibrations of chalcogen and metal atoms within the same layer, while the two latter modes are originated from antiphase vibration between different layers [116]. The A_1g and E_1g are frequently used in the study of Raman scattering spectra of TMDs [119,120], as they correspond to out-of-plane and in-plane vibrational mode, respectively.
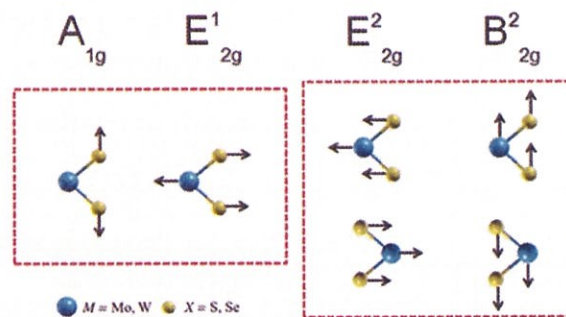
Figure 2.23 Schematic regarding atomic displacement of four Raman active modes in 2D TMDs. (Taken from Ref. [121]).
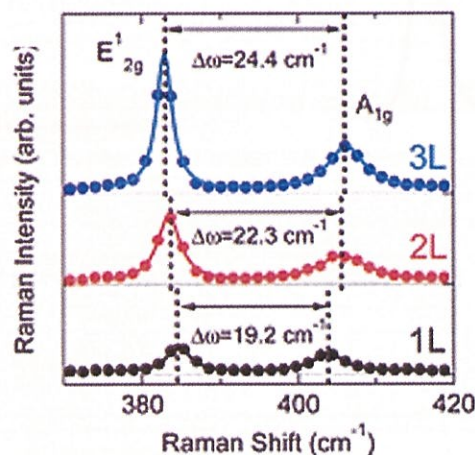
Figure 2.24 Raman spectra of MoS_2. (Left) the Raman spectra of 1L – 6L MoS_2; (right) the expanded scale of Raman spectra for 1L – 3L MoS_2. (Taken from. Ref. [38]).

Figure 2.24 shows Raman spectra for 1–3L of MoS_2. The increase in frequency difference between E^1_{2g} and A_{1g} as the increase in layer number is the crucial fingerprint to

determine the layer number of MoS_2. The Raman scattering spectra and fingerprint for the other TMD such as WSe_2 can be seen in Figure 2.25, where the Raman spectra for 1L WSe_2 is absent of 308 cm^{-1} peak, but the peak becomes Raman active for 2L and more thicker layer, which is useful to confirm the layer number of WSe_2 [122].
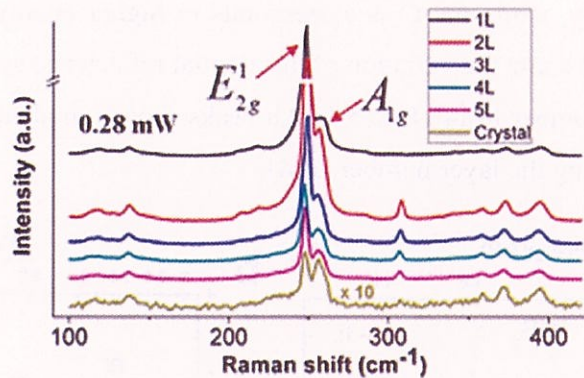
Figure 2.25 Raman spectra of WSe_2. (Taken from Ref. [123]).

2.2.4.   Differential Reflectance ($\Delta R/R$) Spectra

The differential reflectance ($\Delta R/R$) spectrum is referring to reflectance contrast of the very thin material supported by the transparent substrate, and contains the information on the light absorbance on the approximation of normal incidence of light and very thin material [68,114]. The relationship of differential reflectance (reflectance) and absorbance can be simplified as [68]:

$$\Delta R / R = \frac{R_{s+q} - R_s}{R_q} = \frac{4}{n_g^2 - 1} \text{Abs} \qquad \text{Eq. 2.26}$$

where the R_{s+q} and R_s are reflectance of substrate with and without TMDs sample, respectively, while n is refractive index of the substrate, and Abs. is absorbance of the TMDs itself. Absorbance, sometimes called optical density (O.D) [91] has a direct relation to the transmission of sample as indicate in Eq. 2.27 [91,124].

$$\text{O.D} = \log_{10} \frac{1}{T} \rightarrow T = 10^{-\text{O.D}} \qquad \text{Eq. 2.27}$$

The differential reflectance spectra of monolayer TMDs (WS₂, and WSe₂) are shown in Figure 2.26. The three prominent peaks of A, B and C is assigned to the A and B exciton transition, respectively, while the C is corresponds to higher energy absorption C exciton. Figure 2.26(a) and (b) show the variation of differential reflectance spectra of WS₂ and WSe₂ with different layer number from 1L to 5 L. All peaks show a gradual increasing and distinct red-shift with increasing the layer number [114].
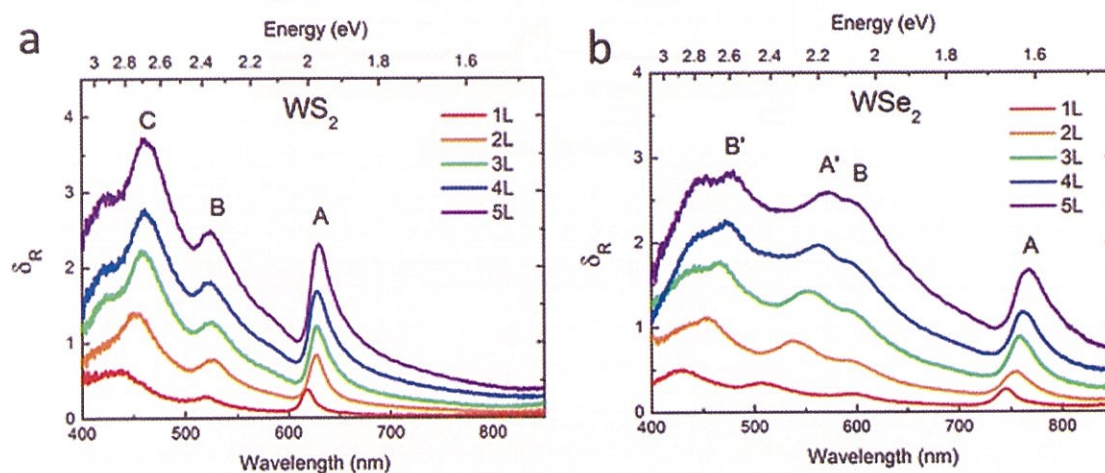
Figure 2.26 Differential reflectance spectra of (a) WS₂ and (b) WSe₂ for 1L - 5L. (Taken from Ref. [114]).

2.2.5.   TMDs Chemical-Treatments

Almost monolayer TMDs in this chapter were prepared using mechanically exfoliation method. Only for monolayer MoS₂ and ReS₂ were chemically treated after the mechanical exfoliation to increase their PL intensities (as well as the PL quantum yield). The detail TMDs-chemical treatment involved in this thesis are discussed as followed:

F₄TCNQ: 2,3,5,6-tetrafluoro-7,7,8,8-tetracyanoquinodimethane

The 2,3,5,6-tetrafluoro-7,7,8,8-tetracyanoquinodimethane (F₄TCNQ) is used for the chemical treatment for ReS₂ in this study. The *p*-type chemical dopant of F₄TCNQ has previously reported to successfully improved and tuning the PL intensity in *n*-type monolayer

MoS$_2$ (Figure 2.27) [38]. As a consequences of F$_4$TCNQ treatment, the PL intensity of an unintentionally heavy electron-doped (*n*-type) monolayer MoS$_2$ becomes improved [125] by the enhancement of neutral exciton emission (*X*) instead of charged exciton, trion X^- [38].
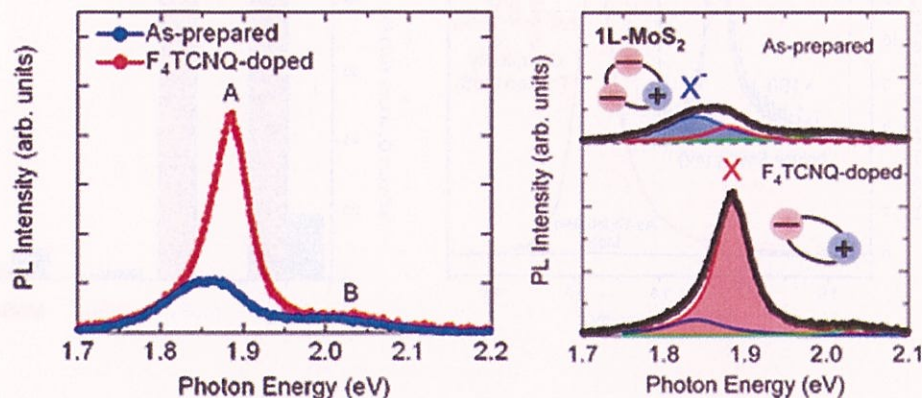
Figure 2.27 PL spectra of monolayer MoS$_2$ before (as-prepared) and after F$_4$TCNQ treatment (F$_4$TCNQ-doped). (Taken from Ref. [38]).

TFSI: Superacid bis(trifluoro-methane)sulfonamide

Only the monolayer MoS$_2$ is chemically treated by a nonoxidizing organic superacid, bis(trifluoro-methane) sulfonimide (TFSI) in this thesis, because the chemical treatment causes an extremely PL intensity enhancement of monolayer molybdenum disulfide, MoS$_2$ and tungsten disulfide, WS$_2$ but the superacid TFSI does not work for the selenide (Se) group of monolayer TMDs e.g.: MoSe$_2$ and WSe$_2$ [75,126]. The enhancement of PL intensity reaches to about 100 times, which can be seen clearly in their optical PL mapping of as-prepared and treated sample. According to the result of this paper [75], the near-unity PL quantum yield of the monolayer TMDs are demonstrated as shown in Figure 2.28.
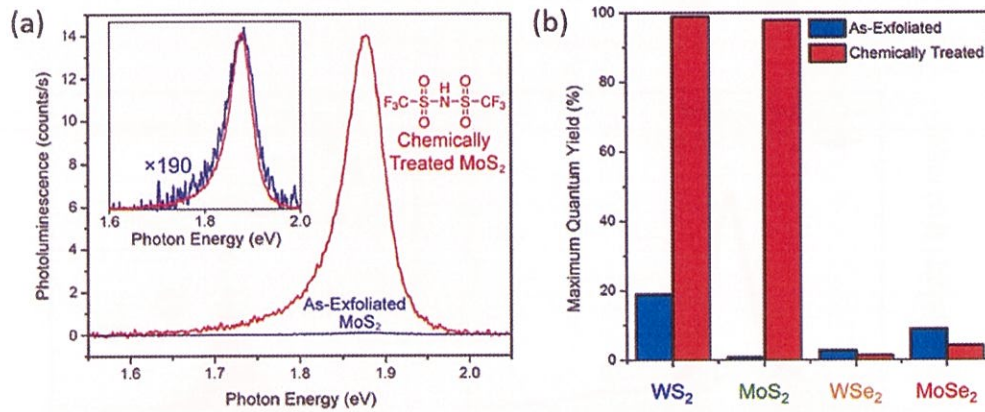
Figure 2.28 Enhancement of PL intensity and PL quantum yield of TMDs. (a) The PL spectra for as-exfoliated and TFSI-treated monolayer MoS2, and (b) the PL quantum yield of TMDs before and after TFSI treatment. (Taken from Ref. [75] and [126], respectively).

2.2.6.   Special Features of TMDs

Remarkably distinctive features of 2D semiconducting TMDs are their strong Coulomb interactions due to reduced dielectric screening in these atomically-thin systems, thus the optical properties of these materials dominated by excitonic transition, electron-hole pair (exciton) and charged exciton (trion) [127–129]. Moreover, the large exciton binding energies of few hundreds meV [70,71,130], are almost one order of magnitude larger than those of other bulk semiconductors [125,131]. This makes the exciton be stable even in room temperature and implies the platform to study many-body effects in their exciton states [63,132–135].

The valence band edge of the TMDs is split, $\Delta_{SO} \sim 100 - 500$ meV [136,137], hence the optical transition between the split valence bands and the conduction band gives rise to the two prominent peaks of absorption spectrum denotes by A and B exciton [70], as shown in Figure 2.29. Overall schematic diagram of energy band for the monolayer, bilayer and bulk TMDs can be expressed in Figure 2.30. There are two-band of valence band split due to spin-orbit coupling, where the splitting were seen to be increase as increase in layer number. Moreover, the figure also show the exciton binding energy, E_B and the band gap energy, E_g (BG peak) which has a relation to the A and B exciton energy transition, by $E_{xA} = E_g - E_B$ (same as eq. 2.16).
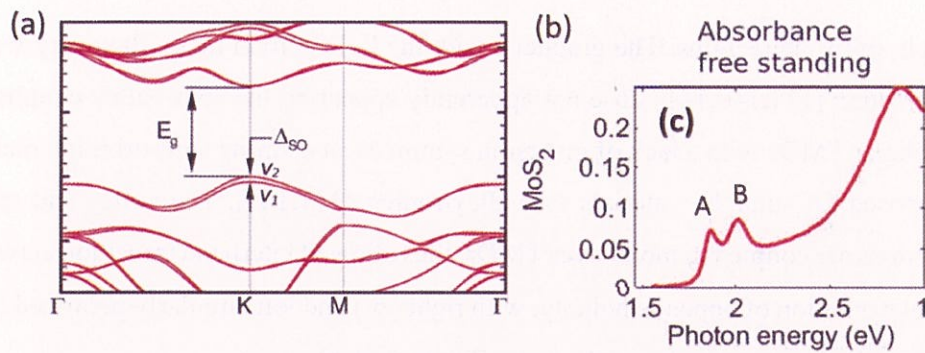
Figure 2.29 Band structure and absorption spectra of MoS$_2$. (a) Typical band structure for MX$_2$ with spin-orbit (SO) splitting of the valence band, v_1 and v_2, and (b) optical absorption spectrum of MoS$_2$. The A and B exciton are denoted in the spectrum. (Taken from Ref. (a) [70] and (b) [138]).
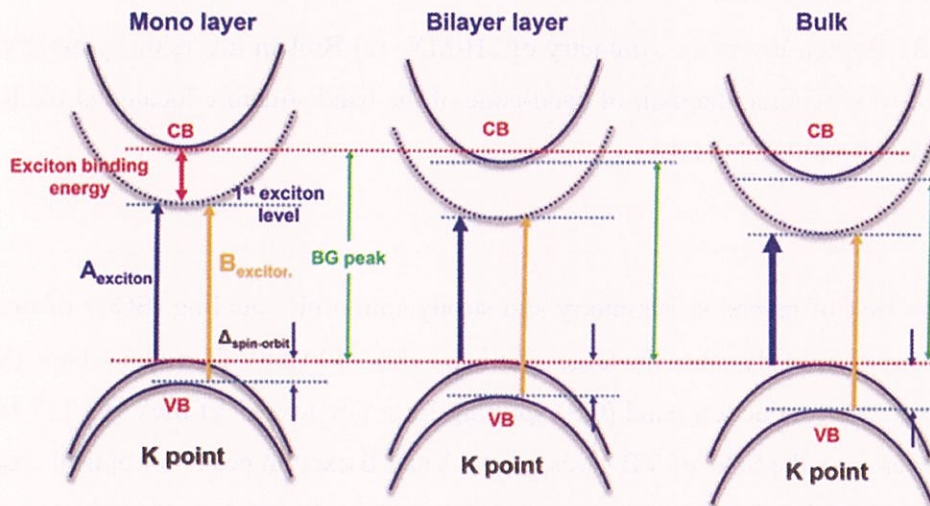
Figure 2.30 Schematic of energy diagram of monolayer, bilayer and bulk TMDs with exciton binding energy and spin-orbit splitting of the valence band. (Taken from Ref. [139]).

The broken inversion symmetry and large spin-orbit interaction in monolayer TMDs cause the anomalous coupling of spin and valley degree of freedom. Figure 2.31(a) shows that the two unit cells of monolayer MoS$_2$, which exhibits broken inversion center symmetry in the middle plane. Moreover, the high total mass elements of MX$_2$, consequently give rise to the

strong spin orbit interactions. The graphene with the light carbon mass, thus very weak spin-orbit interaction [111,140,141] dose not apparently appearing the spin-valley coupling. Thus, the monolayer TMDs with a lack of inversion symmetry and strong spin-orbit interaction have been proposed for suitable materials for valleytronics [111,141]. The valley and spin of the valence bands are coupled in monolayer TMDs, thus allowed interband transition at two valleys for optical excitation of opposite helicity, with right (σ_+) and left circularly polarized (σ_-) at the K and –K valleys, respectively, as shown in Figure 2.31(b).
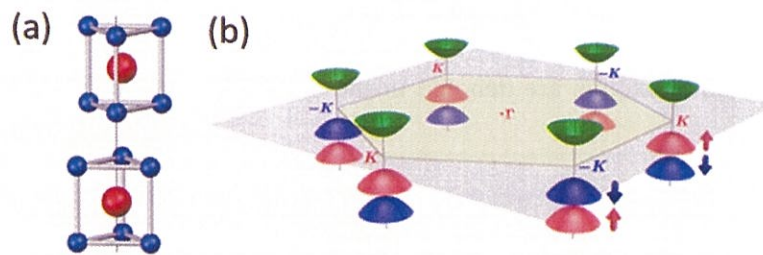
Figure 2.31 Broken inversion symmetry of 2H-MX$_2$ (a) Broken inversion symmetry of 2H-MoS$_2$, and (b) schematic diagram of band-edge of the band structure located at the K and K' points.(Taken from Ref. [141]).

The lack of inversion symmetry and strong spin-orbit coupling (SOC) of monolayer TMDs materials not only cause the large splitting $\sim 100 - 500$ meV for valence band (VB), but also affect to the conduction band (CB) splitting for a few to tens of meV [69,137,142]. For simplest overview, the SOC of VB gives rise to A and B exciton peaks for optical absorption, while SOC of CB is related to the optically bright (allowed) and dark (forbidden) transition. The SOC of both VB and CB can be seen in Figure 2.32, where the up- and down- arrow denote the electron-spin.
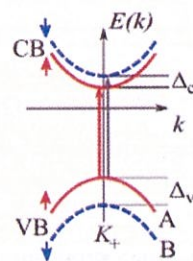
Figure 2.32 Schematic of band structure of TMDs with spin-orbit coupling (SOC) induced splitting valence and conduction band. (Taken from Ref. [137]).

The dipole-allowed exciton called as optically bright exciton is generated in the usual optical excitation process, and recombination of dipole-allowed exciton emits the photons as luminescence, where the spin-flip processes are not occurred. In contrast, the subsequent process such as scattering and collision of exciton with electrons, phonons, and defects, may induce the spin flips, accompanied by changing its momentum [69], would generate the spin-related dark excitons, and the dark exciton does not directly couple to light. Figure 2.33(a) shows the splitting of dark-bright energy of A $1s$ state excitons in MoX_2 and WX_2 systems by theoretical calculation. The MoX_2 exhibits that the bright exciton state is lower energy state than that to dark exciton state, but opposite to WX_2 as the dark exciton state is lying below the bright state. The different features of upper- and lower-lying dark state causes the different temperature dependence of photoluminescence intensity with elevating the temperature, as shown in Figure 2.33(b).
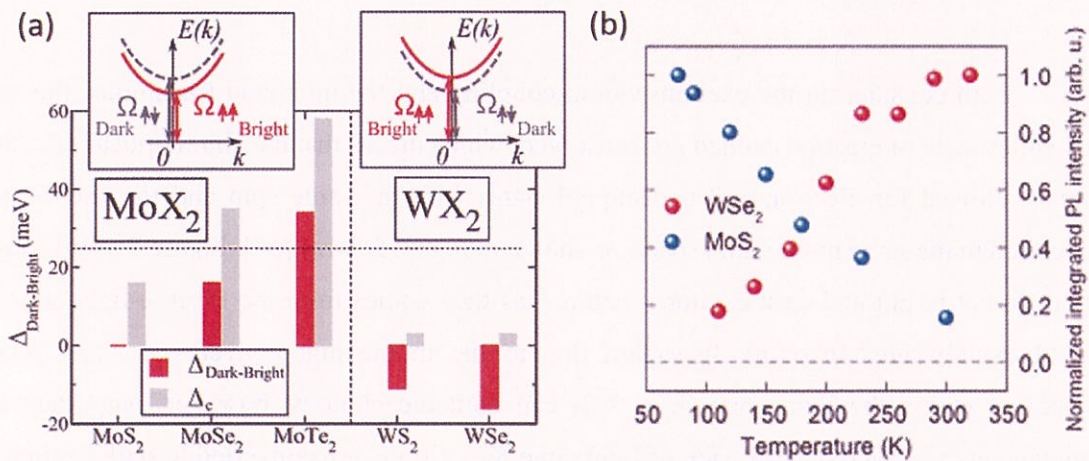
Figure 2.33 Dark states of TMDs. (a) Splitting of energy band for upper- and lower-lying dark exciton state for MoX_2 and WX_2, respectively, and (b) Temperature dependent PL intensity from monolayer MoX_2 and WX_2 with upper- and lower-lying dark state. (Taken from Ref. (a) [137] and (b) [143]).
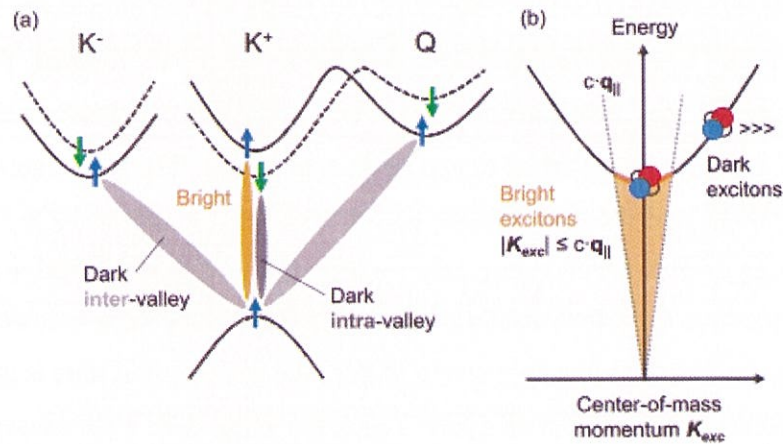
Figure 2.34 Several types of bright and dark exciton transition. (a) Schematic overview of typical bright (allowed) and dark (forbidden) exciton transition, (b) schematic illustration of the exciton-photon dispersion (light-cone) for exciton picture. (Taken from Ref. [69]).

With considering the exciton-photon coupling and the interband transitions, the spin and valley state of electron excited are conserved, which means that the chiral optical selection rule is allowed for electron and unoccupied states with the same spin and the exciton are generated in the same momentum space, as shown in Figure 2.34(a) [69]. Figure 2.34(b) shows the different bright and dark excitons features, as they comes from the exciton-light cone or called exciton-light (photon) dispersion due to the momentum conversion. The exciton generated within the light cone ($K_{exc} = 0$) can emit the photons, however, once they are spontaneously scattered at out-side of light cone $K_{exc} > 0$ i.e. are converted to dark exciton in the momentum space. They are optically inactive, not spontaneously decayed [69] without interaction with the dark exciton and the other quasiparticles, such as phonons.

The atomically thin 2D TMDs also show the strong optical response due to the band nesting [31,144,145]. As an overview picture, the band nesting is occurred, when the dispersion of valence and the conduction band are parallel to each other in the energy band structure. The enhancement of light absorption for the resonance energy, not only due to the direct band gap semiconductor for its monolayer limit, is occurred, which is appeared in van Hove singularities of joint density of states (JDOS). The singularity features in the JDOS correspond to the divergence in optical conductivity and only occur in the low-dimensional material [92,144]. Figure 2.35 shows the interband absorption and photoluminescence (PL) process, where both electrons excited to the conduction band, and the holes left at the valence band will

spontaneously relax to their band extremum. The immediate separation of electron and hole at Λ and Γ point, respectively, also causes the low quantum yield of the TMDs material for higher excitation photon energies than energy resonant [31].
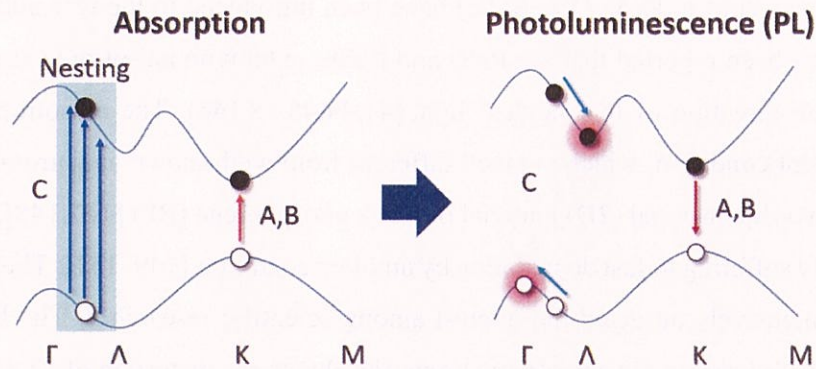
Figure 2.35 Optical response of TMDs materials due to the band nesting. (Reproduced from Ref. [92]).

2.2.7. Optical Properties of Anisotropic structure of TMDs family, Rhenium Dichalcogenides, ReX₂ (X = S, Se)
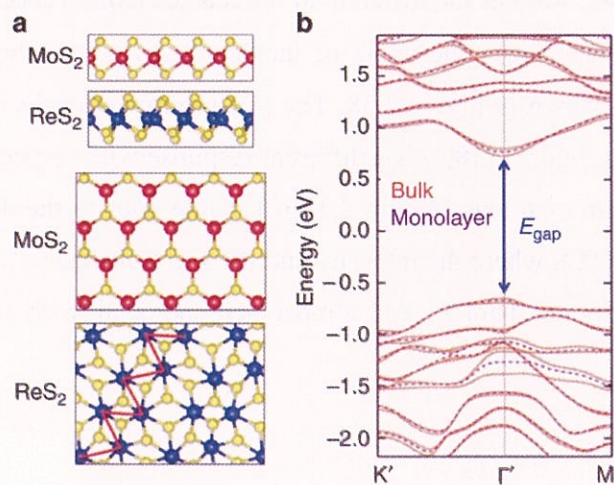
Figure 2.36 Crystal and electronic structure of ReS₂. (a) Comparison of side (upper) and top (bottom) view of 2H (2-hexagonal phase) of MoS₂ and distorted 1T (1-tetragonal) of ReS₂ crystal structure – the red line indicate Re-chain. (b) DFT calculation of electronic structure for bulk (orange line) and monolayer (purple dashed-line) ReS₂. (Taken from Ref. [41]).

Recently, new members from the family of transition metal dichalcogenides (TMDs), rhenium dichalcogenides, ReX_2 (X = S, Se) have been introduced to the research field of 2D materials. It has been reported that the ReS$_2$ and ReSe$_2$ exhibit an anisotropic structural from the propagation direction of the incident light [41,44,45,58,146]. The anisotropic ReX_2 are stable in ambient condition, which is much different from well-known anisotropic atomically thin-layered two-dimensional (2D) material of black phosphorene (BP) [147,148], because the BP is obviously suffering to fast degradation by ambient condition [149–151]. These properties of ReX_2 has intensively attracted the interest among scientific researches. The lower crystal symmetry of ReS$_2$ leads to the anisotropic properties due to the distortion of 1T (1-tetragonal) structure (Figure 2.36(a)), which is different from other family members of TMDs such as MoS$_2$ [42,51,152,153]. Moreover, the atomically thin ReS$_2$ has been reported as the direct band gap semiconductors from the bulk counterparts and monolayer limit (Figure 2.36(b)) by the first report of density-functional theory (DFT) calculation [41], which is further distinguished as the atomically thin MoS$_2$.

Figure 2.37 shows results of high-magnification of annular dark-field (ADF) by transmission electron microscopy (TEM). The ADF image clearly exhibits the Re-chain (b-axis) of ReS$_2$ and ReSe$_2$. Raman and differential reflectance ($\Delta R/R$) spectra have also reported the highly-sensitive response to the angle of incident light polarization due to anisotropic structural of ReS$_2$, as shown in Figure 2.38. The two prominent peaks of Raman modes of 4 layer (4L) observed in Figure 2.38(a) has different response with respect to the cleaved edge, also known as Re-chain or b-axis (Figure 2.38(b)). Same goes to the differential reflectance spectra of monolayer (1L), where the intensity and the spectral shape of exciton 1 (Exc-1) and exciton 2 (Exc-2) response parallel and almost perpendicular with regards to the b-axis, respectively.
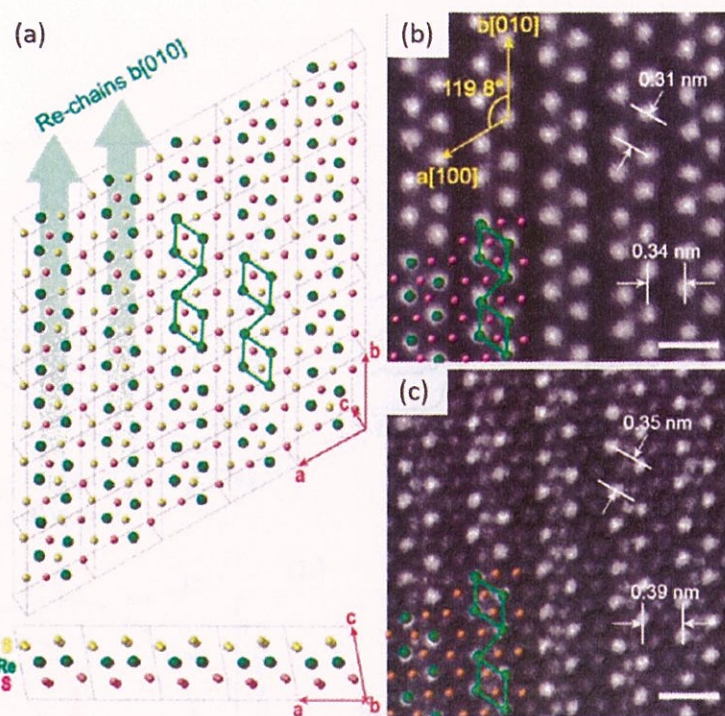
Figure 2.37 (a) Schematic of crystal structure of ReX_2. (b) and (c) ADF images results of ReX_2. The lattice spacing for Re diamond chains (Re diamond-shape clusters) is 0.34 nm (0.31 nm) and 0.39 nm (0.35 nm), for ReS_2 and $ReSe_2$, respectively. Scale bar is 0.6 nm. (Taken from Ref. [154]).
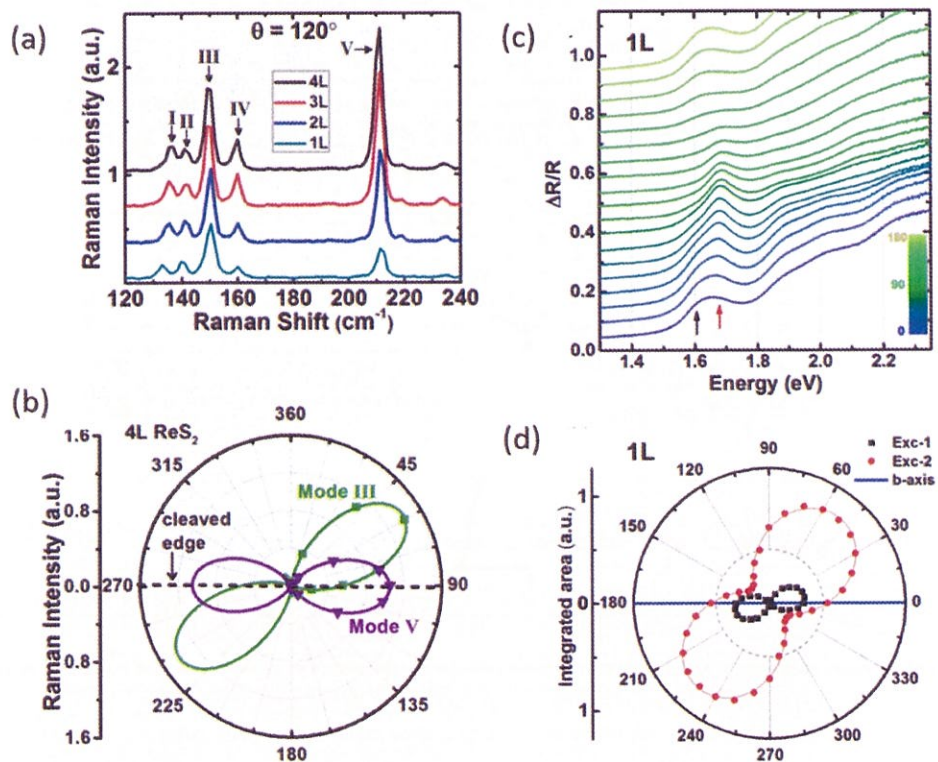
Figure 2.38 Anisotropic response of (a,b) Raman and (c,d) differential reflectance spectra of ReS$_2$. (Taken from Ref. (a,b) [44] and (c,d) [45]).

Chapter 3.   Evaluation   of   PL   Quantum   Yield   of WSe₂ using 3-Borylbithiophene Derivative

3.1. Introduction

Photoluminescence (PL) quantum yield is defined as the ratio of absorbed photons in the materials and emitted photons from the materials [76,77], which is essential value for optical analysis of semiconductors [77,155]. There are two typical ways of evaluating the PL quantum yield, such as absolute method using the integrated sphere [156–158] and relative method using the reference dye with well-known quantum yield [77,157].

Monolayer TMDs, MX_2 (M = Mo, W; X = S, Se) are reported to be the direct band gap semiconductor at K-point of the Brillouin zone [22,33,159], thus promising for optoelectronic devices [15,72,160]. The light emission efficiency is critical value to evaluate the quality of monolayer TMDs and also determine the device performance, because the light emission process is strongly affected by the non-radiative relaxation process of electron-hole pairs (excitons). As-exfoliated TMDs have been reported to have very low PL quantum yield due to high defects densities and large nonradiative recombination rates [22,33,73].

In this Chapter, I have carefully measured and studied the evaluation method of photoluminescence (PL) quantum yield of monolayer semiconductors transition metal dichalcogenides (TMDs), tungsten diselenides, WSe₂ on a transparent substrate using both absolute and relative methods [76,157]. Monolayer WSe₂ was chosen from TMDs because it exhibits various important characteristics, for instances single photon light emission [34,161–164], biexciton emission [97], and existence of dark exciton state [143,165], which represents a model of 2D systems to understand the light emission properties. I have employed highly-emissive 3-borylbithiophene derivative ($C_{58}H_{49}BN_2S_4$) [166] in a PMMA matrix as our reference dye, in which the PL intensities and absorption of both reference dye and monolayer WSe₂ were compared.

3.2. Methodology – Samples Preparation

3.2.1.   Preparation of Monolayer TMDs samples
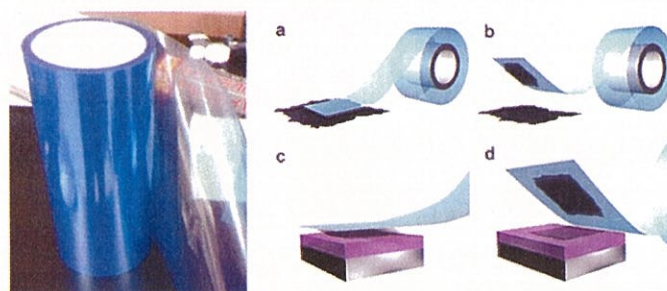
Figure 3.1 Mechanical exfoliation method. (Left) Photograph of blue tape using for mechanical exfoliation, (Right) Brief overview of mechanically exfoliation method [8].

The 2D TMDs have strong covalent bond between intralayer transition metal M atom and chalcogen X atom, but weak van der Waals interactions between its adjacent layers [17,167]. Indeed, the TMDs can be simply exfoliated using mechanical exfoliation [4], chemical exfoliation [168], and so on. In this thesis, the preparation of TMDs samples are using mechanically exfoliation method so-called "scotch-tape" exfoliation method [2,4]. The "scotch-tape" used in this study is a special adhesive blue tape for exfoliation as shown in Figure 3.1 (left). The schematic and brief overview of mechanical exfoliation process are shown in Figure 3.1 (right). For Figure 3.1 (right) (a – d) show the blue tape is pressed against a bulk TMDs crystal, and the crystals will mechanically cleaved. Then, the micro-crystals on the tape will be transferred to the SiO_2/Si substrate (300-nm- thick SiO_2 layer) or quartz substrate, once peeling-off process is applied. The layer number and thickness of the layered TMDs will be determined by optical spectroscopy measurement such as Raman scattering, PL or atomic force microscopy (AFM).

3.2.2.   Preparation of Reference Dyes

Reference dyes play crucial parts as method of evaluation and determining the photoluminescence (PL) quantum yield (QY) of monolayer TMDs in this study. I have

prepared two types of reference dyes, which are Rhodamine 6G (R6G) and 3-borylbithiophene derivative dye, and these dyes were prepared carefully according to previous suggested reports [166,169]. The dye with high QY in the solid form (thin-film) should be chosen to proceed the PL QY measurement of TMDs. Therefore, I have choose the 3-borylbithiohene derivative as my reference dye. But in this thesis, I will explain both procedure to prepare the references dye as supplementary information. The detail preparation procedures are explained as follows.

Rhodamine 6G (R6G)

As an initial stage to evaluate the PL QY of the monolayer TMDs, I have employed a standard reference luminescent dye, Rhodamine 6G (R6G) as our reference dye. The R6G is a typical laser dye with molecular formula of $C_{28}H_{31}ClN_2O_3$, and has high QY value only in solution form for > 80 % [170]. The dye has been prepared accordingly before we confirm the low value of QY in solid form (thin-film) and proceed to other reference dye:

The solid powder of R6G was added to a 1 wt % solution of solid poly(vinyl alcohol) (PVA) (Mw = 1.25×10^5 g/mol) in the ratio of 1:1 in methanol – water with the concentration ~ 10^{-5} M. The solution was sonicated using the bath-sonicator about 10 – 15 minutes until the solid PVA is fully dissolved. The R6G dye solution was then spincoated to a quartz substrate using spincoater (spincoater 1H-D7, Mikasa Co. Ltd.), using the spun rate of 500 rpm for 5 - 10 seconds and 5000 rpm for 30 seconds immediately, to get the uniform film to measure the absolute quantum yield.

3-Borylbithiophene Derivative

The reference dye of 3-boryl-2,2'-bithiophene with 7 types of full-color organic solids were suggested to be highly emissive and have high quantum yield with wide range of emission wavelength from 350 to 900 nm [166] as shown in Figure 3.2 (upper panel). Figure 3.2 (lower panel) shows the 7 different color of the dyes with their respective emission wavelength as Figure 3.2 (upper panel). The derivative no. 7, $C_{58}H_{49}BN_2S_4$=5,5'''-Bis(N,N-dipenylamino)-4'-dimesitylboryl-2,2':5',2'':5'',2'''-quaterthiophene with similar emission wavelength (500

– 900 nm) to that of monolayer TMDs was chosen for measuring the relative quantum yield. This 3-borylbithiophene derivative dye was chosen instead of R6G because this dye has high QY value of > 30 % in solution and solid form. The dye has special bulky-boryl group in their conjugate-π to prevent the intermolecular interaction that diminished the self-quenching emission in condensed phase [166]. The method to prepare the dye has been explained as below:
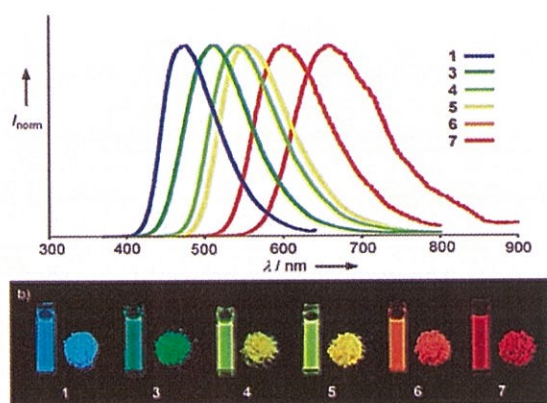
Figure 3.2 Fluorescence of 3-borylbithiophene derivatives. (a) Fluorescence spectra of derivatives 1 and 3-7, measured in THF solution, and (b) photographs of the dyes under irradiation at 365 nm. (Taken from Ref. [166]).

The dye solution with concentration of 10^{-3} M prepared in concentrated of tetrahydrofuran (THF), was mixed with ratio of 1:1 to 2×10^{-4} M of poly(methyl methacrylate) (PMMA) (with respect to THF solution), as PMMA behave as a protecting layer [171]. The solution was bubbling under Argon gas for 10 minutes. The mixed dye solution was then spincoated to ~0.15 mm and ~1.00 mm thickness of micro-cover glass and quartz substrate, respectively. The substrate is spun at a low speed 500 rpm for 5 - 10 seconds and directly proceed to higher speed of 5000 rpm for 30 second to spread homogeneously the dye solution to the substrate to form a uniform and large size (10 mm × 10 mm) of reference dye film.

3.3. Sample Characterizations

3.3.1.   PL, Raman and Differential Reflectance Measurements

The photoluminescence (PL), Raman and differential reflectance measurement on TMDs materials were carried out using micro-Raman spectroscopy system, (Nanophoton, RAMANTouch). The photograph of system and the objective microscope lens used are shown in Figure 3.3.
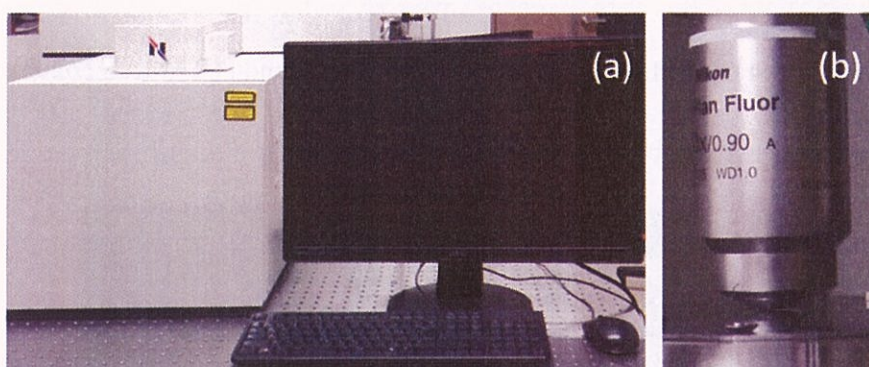
Figure 3.3 Micro-Raman spectroscopy system. (a) Photograph of Nanophoton RAMANTouch, and (b) the microscope objective lens.

Figure 3.4 shows the schematic diagram of Nanophoton (RAMANTouch) setup composed of several parts: (1) the excitation wavelength of laser light (continuous wave, c.w.) of 532 nm is employed, (2) the microscope objective lens of either ×5 (numerical aperture, NA = 0.2), ×20 (NA = 0.5), ×50 (NA = 0.8) and ×100 (NA = 0.9) are being used, (3) the Raman (PL) signals from the samples were detected by spectrometer with Si CCD camera, and (4) the data were recorded by the software of Raman Viewer. For the measurements of anisotropic structural materials such as rhenium disulfides (ReS$_2$) and black phosphorus (BP), the linear polarizer (LP), half-wave plate (HW) and quarter-wave plate (QW) will be used to significantly observe the different of optical measurement correspond to the incident excitation angle. The green and red solid line is the excitation and emission side, respectively.
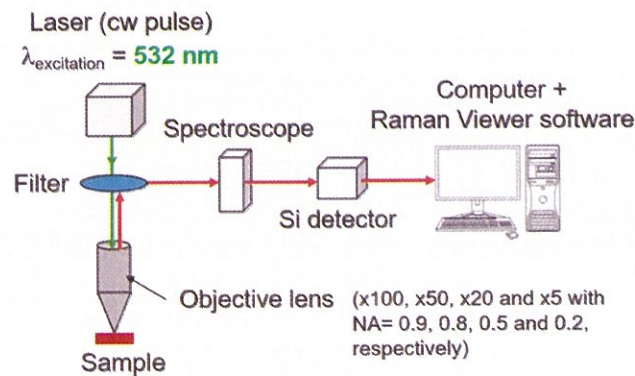
Figure 3.4 Optical schematic diagram of Nanophoton (RAMANTouch).
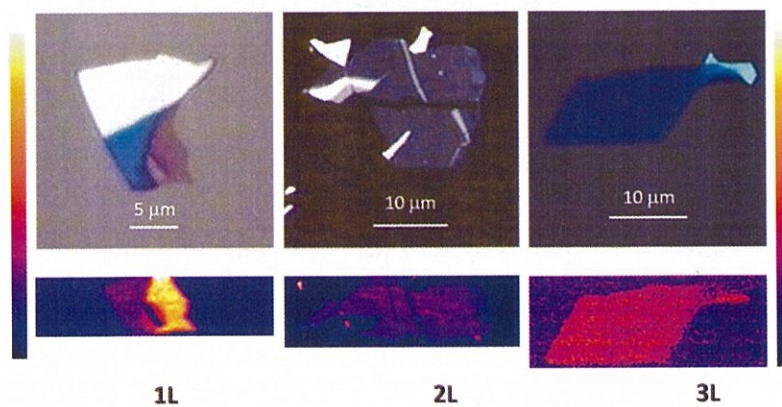
Figure 3.5 Optical contrast and PL mapping of 1L, 2L and 3L of MoS_2.

Figure 3.5 shows the PL mapping of monolayer (1L) and few layer (2 - 3L) MoS_2 on sample substrate. Noted that the contrast of the TMDs flake is vary with the substrate used. I can identify the layer number of samples by seeing the optical contrast (Figure 3.5 upper panel) and the brightness of the PL mapping (Figure 3.5 bottom panel). The variation of the contrast and color of the mapping with respect to the mapping scale (at right and left of the Figure 3.5) with blue-black to yellow-white is equal to the weak to strong PL intensity, respectively.

3.3.2.   UV-Vis Measurements

The UV-Vis spectrophotometer (UV-1800, Shimadzu Co.) as shown in Figure 3.6 is an equipment used for measuring an optical absorption of the thin-film reference dyes.

Figure 3.6 Photograph of UV-Vis spectrophotometer.
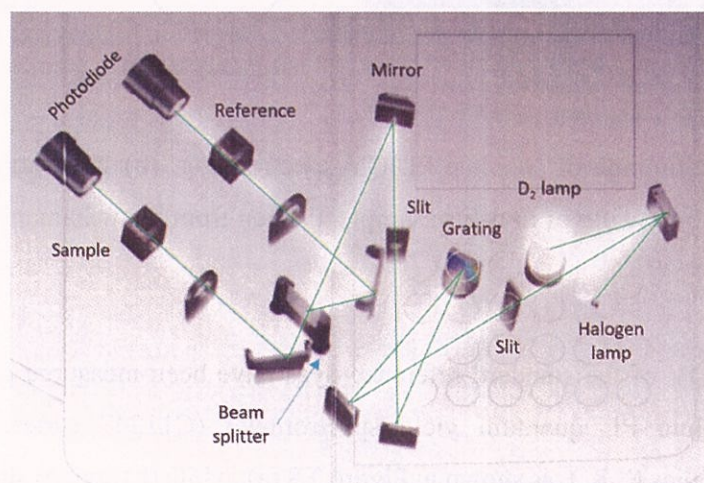
Figure 3.7 Optical Schematic of the UV-Vis spectrophotometer. (Reproduced from www.shimadzu.com).

Figure 3.7 shows the schematic of optical layout in the UV-Vis spectrophotometer. The combination of deuterium (D_2) and halogen lamp is used for light source in $190 - 1100 \pm 0.3$ nm. The two-light sources are crucial in the UV-Vis spectrophotometer since the measured wavelength range should be covered from UV to near-infrared region. The white light

(monochromatic light) from the lamps was selected by the diffraction grating (grating) and simultaneously separated into two optical paths for the transmissions of sample and reference photodiode, respectively. The absorption spectrum of the blank substrate (as reference or background) was firstly measured before the reference dye film, to obtain the baseline for the spectrum correction. Then, the detected spectra were recorded by the specific software of UVProbe in the personal computer which directly connected to the spectrophotometer.

3.3.3.   Absolute QY Measurements of the Reference Dyes
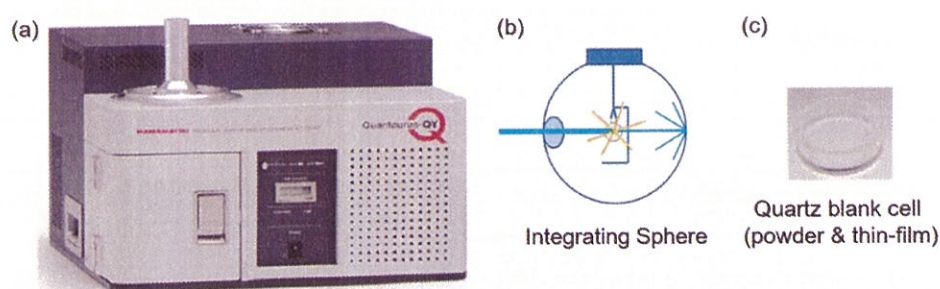
Figure 3.8 (a) Photograph of absolute PL QY spectrometer. (b) Integrating sphere, and (c) quartz blank cell for powder of thin-film sample. (Taken from www.hamamtsu.com).

Absolute QY of the standard reference dyes have been measured and determined by commercial absolute PL quantum yield spectrometer (C11347 series, Quantaurus-QY, Hamamatsu Photonics K. K.), as shown in Figure 3.8 (a), while (b) and (c) show the integrating sphere and quartz blank cell that can be used for powder and thin-film sample, respectively.

Figure 3.9 shows the schematic diagram of the absolute QY spectrometer. The spin-coated thin-film dye sample on the transparent substrate was firstly inserted in the quartz blank cell, in the integrating sphere. A monochromatic light from 150 W xenon lamp through an optical fiber was employed to be an excitation light to excite the dye sample. The integrating sphere with a 3 inch inner diameter was adopted which contained baffle between the sample cell and exit of detection position, to prevent direct exposure and detection from the scattered excitation light (blue solid line) and/or emission (red solid line) from the sample. The signals including the spectra of excitation light and PL were detected by back-thinned CCD

sensor [158,172]. The data acquisition from the absolute QY measurement was automatically calculated using the dedicated software in the personal computer.
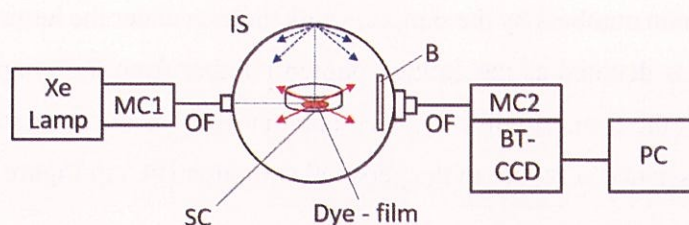
Figure 3.9 Schematic diagram of absolute QY spectrometer. The absolute QY spectrometer has integrated sphere (IS) system, with two monochromator (MC1 and MC2), optical fiber (OF), quartz blank cell (SC), baffle (B), back-thinned CCD (BT-CCD) and the personal computer (PC). (Reproduced from Ref. [158]).

▲ Excitation light on reference and sample and photoluminescence spectrum measurement example
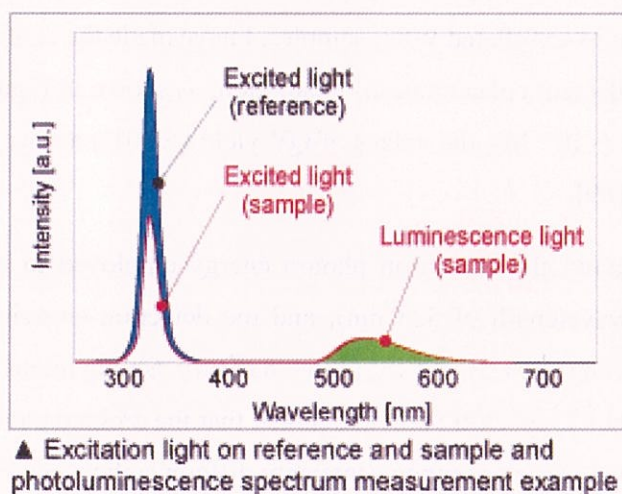
Figure 3.10 Data acquisition procedure of absolute QY measurement (absolute QY profile). (Taken from www.hamamtsu.com).

The principle calculation of the absolute PL QY from the absolute QY measurement is shown in Figure 3.10 as an example, with the y-axis is a fluorescence intensity as a function of wavelength. In this figure, the excitation wavelength is ~ 320 nm and the detection emission is in the range of 490 – 640 nm. The intensity different between the excited light from the reference (blank substrate) and the fluorescence dye sample (sample) – (blue area) is assigned

to the absorbed photon numbers by the sample, while the area under the luminescence spectrum curve (green area) is denoted as the emitted photon number from the sample. Therefore, the ratio of the latter to the former, will calculated automatically as the absolute QY value of the sample using the assigned software in the personal computer (PC) in Figure 3.9.

3.4. Results and Discussion

3.4.1. Absolute QY of Reference Dyes

The Rhodamine 6G (R6G) was firstly used for a reference dye to measure the relative quantum yield (QY) of as-exfoliated WSe_2 samples. I have made the confirmation of QY value using of R6G (with different concentration) in solution, as shown in Figure 3.11. In the lower concentration of R6G ($<10^{-4}$ M), the values of QY yield ($> 80\%$) are well consistent with the previously reported [169].

Figure 3.11 shows the excitation photon energy employed to excited the R6G dye sample is 2.33 eV (wavelength of 523 nm), and the detection emission of the dye in this experiment are in the range of $1.5 - 2.5$ eV ($495 - 830$ nm). Strong intensity which response to the large area under the PL spectrum curve, denoted that the emitted photon numbers is larger to than that of absorbed photon numbers (intensity difference between the excited light from the blank and the dye), thus the obtained absolute QY values is also higher for lower concentration of the R6G dye were observed.
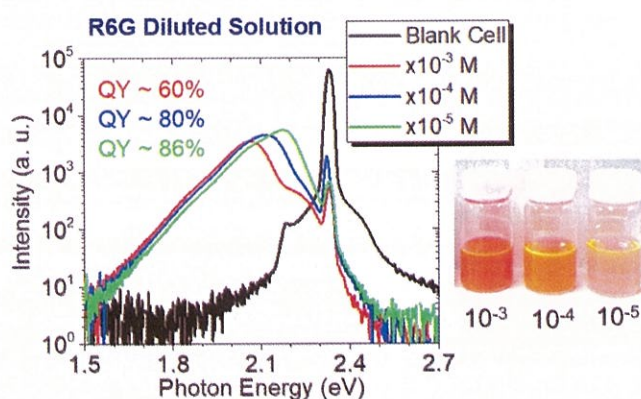
Figure 3.11 Absolute QY profile of R6G diluted solution.

It is well known that the high QY value of the R6G dye cannot be realized in a solid form. The absolute QY profile of R6G spincoated film in Figure 3.12 shows that there are no any PL peaks in the visible range (1.5 – 2.5 eV), which is in contrast with that in a solution (Figure 3.11). This is because that the aggregation of dyes in the solid form causes the PL (fluorescence) to quench [170]. I also measured the powder of R6G dye using higher excitation energy of 2.75 eV, and the very weak PL is observed at ~ 1.89 eV (656 nm). The inset of Figure 3.12 shows the absorption for blank cell and the R6G powder itself. The determined absolute QY of R6G powder was still less than 1%, which is not suitable for the R6G dye to be appointed as the reference dye for the evaluation of PL QY in the monolayer TMDs.
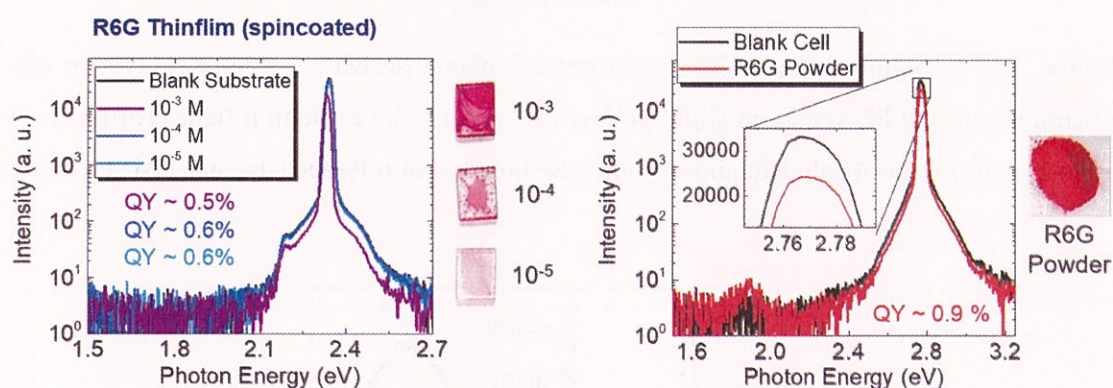
Figure 3.12 Absolute QY profile of R6G spincoated dye and R6G powder.

Then, I tested the absolute QY measurement of a highly emissive 3-borylbithiophene derivative ($C_{58}H_{49}BN_2S_4$), to achieve precise measurements of PL QY in the monolayer TMDs. Figure 3.13 shows the results of absolute PL QY of 3-borylbithiophene derivative as a reference dye (Dye) with respect to blank glass substrate (Blank) at photon energy of 2.33 eV (wavelength of 532 nm). The figure shows the excitation light profiles (light-green region) and PL spectrum (light-yellow region) of reference dye. The broad PL with center photon energy of 1.98 eV is observed in the spectrum.
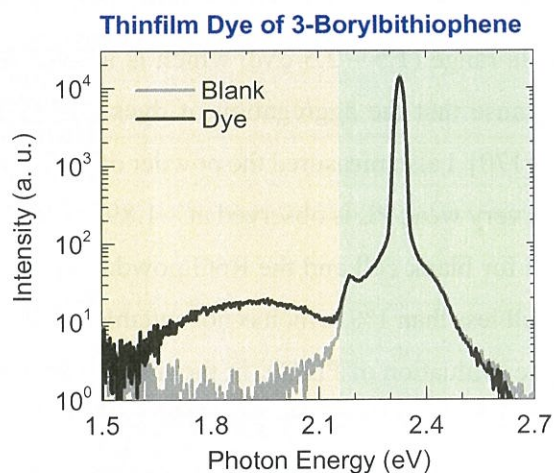
Figure 3.13 Absolute QY profile of 3-borylbithiophene derivative reference dye on glass substrate, with the PL spectrum (light-yellow region) and the excitation light profiles (light-green region) for the absolute quantum yield measurement of reference dye in a PMMA matrix.
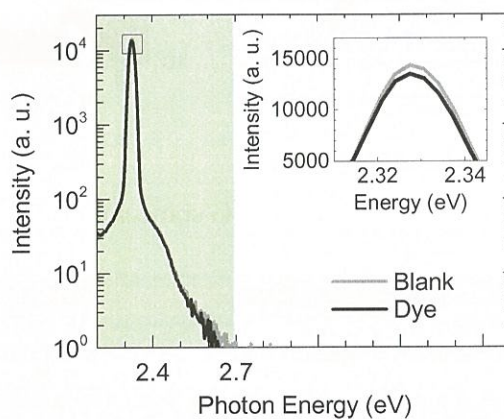
Figure 3.14 Excitation light profile of absolute QY in expended scale (inset).

The inset of Figure 3.14 exhibits the excitation light profiles of the dye, close-up from the rectangle in the Figure 3.14 (expended scale). The intensity difference of the excitation light with (Dye) and without (Blank) reference dye corresponds to the absorbed photon numbers, and the area of PL peak corresponds to the emitted photon numbers from the reference dye. Thus, from the ratio of emitted photon numbers and the absorbed photon numbers [158], the absolute PL quantum yield of the reference dye film, Φ_r on the glass and

the quartz substrate (absolute QY profile not showed) are measured about 36 % (0.359 ± 0.003) and 47 % (0.473 ± 0.008), respectively, where the high QY is kept in the solid form.

Figure 3.15 shows the optical absorption spectrum of reference dye in PMMA matrix using the UV-Vis spectrophotometer. The value of absorbance of the reference dye, Abs_r, at 2.33 eV (532 nm) shows relatively low value of ~ 0.003 ± 0.001 and this value is used for the evaluation of QY of monolayer TMDs. The value of the measured absorbance will denoted the absorbed photon flux which will be explained in the next sub-topic of 3.4.3.
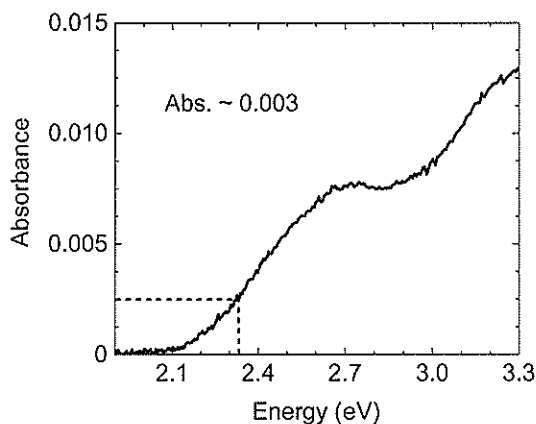
Figure 3.15 Absorption spectrum of reference dye.

3.4.2.   Optical Measurements of Monolayer WSe_2

Figure 3.16(a) shows the Raman scattering spectrum of monolayer WSe_2 on the glass substrate. The inset of Figure 3.16(a) is the optical image of the WSe_2 with the region inside the dotted lines corresponding to the monolayer of WSe_2. The typical intense Raman peak of E^1_{2g} and weak A_{1g} degenerated modes are observed at 250 and 262 cm^{-1}, respectively. The no distinct peak at 308 cm^{-1} which is the Raman active mode in bilayer, multilayer and bulk WSe_2, strongly suggests the monolayer TMDs of WSe_2 [122]. I also confirmed the layer number of WSe_2 from optical contrast and PL peak position [114], other than analyzing the characteristic of Raman peaks.
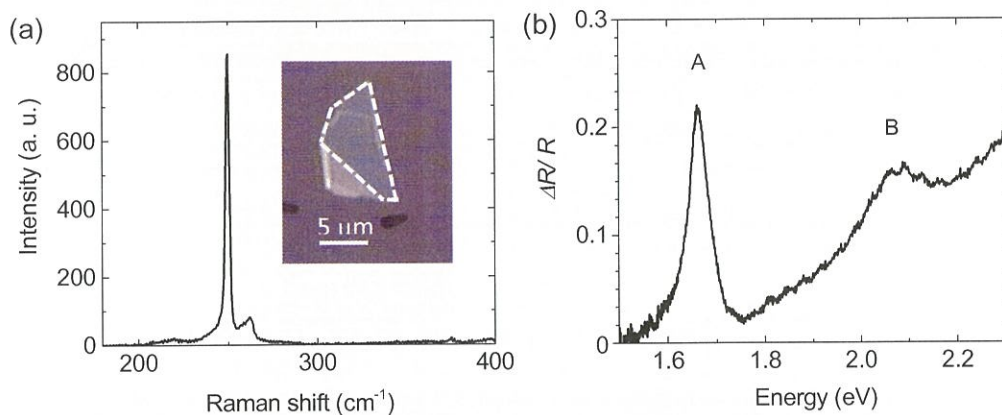
Figure 3.16 Optical image, Raman and differential reflectance spectrum of monolayer WSe_2. (a) Raman spectrum of monolayer WSe_2. The inset (dash-line) shows the optical image of measured monolayer WSe_2. (b) Differential reflectance spectrum of monolayer WSe_2. Peak A and B indicate the A and B exciton, respectively. Both spectra are on the glass substrate.

Figure 3.16(b) shows the differential reflectance $\Delta R/R$ spectrum of monolayer WSe_2 on the glass substrate. Several peaks (A and B) are observed in the differential reflectance spectrum corresponding to the optical transition of A and B exciton peak [128]. The distinct A exciton peak comes from the lowest optical transition in monolayer WSe_2 [68]. The value of optical absorption is evaluated from the value of differential reflectance spectrum at excitation energy of 2.33 eV using Eq. 2.26.
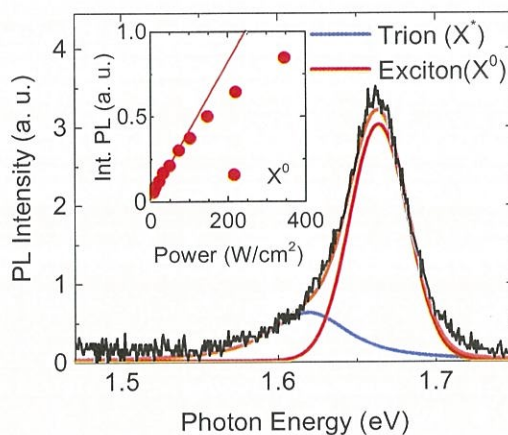
Figure 3.17 PL spectrum of monolayer WSe_2 with fitted line using Voigt function. PL spectrum of monolayer WSe_2 (black line) at low excitation power density of 36 W/cm^2. The

spectrum is fitted (orange line) using Voigt functions assuming the exciton and charged exciton (trion) peak. The inset shows the integrated PL intensity of monolayer WSe_2 as a function of power density, and the solid line indicates the linear relationship region.

Figure 3.17 exhibits the PL spectrum of the monolayer WSe_2. The spectral fitted results using Voigt functions are also shown with consideration of the exciton and charged exciton (trion) at 1.66 and 1.62 eV, respectively. The figure shows that the PL spectrum is dominated by the exciton emission in monolayer WSe_2 at linear excitation power density of 36 W/cm^2. Moreover, the contribution of trion for the spectrum is small amount of less than 20 %, which is negligibly small in the analysis. The inset of Figure 3.17 shows the integrated PL intensity of exciton in the monolayer WSe_2, as a function of excitation power density. The solid line represents the linear relationship of integrated PL intensity as a function of excitation power density. With increasing the excitation power density, the integrated PL intensity exhibits a nonlinear saturation behavior above around 100 W/cm^2 because of the strong exciton-exciton annihilation processes [135].

3.4.3. Estimation of Photoluminescence Quantum Yield of Monolayer WSe_2 with respect to Reference Dye

In order to estimate the PL QY of monolayer, multilayer and bulk transition metal dichalcogenides (TMDs) (MX_2, M = Mo, W, Re; X = S. Se), the relative QY method will be employed. The relative QY is measured by comparing normalized PL intensity of the sample and reference dye, using the QY of reference dye that is obtained from the absolute QY measurement. Here, I used the reference dye of 3-borylbithiophene derivative dye ($C_{58}H_{49}BN_2S_4$) with high QY and similar emission wavelength to monolayer TMD. Noted that the experimental conditions of optical studies should be carefully implement in the same condition. The excitation wavelength to measure the reference dye and monolayer TMDs in this study, is fixed to 2.33eV (532 nm), and the experiments are perform at weak excitation conditions where the PL intensity linearly increases with the excitation power density. All measurements were carried out at room temperature condition.

$$\Phi = \frac{\#\ \text{emitted photons}}{\#\ \text{absorbed photons}} = \frac{PL}{\text{Absorption}}$$

$$\Phi_{TMDs} = \left(\frac{A_{TMDs}}{f_{TMDs}} \div \frac{A_{Dye}}{f_{Dye}} \right) \times \Phi_{Dye}$$

where

A = linear gradient of Integrated Photon Flux vs. Power Density

f_{Dye} = Absorbance (Light absorption measurement (UV-Vis))

$f_{TMDs} = 1 - 10^{Abs.}$ $Abs. = \dfrac{\frac{\Delta R}{R} \cdot n^2 - 1}{4} \rightarrow \dfrac{\Delta R}{R} = \dfrac{4}{n^2 - 1} Abs.$

Figure 3.18 Formula of relative QY of TMDs sample. (Reproduced from Ref. [76,77,114]).

The method to estimate the PL quantum yield of monolayer WSe_2 using the QY relative method is described in Figure 3.18, where A is the linear gradient coefficient evaluated from the emission photon flux (PL per s per unit area) of the monolayer WSe_2 (TMDs) and the reference dye (dye), as a function of excitation power density. The absorbed photon flux at the excitation photon energy of 2.33 eV (532 nm wavelength) of f_{TMDs} is evaluated from differential reflectance ($\Delta R/R$) spectra, where f_{Dye} is obtained from the UV-Vis absorption measurement.
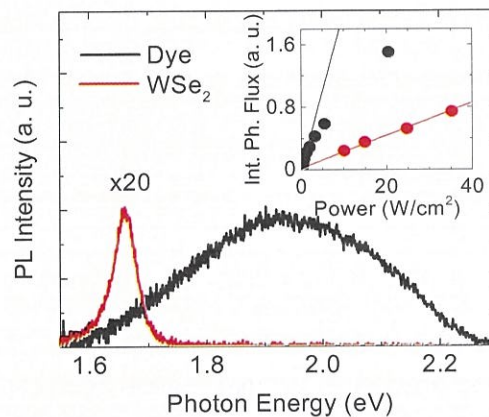
Figure 3.19 Comparative of PL spectra of reference dye and monolayer WSe_2. Both the PL spectra of reference dye and monolayer WSe_2 are excited using excitation power density of 1.3 and 36 W/cm^2, respectively. The inset shows the linear relationship of integrated photon flux as a function of power density for both reference dye and monolayer WSe_2.

Figure 3.19 shows the PL spectra of reference dye ($C_{58}H_{49}BN_2S_4$) (black solid line) and the monolayer WSe_2 (red solid line) on the glass substrate at low power conditions (linear region) of 1.3 W/cm^2 and 36 W/cm^2, respectively. The inset of Figure 3.19 shows the comparison of the integrated emission photon flux calculated from the PL intensities of reference dye (black-filled circle) and monolayer WSe_2 (red-filled circle) as a function of the excitation power density. Both gradient coefficient, A of reference dye and the monolayer WSe_2 depict linear power dependence at low power density conditions of < 5 W/cm^2.

I evaluated the PL quantum yield as 0.18 ± 0.03 % for the monolayer WSe_2 on the glass substrate at room temperature using equation in Figure 3.18. Moreover, the PL quantum yield of the monolayer WSe_2 on a quartz substrate is also determined using the same reference dye ($C_{58}H_{49}BN_2S_4$) on a quartz substrate (Φ_r = 47 % (0.473 ± 0.003)). The value of the PL quantum yield of the monolayer WSe_2 on quartz substrate is evaluated as 0.61 ± 0.08 %. In addition, the difference of quality in each monolayer WSe_2, the surface condition, difference in doping and charge transfer phenomena are suggested to cause the deviation of the PL quantum yields of the monolayer WSe_2 on the glass and quartz substrates.

3.5. Chapter Summary

As a summary of this chapter, I have evaluated the PL quantum yield of monolayer WSe_2 on transparent substrates at room temperature by employing highly emissive reference dye of 3-borylbithiophene derivative ($C_{58}H_{49}BN_2S_4$) in a PMMA matrix. Using the reference dye film on the glass (quartz) substrates with the high absolute quantum yield of 36% (47%), I have successfully evaluated the PL quantum yield of mechanically exfoliated monolayer WSe_2 as 0.18 ± 0.03 % and 0.61 ± 0.08 % on glass and quartz substrate, respectively. My finding also helps to provide insight information on evaluation methods of quantum yield for solid samples.

Chapter 4. Long Effective Exciton Radiative Lifetime of TMDs

4.1. Introduction

In Chapter 2, the elementary excitation – electron-hole pair (exciton) in the monolayer TMD has large binding energy about several hundred meV [70,71,173]. This extraordinary nature of the elementary excitation compared to those of other semiconductor materials [174–176] makes the stable bound exciton formation even at room temperature due to strong Coulomb interactions, which provides the novel optical properties of this material. The monolayer TMDs representing a model system of 2D materials have been received a lot of attention, because they are directly band gap semiconductors, and are expected to be superior light emitters in the visible range [22,33,127] [30,177] and other optoelectronic devices [10,11,178,179]. For the optoelectronic applications, it is essential to know the radiative lifetimes of excitons [129], because it reflects the strength of light–matter interaction [11,180,181] and the light-emission efficiency, such as PL quantum yield. The PL quantum yields of as-exfoliated TMDs have been reported to be very low because of high defect densities and large nonradiative recombination rates [22,33,73].

In this chapter, I have extend the studies of PL QYs to other members of group VI of 2D semiconductors TMDs such as MoS_2, $MoSe_2$ and WS_2. The main objective of this chapter is to experimentally evaluate the effective exciton radiative lifetimes of TMDs of MX_2 (M = Mo, W: X = S, Se) from simultaneous measurements of the PL QY and the PL decay time at room temperature. The experimentally evaluated PL QYs in comparison with the theoretically calculated results, were further discussed in the basis of long radiative lifetime of bright excitons at low temperature limit, a finite coherence area and the populations of dark exciton states. Explicitly, the PL quantum yield in this chapter is ascribed to the A exciton quantum yield (exciton quantum yield) which resonant to the exciton emission in this TMDs materials.

4.2. Methodology – Samples Preparation

The monolayer samples of TMDs, MoS_2, $MoSe_2$, WS_2 and WSe_2 were prepared using mechanically exfoliated method onto transparent of quartz substrate. Due to the weak PL

intensity and the PL QY as well as the PL decay time of monolayer MoS_2 compared to other TMDs monolayer, I have treated the monolayer MoS_2 with the chemical superacid of bis(fluoromethane)sulfonimide (TFSI) [75].
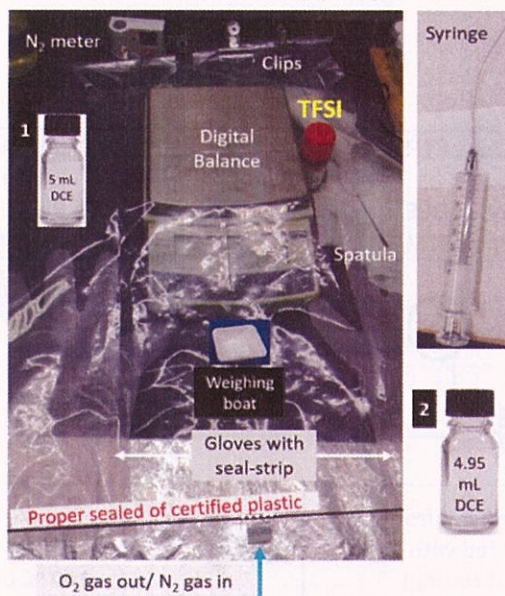
Figure 4.1 Experimental setup for preparing the TFSI solution. Note that step 1 and 2 referring to bottle 1 and 2, respectively; DCE = 1,2-dichloroethane (Sigma-Aldrich); and TFSI/DCE = mixed solution of TFSI and DCE.

I have carefully treat the superacid TFSI (Sigma-Aldrich), and carry out an experimental procedures of TFSI diluted solution in the glove-bag (Figure 4.1). The nitrogen (N_2) gas should be purged to fully replace the oxygen (O_2) gas inside the glove bag. Since the TFSI solid powder is highly reactive and evaporated very fast even in N_2 gas (in Figure 4.1), I transferred neatly and immediately the 100 mg of TFSI in the weighing boat, then I mixed the diluted solution of 20 mg/mL – TFSI and 1,2-dichloroethane (DCE) (Sigma-Aldrich), in the bottle 1 (Figure 4.1) which denoted as 1 in the flowchart of Figure 4.2. After that, only 0.05 mL from the 20 mg/mL of diluted TFSI/DCE was added to other bottle of DCE (bottle 2) with 4.95 mL, to make the mixed solution of 0.2 mg/mL of TFSI/DCE. This step shown as 2 in Figure 4.2, and followed by the next step 3 – 5 are perform outside the glove-bag. The monolayer MoS_2 on the substrate was immersed in the TFSI in DCE solution and annealed at

100°C on hotplate for 15 minutes. After the blowing the substrate by N_2 gas without rinsing, the substrate then annealed at 100 °C for 5 minutes. The detail procedure of TMDs-TFSI treatment [75] is summarized in Figure 4.2.
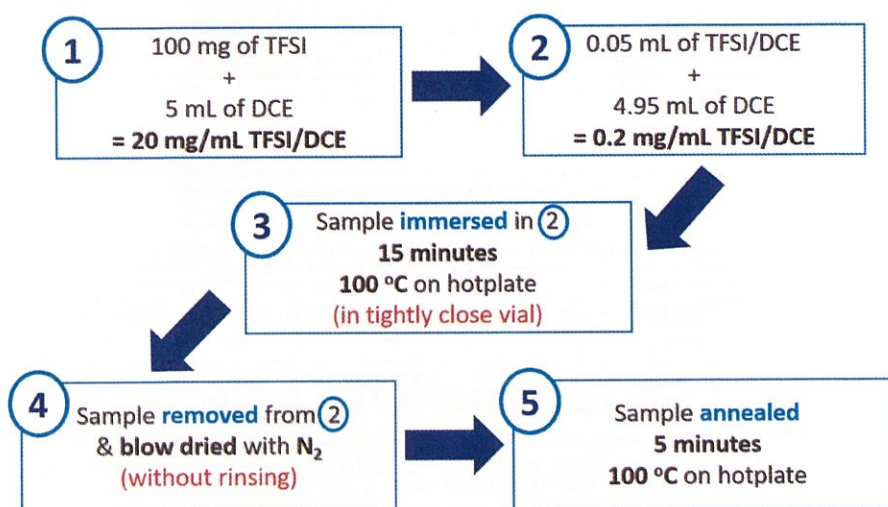
Figure 4.2 Flowchart of TMDs-TFSI treatment.

4.3. Sample Characterizations

4.3.1.   PL, Raman and Differential Reflectance of TMDs

The optical measurements of PL, Raman scattering and differential reflectance ($\Delta R/R$) spectra of monolayer MX_2 (M = Mo, W; X = S, Se) were carried out mainly by using micro-Raman system (Nanophoton, RAMANTouch) as explained in chapter 3.3.1, while the time-resolved PL (TRPL) were implement to measure the PL decay of the samples at room temperature.

4.3.2.   Time-Resolved Photoluminescence (TRPL)
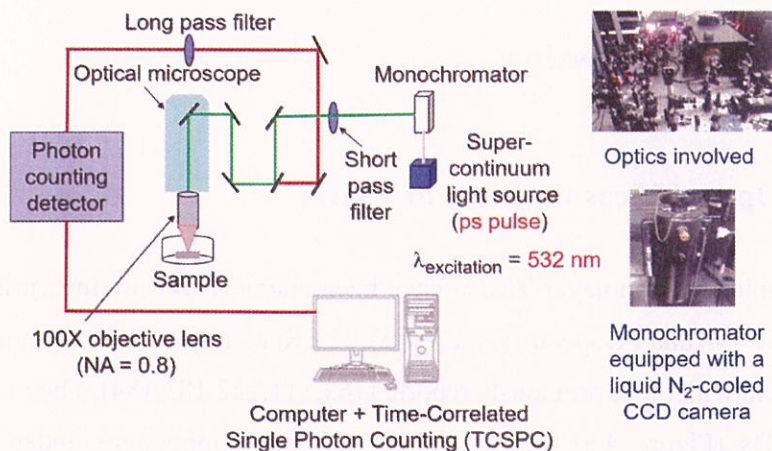
Figure 4.3 The setup of the time-resolved photoluminescence (TRPL) with TCSPC technique.

The TRPL were executed using a homemade setup equipped with a monochromatic super-continuum light source (~20 ps) (WL-SC480-4, Fianium) with an excitation wavelength of 532 nm and a repetition rate of 40 MHz. The schematic of TRPL measurement setup is shown in Figure 4.3. The focused spot size on the sample was ~2 μm in this setup. The PL signal was detected by a monochromator equipped with a liquid-N_2-cooled charge-coupled device (CCD) camera. The PL decay profiles were recorded by a time-correlated single-photon counting (TCSPC) technique using a single-photon avalanche Si photodiode. The instrumental response function (IRF) of this setup was ~70 ps.

The TRPL is measured by time-correlated single photon counting (TCSPC) method, which provides the information on the photocarrier (exciton) dynamics of the semiconducting materials [182] such as TMDs in the picosecond/ nanosecond time-range region. The concept of TCSPC methods is that the accumulation of arrival time of emitted photon from the sample against the excited pulsed laser to the sample is measured. The occurrence of the emission over time after the excitation pulse corresponds to the PL decay due to the recombination of electron-hole pair (exciton) of the sample [92,182].

4.4. Results and Discussion

4.4.1.   Optical Measurements of TMDs

The samples of monolayer TMDs have been characterized by measuring the Raman scattering (Figure 4.4) and PL spectra (Figure 4.5). The Raman spectra for all monolayer TMDs are well consistent with those previously reported [63,111,122,183,184]. The PL spectra of the monolayer TMDs (Figure 4.5) were collected at room temperature under weak (linear) excitation power condition to avoid nonlinear effects. The PL peaks (exciton energy, E_x) were observed at 1.88, 1.57, 2.01, and 1.66 eV for monolayer MoS_2, $MoSe_2$, WS_2, and WSe_2, respectively, in good agreement with those previously reported [38,114,177].
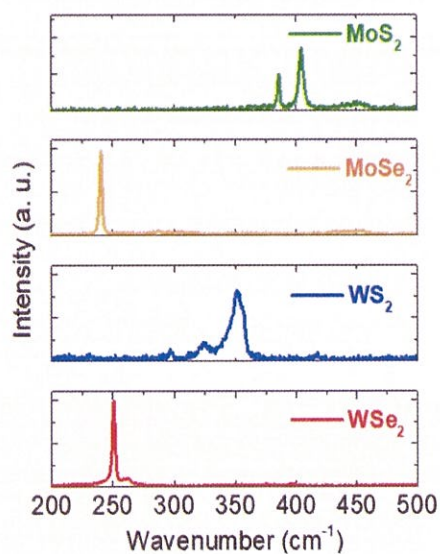
Figure 4.4 Raman scattering spectra of monolayer TMDs, MX_2 (M = Mo, W; X = S, Se).
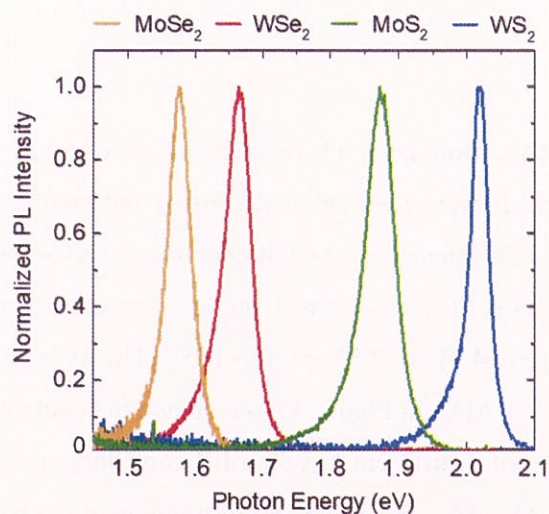
Figure 4.5 Normalized PL spectra of monolayer TMDs MX_2 (M = Mo, W; X = S, Se) at room temperature.
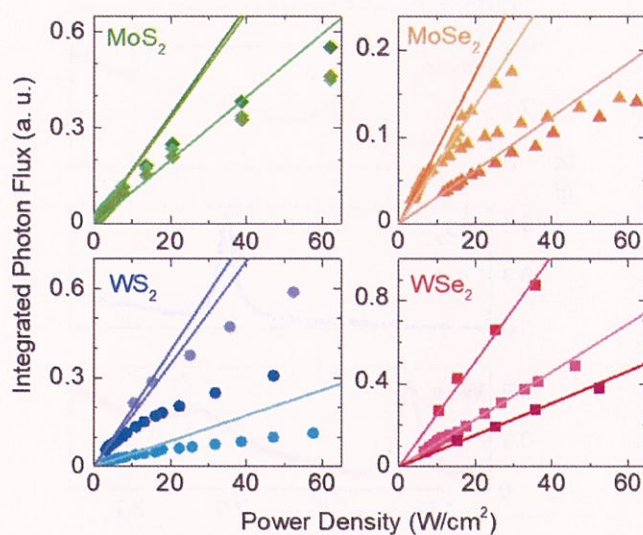
Figure 4.6 Integrated photon flux as a function of power density for monolayer TMDs. The data sets from three different monolayer samples of each MX_2 are shown. The solid lines indicate the linear relationship between the integrated photon flux and the excitation power density for each sample.

The PL spectra of the monolayer TMDs were recorded by varying the excitation power density. The quantum yields were then calculated using the gradients of the emitted photon fluxes from the integrated PL intensities of exciton emission (X) at the linear excitation region in Figure 4.6 as a function of the absorbed photon densities evaluated from differential reflectance spectra (Figure 4.7) at 2.33 eV [76,155]. The data sets from three different monolayer samples for each MX_2 in Figure 4.6 are shown in Figure 4.8. Figure 4.8 shows the optical microscope image of 3 different sample (different flake, point and substrate) of each monolayer TMDs MX_2, M = Mo, W; X = S, Se. Variations in the data are observed even for the same monolayer MX_2 because of fluctuations induced by imperfections (strain, defects, and vacancies) and carrier densities.
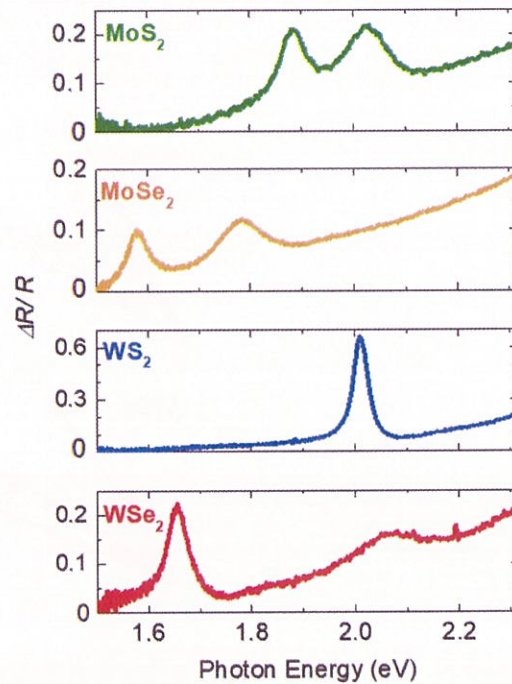
Figure 4.7 Differential reflectance spectra of monolayer TMDs.
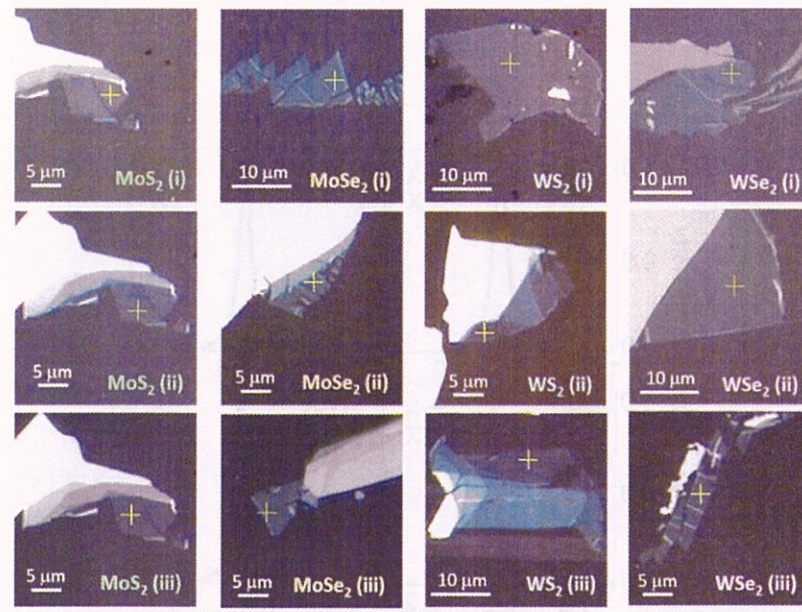
Figure 4.8 Optical microscope of monolayer TMDs on quartz substrates. The cross symbols in the images denote the positions of the PL and Raman measurements.

4.4.2.   PL Spectral Fitted and Linewidth Estimation

Figure 4.9 exhibits the normalized PL spectra of monolayer MoS_2, $MoSe_2$, WS_2, and WSe_2, and the spectral fitting results obtained using Voigt functions [185] with homogeneous and inhomogeneous broadening assumed to be Lorentzian and Gaussian functions, respectively [186,187]. Each PL spectrum is composed from the exciton (X) and charged exciton, trion (X*) emissions. The spectral shape of the experimentally obtained PL spectra for each monolayer TMD is well reproduced by the fitting results obtained assuming inhomogeneous broadening of 5–15 meV, as reported previously [177,187,188]. Here, I used the PL linewidth of monolayer TMDs at cryogenic temperature (~5 K) as the values of inhomogeneous broadening, which were mainly determined by the temperature-independent impurity (defect) scattering of excitons and by the inhomogeneity of the exciton energy [189].
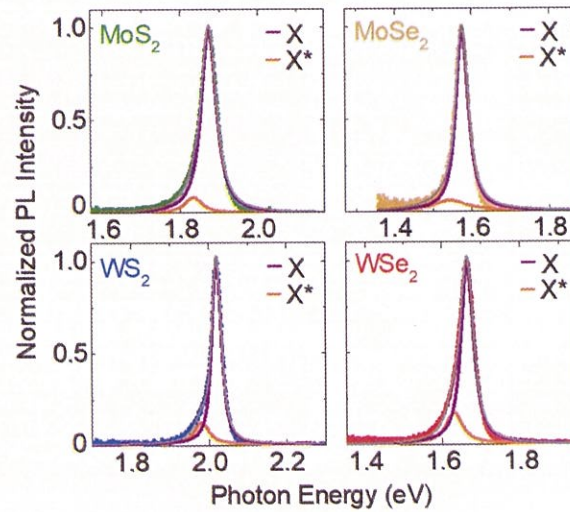
Figure 4.9 Normalized PL spectra of monolayer TMDs with PL spectral fitted using Voigt function. The X and X* denote the exciton (orange) and trion (purple) emission, respectively.

From the spectral fitting results, the homogeneous linewidth of the excitons, Δ, for monolayer MoS_2, $MoSe_2$, WS_2, and WSe_2 at room temperature was evaluated as 45.4 ± 0.3, 38.3 ± 0.3, 28.2 ± 0.5, and 38.8 ± 0.3 meV, respectively. These values are approximately consistent with the previously revealed values [165,177,190]. Moreover, the energy separation between the X and X* emissions, as determined from the fitted results, ranges from 30 to 40 meV. These values are also consistent with the previously reported values, which also supports the validity of the spectral analysis [38,177,191,192]. Notably, the PL spectra of TMDs studied here are dominated by the exciton emission (X) at room temperature.

4.4.3.   Evaluation of Exciton Quantum Yield of TMDs

As briefly noted in the introduction of this chapter, I have estimated the PL quantum yield of monolayer TMDs by ascribing to the A exciton emission. Here, I define the PL quantum yield from A exciton as exciton quantum yield, because the characteristic carrier relaxation process occurs due to the band nesting in the monolayer TMDs. The excitation energy of 2.33 eV in this experiment corresponds to the higher-energy states than B excitons in all the monolayer TMDs studied here. All of the photoexcited electron–hole pairs do not relax to the lowest A exciton energy state contributing to the radiative emission because some

of the photoexcited electron–hole pairs are spontaneously separated in the k-space (the relaxation pathways toward the Λ-point for electrons and toward the Γ-point for holes) due to the existence of nested bands (band nesting) in the monolayer TMDs, as explained in Chapter 2.2.6 [31,144]. As a consequence, with consideration of the band nesting and variations of the PL intensity in each monolayer MX_2 using the relations;

$$\Phi = \frac{\Phi_{raw}}{BN},$$

Eq. 4.1

the Φ of the monolayer MoS_2, $MoSe_2$, WS_2, and WSe_2 were evaluated as 0.68 ± 0.13, 0.79 ± 0.30, 0.47 ± 0.23, and $0.45 \pm 0.24\%$, respectively, at room temperature.

4.4.4.   PL Decay Measurements of TMDs
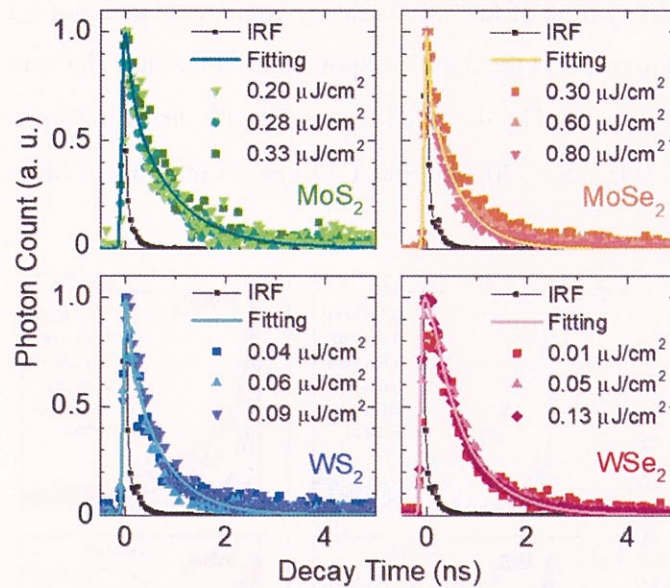
Figure 4.10 PL decay profiles of monolayer TMDs at room temperature in the linear excitation power density regime. The black square indicates the IRF of the experimental setup.

Figure 4.10 shows the instrument response function (IRF) of the experimental setup and the PL decay profiles for monolayer TMDs at linear excitation power regions, whereas the Figure 4.11 shows the PL decay profiles of monolayer MoS_2, $MoSe_2$, WS_2, and WSe_2 on quartz substrates at different excitation power densities. In my study, I only concentrate on the linear region of the emission, means in the weak and linear power excitation density. This is because

we want to prevent the other effect to the sample such as exciton – exciton annihilation (at high and saturated power excitation region) which will drastically affected our calculation for exciton radiative lifetime (will explained in next sub-chapter). Shortening of the PL decay due to an exciton–exciton annihilation process [135] was observed at higher excitation power densities (>0.3 μJ/cm^2) in Figure 4.11.

The solid lines in both Figure 4.10 and Figure 4.11 is corresponds to the curves fitted by the convolution of a double-exponential function and the IRF. The average PL lifetimes were calculated as follows,

$$\tau_{PL} = A_1 \tau_f + A_2 \tau_s,$$

<div align="right">Eq. 4.2</div>

where τ_f (τ_s) is the decay time of fast (slow) decay component and A_1 (A_2) is the amplitude of fast (slow) decay component in the double-exponential functions. The experimental results for each TMD are well reproduced by the fitted curves. The PL decay lifetimes, τ_{PL} were evaluated as 420 ± 110, 360 ± 100, 220 ± 70, and 380 ± 130 ps for monolayer MoS$_2$, MoSe$_2$, WS$_2$, and WSe$_2$, respectively.
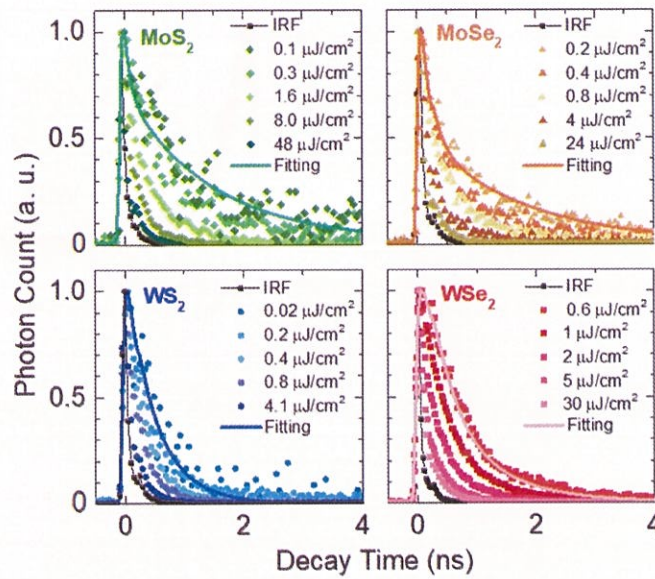
Figure 4.11 Normalized PL decay profiles of monolayer TMDs at various excitation power densities, and IRF. The solid lines correspond to the curves fitted by double-exponential functions.

4.4.5. Determining the Effective Excitons Radiative Lifetimes of TMDs

Effective radiative lifetimes of excitons, τ_{rad}, in this study represent the experimentally measured radiative lifetimes of excitons, calculated from the relation of the obtained PL decay time, τ_{PL}, and the exciton quantum yield, Φ, using the equation of $\tau_{rad} = \tau_{PL} / \Phi$ [73,193,194]. By employing this relationship, the τ_{rad} values were evaluated as 61 ± 8, 36 ± 9, 55 ± 18, and 93 ± 27 ns for monolayer MoS_2, $MoSe_2$, WS_2, and WSe_2, respectively, at room temperature. The values of Φ, τ_{PL}, and τ_{rad} for the studied monolayers are summarized in Table 4.1.

Table 4.1 Values of band nesting (BN) at an excitation energy of 2.33 eV [31], PL quantum yield (Φ_{raw}), exciton quantum yield (Φ), PL decay time (τ_{PL}), and effective radiative lifetime (τ_{rad}) of monolayer TMDs.

TMDs	Band Nesting (BN)*S1)	Φ_{raw} (%)	Φ (%)	τ_{PL} (ps)	τ_{rad} (ns)
MoS$_2$	0.67	0.34	0.50 ± 0.05	310 ± 20	62 ± 8
		0.50	0.74 ± 0.08	380 ± 50	51 ± 9
		0.54	0.81 ± 0.09	570 ± 70	70 ± 12
			Ave.: 0.68 ± 0.13	Ave.: 420 ± 110	Ave.: 61 ± 8
MoSe$_2$	0.22	0.24	1.10 ± 0.04	480 ± 20	44 ± 2
		0.19	0.87 ± 0.03	230 ± 20	27 ± 2
		0.09	0.39 ± 0.01	-	-
			Ave.: 0.79 ± 0.30	Ave.: 360 ± 100	Ave.: 36 ± 9
WS$_2$	0.71	0.10	0.15 ± 0.02	120 ± 20	81 ± 6
		0.42	0.59 ± 0.06	250 ± 20	42 ± 6
		0.47	0.67 ± 0.07	290 ± 30	43 ± 7
			Ave.: 0.47 ± 0.23	Ave.: 220 ± 70	Ave.: 55 ± 18
WSe$_2$	0.80	0.28	0.35 ± 0.04	450 ± 10	129 ± 16
		0.19	0.23 ± 0.03	200 ± 20	85 ± 14
		0.62	0.78 ± 0.09	500 ± 20	64 ± 8
			Ave.: 0.45 ± 0.24	Ave.: 380 ± 130)	Ave.: 93 ± 27

The evaluated τ_{rad} values at room temperature are relatively long—on the order of several tenths of a nanosecond, which is similar to the previously reported values for mechanically as-exfoliated [73,195] and chemically treated monolayer TMDs [75,126]. In

contrast, the relatively long effective exciton lifetimes on the order of several tenths of a nanosecond is much differ from the theoretically predicted values of ~ 1 ns at room temperature [129,196]. Our long effective exciton radiative lifetimes are explained in consideration of (1) the long radiative lifetime of bright excitons at low temperature limit, (2) a finite coherence area and, (3) the populations of dark exciton states. Figure 4.12 shows the simple model to understand the factors contributed to the longer exciton lifetimes, as I estimated by the theoretical predicted values and will be discuss accordingly.
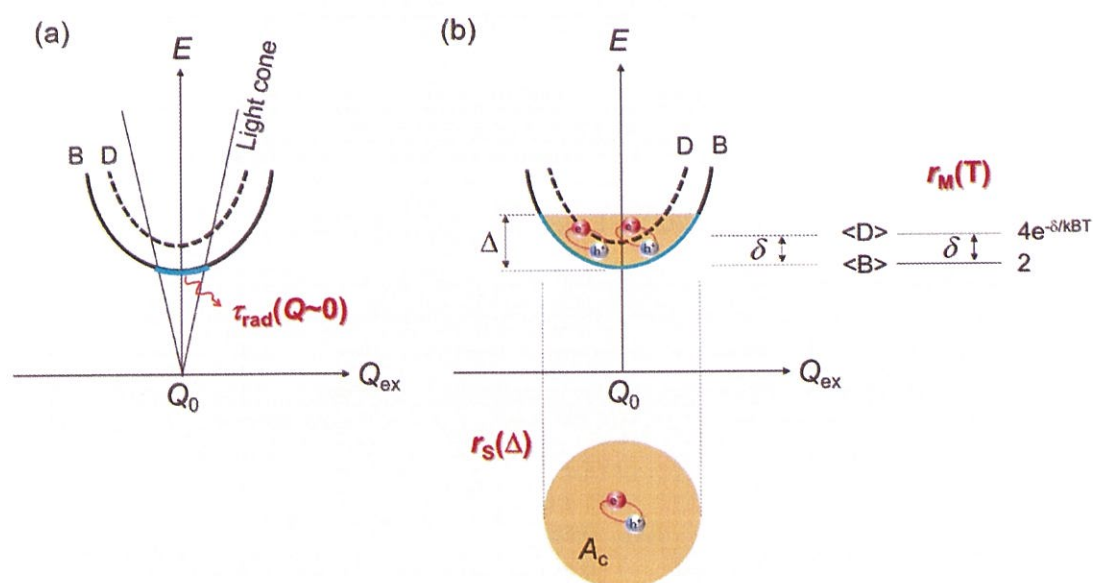
Figure 4.12 Schematic model of TMDs long effective exciton radiative lifetimes; (a) at low temperature limit, $\tau_{rad}(Q\sim0)$, and (b) as a consequence of finite coherence area, A_c and population of dark exciton state, r_M, where E is energy, Q_{ex} denotes as exciton momentum, Δ is set as the homogeneous linewidth, and the δ is energy splitting distance between the bright (B) and dark exciton state (D).

In order to understand our experimentally obtained results, here I calculated the effective radiative lifetime of excitons at finite temperature, $\tau_{eff}(T)$ with consideration of exciton momentum distribution, and effect of dark exciton states. The experimentally observed $\tau_{eff}(T)$ values do not simply correspond to that of the singlet bright exciton at $Q_{ex}\sim0$ as $\tau_{rad}(Q\sim0)$, where Q_{ex} is the exciton momentum as shown in Figure 4.12(a). This is because the oscillator strength of $Q_{ex}\sim0$ exciton is shared by all states within the finite homogeneous linewidth $\Delta(T)$

because of the uncertainty of Q_{ex} induced by the dephasing process, which changes the radiative lifetime of the exciton as a factor of $r_S(\Delta)^{-1}$ (Figure 4.12(b)). Moreover, not only the thermalization within each single exciton band but also the exciton distribution among the singlet bright states and other states, including the dark states, further elongates the radiative lifetime of the exciton as a factor of $r_M(T)^{-1}$. Figure 4.12(b) only shows the band structure of Mo-based TMDs (e.g. MoS_2 and $MoSe_2$), where the dark exciton state are higher than the bright exciton state. In contrast, the dark exciton states of W-based TMDs (e.g. WS_2 and WSe_2) were observed to locate below the bright state (lower-lying dark states) [143]. Thus, the $\tau_{eff}(T)$ with consideration of three factors mentioned is described as

$$\tau_{eff}(T) = \tau_{rad}(Q\sim 0) \cdot r_S(\Delta)^{-1} \cdot r_M(T)^{-1}.$$

Eq. 4.3

Moreover, the factors of r_S and r_M are elaborated as,

$$r_S(\Delta) = \frac{2\pi E_x^2}{M_x \Delta c^2},$$

Eq. 4.4

$$r_M(T) = \frac{2}{2 + 4e^{-\delta/k_B T}},$$

Eq. 4.5

where temperature T is 300 K, M_x is the exciton mass, c is the speed of light, k_B is the Boltzmann constant, and δ is the energy splitting between the bright and dark exciton states, which is approximately +3, +21, −27, and −38 meV for MoS_2, $MoSe_2$, WS_2, and WSe_2, respectively [142]. The positive (negative) signs denote the position of the dark exciton state as being above (below) the bright exciton state. The calculated values of $r_S(\Delta)$ and $r_M(T)$ (with consideration of both K and K' valleys of TMDs) are presented in Table 4.2. The exciton coherence area, A_c, which is defined by the area over which the excitons capture the oscillator strength, is deduced as $r_S = Q_0^2 A_c$, where $Q_0 = E_x/\hbar c$ [129] is the momentum of a photon with an energy equal to the exciton energy. Meanwhile, A_c is described as Eq. 4.6 [197], and the calculated coherence areas of excitons range from 3 to 5 nm^2 at room temperature in monolayer TMDs, as also shown in Table 4.2.

$$A_c = \frac{2\pi \hbar^2}{M_x \Delta},$$

Eq. 4.6

The values of $\tau_{rad}(Q\sim 0)$ are approximately the same for monolayer MoS_2, $MoSe_2$, WS_2, and WSe_2, and are evaluated as 0.23, 0.24, 0.19, and 0.22 ps, respectively, as derived from theoretical studies [196]. However, the values of τ_{eff} calculated from Eq. 4.3 using the theoretically predicted values of $\tau_{rad}(Q\sim 0) < 1$ ps are 0.72 ± 0.03, 0.64 ± 0.06, 0.71 ± 0.04, and 2.55 ± 0.02 ns for monolayer MoS_2, $MoSe_2$, WS_2, and WSe_2, respectively, at room temperature.

These values are more than one order of magnitude smaller than the experimentally obtained values, as shown in Table 4.1. The quantitative differences between the theoretically predicted $\tau_{rad}(Q{\sim}0)$ and the experimentally obtained values might arise from weak localization of excitons in 2D monolayers at low temperatures [129]. Here I employed values of $\tau_{rad}(Q{\sim}0)$ for monolayer TMDs of 2–10 ps, as obtained from the time-resolved PL at low temperatures [63,198,199]. The calculated radiative lifetimes of excitons from eq. (1) using $\tau_{rad}(Q{\sim}0)$ of 8 ps [199] are 25 ± 1, 21 ± 2, 30 ± 2, and 93 ± 1 ns for MoS_2, $MoSe_2$, WS_2, and WSe_2, respectively, which are almost consistent with the experimental results, as shown in Table 4.1.

Table 4.2 Homogeneous linewidth (Δ), coherence area (A_c), $r_s(\Delta)$ and $r_M(T)$, and calculated effective exciton radiative lifetime (τ_{eff}) of monolayer TMDs as obtained using $\tau_{rad}(Q \sim 0) = 8$ ps [199].

TMDs	Δ (meV)	A_c (nm^2)	r_s ($\times 10^{-5}$)	r_M	τ_{eff} (ns)
MoS_2	45.4 ± 0.3	3.13 ± 0.07	89 ± 4	0.3595	25 ± 1
$MoSe_2$	38.3 ± 0.3	3.36 ± 0.15	71 ± 6	0.5286	21 ± 2
WS_2	28.2 ± 0.5	4.14 ± 0.13	178 ± 11	0.1504	30 ± 2
WSe_2	38.8 ± 0.3	3.43 ± 0.02	83 ± 1	0.1039	93 ± 1

The experimentally obtained and theoretically calculated results are summarized in Table 4.1 and Table 4.2, respectively. The deviation of $\tau_{eff}(T)$ of monolayer WSe_2 compared to other TMDs is caused by combination effects from homogeneous linewidth, Δ due to dephasing process, the exciton mass, M_x [70], as well as the splitting between the dark and bright state, δ.

4.5. Chapter Summary

As a summary to this chapter, I have investigated the effective radiative lifetimes of monolayer TMDs of MoS_2, $MoSe_2$, WS_2, and WSe_2 at room temperature. The considerably

long effective radiative lifetimes of exciton (> 10 ns) at room temperature were evaluated and determined from exciton quantum yields of 10^{-2} to 10^{-3} and PL decay lifetimes of several hundred picoseconds. The long effective radiative lifetimes of monolayer TMDs at room temperature are suggested to be affected by the long radiative lifetime of bright exciton at low temperature limit, the distribution of singlet exciton population in other states, including the dark states, and a finite exciton coherence length (area) or several square nanometers. The findings are expected to provide crucial information about exciton dynamics for the future development of optical applications based on monolayer TMDs.

Chapter 5. PL Quantum Yields for Thin-Layered ReS₂: Identification of Indirect Band Gap Semiconductors

5.1. Introduction

Rhenium dichalcogenides (ReX_2, X = S, Se) is a member of two-dimensional (2D) atomically thin-layered semiconductors of transition metal dichalcogenides (TMDs). They are observed to be distinguish from other TMDs members as they have anisotropic structured, which response strongly and exactly to the angle of incident light, strained and Re-chain (b-axis) [44,45]. Rhenium disulfides, ReS₂ has been studied for the past two decades due to the optical and electrical anisotropic of its bulk counterparts [49,52,200–202]. Just recently, the thinner layered until its monolayer part has been discovered to have their own attractive properties, especially in optoelectronic devices, such as field-effect transistor, photodetectors [203,204], optical waveplates [61], thermoelectric and piezoelectric devices [205], by manipulating its flexible, birefringence and anisotropic optical properties [206,207].

The PL quantum yield (QY), Φ_{PL} has been described previously (in chapter 3.1) is the crucial parameter to determine the efficiency and performance evaluation of an optical device [208]. Different with the monolayer TMDs group VI, MX₂ (M = Mo, W; X = S, Se) which reported to have strong PL intensity, and hence its PL quantum yield due to the direct band gap semiconductors, instead of indirect band gap nature of their multilayer and bulk counterpart [22,33,145], the nature of the band gap two-dimensional (2D) ReS₂ semiconductor, are still under debate to-date [41,45,152,209].

In this chapter, I have properly examined and reported the PL QYs of thin-layered ReS₂ using circularly polarized light on transparent substrates at room temperature. The calculated PL QY for layered ReS₂ of monolayer (1L) to few-layer (2–7L) in the range of 10^{-4} are reported to be almost independent with regards of its layer number and the substrate occupied. This occurrence is proposed by no prominent band gap transition and indirect band gap semiconductor nature of thin-layered ReS₂, and the phenomenon is deviate to the previously reported monolayer-to-few-layer MoS₂, the prototype of TMDs group VI.

5.2. Methodology – Samples Preparation

The ReS_2 samples from mono to few layer (1–7L) were prepared using a mechanically exfoliation method, same as other previous TMDs samples in previous chapter. PL intensities of monolayer, multilayer as well as bulk ReS_2 are very weak, even when comparing to the monolayer as-exfoliated MoS_2. In order to enhance their PL intensity, I have consider a chemical-treatments method for verification of charge-carrier doping to the ReS_2 samples. A p-type dopant of F_4TCNQ (as ReS_2 is also confirm to be n-type semiconductor [203,210,211]) and a nonoxidizing superacid TFSI (as these chemical have been discussed previously in chapter 2.2.5) were utilized for the chemical-treatments of ReS_2 samples. The method preparation for the TFSI treatments have been explained previously in chapter 4.2, while the F_4-TCNQ – ReS_2 treatment is explained as follow:

The F_4TCNQ was prepared with the concentration of 0.02 μmol/ mL in toluene solution by using the bath type sonicator (As One Corporation) for 40 minutes. The diluted F_4TCNQ solution was then applied to the quartz substrate by drop-cast method with approximately 10 μL droplet on substrate area of 1 cm^2. The proper procedure to prepare the F_4TCNQ solution is summarized in Figure 5.1.
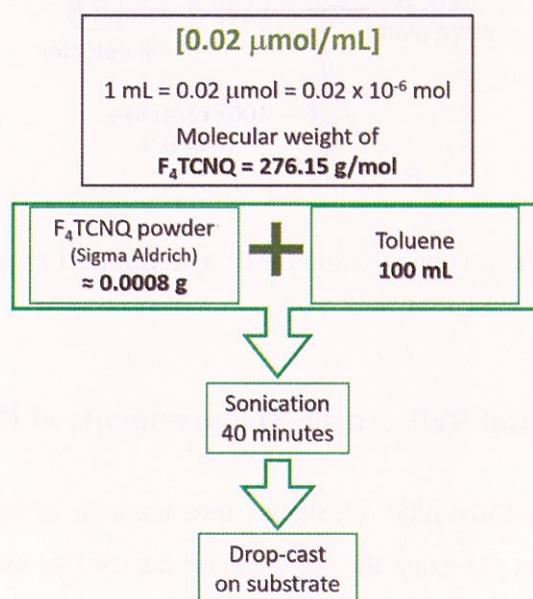
Figure 5.1 Procedure to prepare F_4TCNQ solution [38].

5.3. Sample Characterizations

5.3.1.   PL and Raman scattering of ReS$_2$

The PL and Raman scattering spectra of ReS$_2$ have been measured using micro-Raman system, Nanophoton (RAMANTouch) spectroscopy same as previously done for other TMDs (MX$_2$, M = Mo, W; X = S, Se) samples. But, I have specifically assisted with a quarter-wave (λ/4) and half-wave plate (λ/2) filter (as shown in Figure 5.2), for averagely excited the sample with circularly-polarized light, and I employed the linearly-polarized light to the ReS$_2$ samples, respectively.
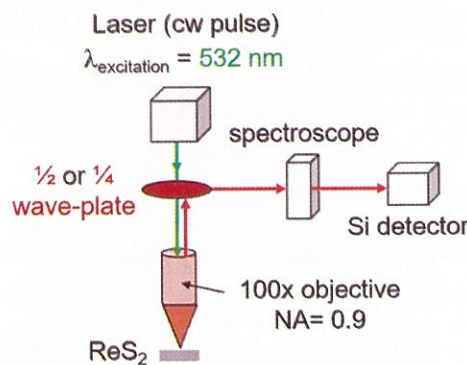
Figure 5.2 Nanophoton optical setup for PL and Raman measurements of ReS$_2$.

5.3.2.   Differential Reflectance Measurements of ReS$_2$

In this thesis, the differential reflectance measurement of ReS2 has been done using two kind of optical setup: (1) using the Nanophoton (as usually used for monolayer TMDs group VI), and (2) by utilizing the optical home-made setup. The former is employed for unpolarized excitation light (which mainly discussed and explained in this chapter), while the latter is employed to confirm the polarization-angle dependent of the anisotropic structure of ReS$_2$.

5.4. Results and Discussion

5.4.1.   Optical Measurements of ReS$_2$
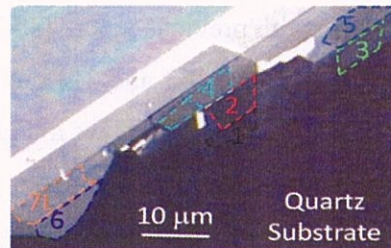
Figure 5.3 Optical image of 1–7L and bulk ReS$_2$ on quartz substrate.

Figure 5.3 show the optical image of 1–7L of ReS$_2$ on quartz, under high magnification of x100 with NA = 0.9. The layer number of ReS$_2$ has been confirmed by analyzing the Raman scattering spectra, as well as by identifying the optical contrast [212] from its optical image. Figure 5.4(a) shows the Raman scattering spectra of monolayer (1L) to few-layer (2–7L) of ReS$_2$ on quartz substrate. There are 5 Raman modes with two pronounced modes detected of III and V mode, as they are respect to the in-plane and out-of-plane vibration of rhenium-sulfur atoms, respectively [44].
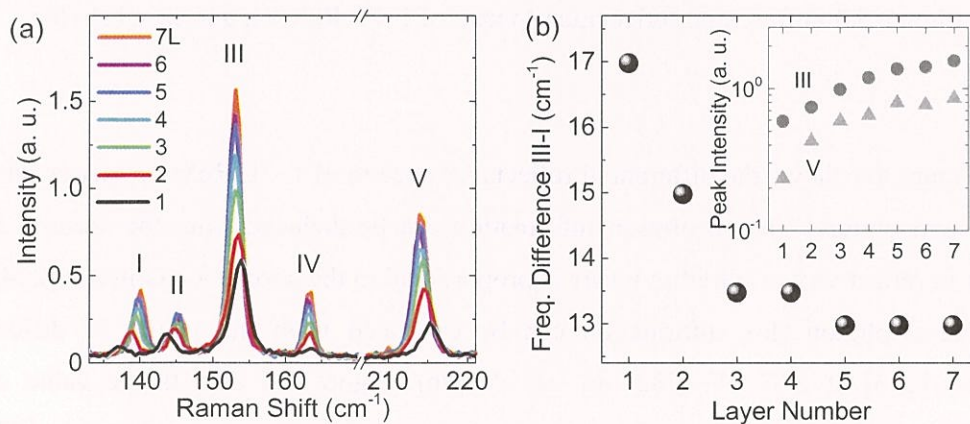
Figure 5.4 (a) Raman spectra of 1–7L at room temperature, (b) Frequency difference between I and III mode; and Inset figure: peak Raman intensity of III and A$_g$-like mode as a function of layer number .

The Raman modes exhibit monotonic increase in I to IV and A_g-like modes for 1–7L. The observed tendency are consistent with previous report [44,213] with the peak positions of III, IV and A_g-like mode is constant at 153, 163 and 214 cm^{-1}, respectively. The frequency difference between I and III modes of 1–7L which shows in Figure 5.4(b) is decrease from 17 to 13 cm^{-1} of Raman shift, is also in agreement with the report [44]. The frequency difference for III-I mode is appointed as a way for characterizing the layer number thickness of ReS_2 samples, as same method applied for monolayer MoS_2 of TMDs using E^1_{2g} and A_{1g} mode [38].
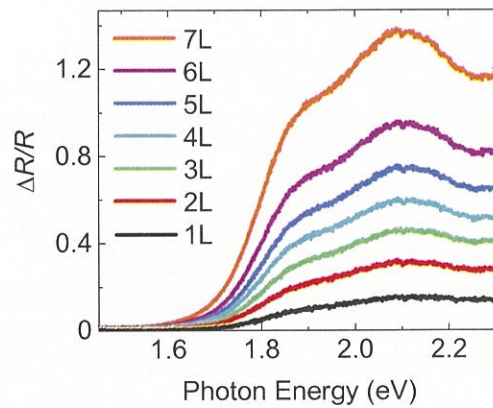
Figure 5.5 Differential reflectance spectra of 1–7L ReS_2 on quartz substrate.

Figure 5.5 shows the differential reflectance spectra of 1–7L ReS_2 on quartz substrate at room temperature. The absorption information can be deduced from the spectra, as the different in reflectivity of ultrathin layers is proportional to the absorption constant [214] thus the absorbed photon flux information can be evaluated from the values of differential reflectance [215] at 2.33 eV (532 nm wavelength). Figure 5.6 depicts the value of the differential reflectance was observed to be identical even the substrate employed is different, and this indicate that the absorption transition for layered ReS_2 is independently to substrate and carrier, but not as PL which commonly affected due to the defect, impurities and carrier.
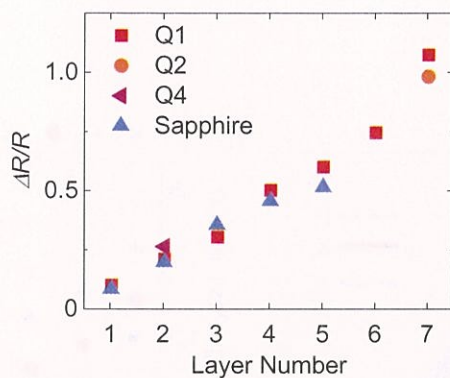
Figure 5.6 The differential reflectance of 1–7L on different substrates, such as quartz (Q) and sapphire.

Figure 5.7 shows the PL spectra of 1–7L (left) and 1–5L (right) ReS$_2$ on quartz and sapphire substrate, respectively, at room temperature using the circularly polarized light. The blue-shift of the PL spectrum as decrease in layer number were noticed with overall PL intensity enhancing consecutively as layer number, and these observation are consistent with earlier reported PL intensities' trend [41]. However, the results of ReS$_2$ is in contrast with that in the atomically thin layer MoS$_2$ [22]. The peak intensity for each PL spectral shape is originated to the peak position of exciton 1, which has greater intensity than exciton 2 and 3 [45], as exhibit in Figure 5.8.
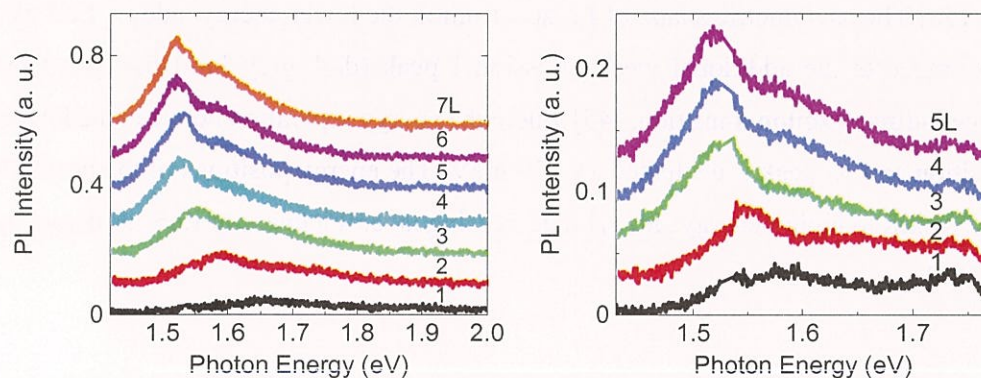
Figure 5.7 PL spectra of 1–7L (left) and 1–5L (right) ReS$_2$ on quartz and sapphire substrate, respectively.
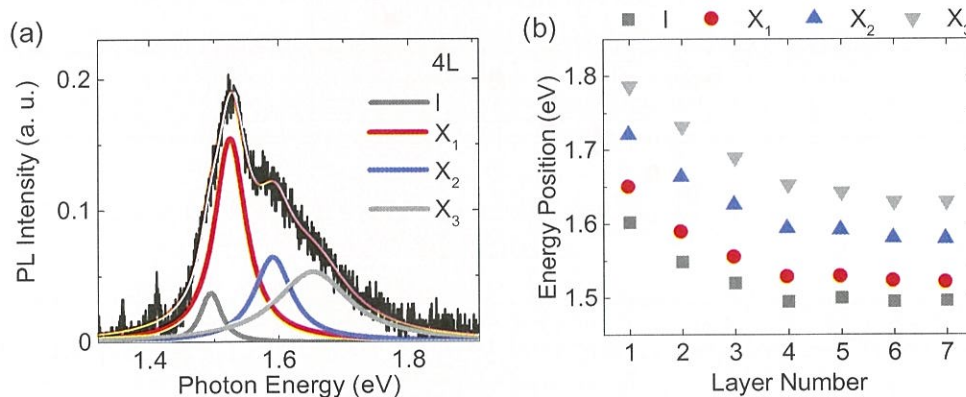
Figure 5.8 PL spectral fitted of 4 layer (4L) ReS$_2$ and the correspond energy position. (a) PL spectral fitted using Voigt function, with I and X indicated by indirect band gap transition, and exciton 1, 2, and 3, respectively, and (b) Energy position of peak I (indirect transition), X$_1$ – X$_3$ (electron-hole pair, exciton emission) of 1–7L ReS$_2$ on quartz substrate.

Figure 5.8 shows the typical PL spectrum of 4L ReS$_2$, and the PL spectrum is decomposed by the several peaks with assuming Voigt functions. [216] The spectrum is reproduced by the X$_1$ (red line) and X$_2$ (blue line) peak arising from emissions of bound electron-hole pair (exciton) confined along and perpendicular to the crystal direction of Re-chain (*b*-axis), respectively, whereas the X$_3$ (grey line) at higher energy side is assigned as the hot PL. [45], [56] The asymmetric shape of PL spectrum in the lower energy side (< 1.55 eV) in Fig. 2 (b) suggests the additional weak emission I peak (dark-grey line) that has been assigned to the indirect exciton transition, [45] where the energy separation between the lowest indirect transition and X$_1$ peak is evaluated as ~ 30 meV. The energy positions of the peaks (I, X$_1$, X$_2$, and X$_3$) shift to higher energy side with decreasing layer thickness of ReS$_2$ as depict by the Figure 5.8(b).

5.4.2. Estimation of PL Quantum Yield and Determination of Band Gap Semiconductor ReS$_2$ at Room Temperature

I further our investigation of the band gap nature of ReS$_2$, by estimating the PL quantum yield of layered ReS$_2$ on transparent substrates using the absolute and relative method of PL

quantum yield [76] using highly emissive standard reference dye of 3-borylbithiophene derivative [166].
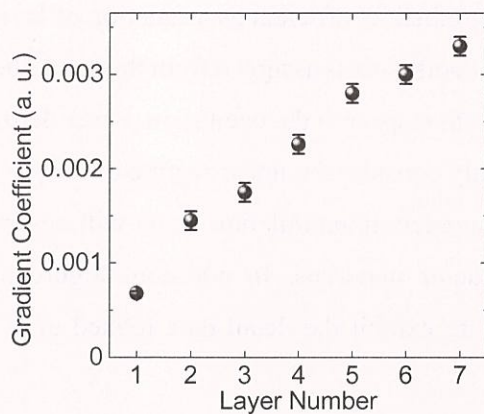
Figure 5.9 Gradient coefficient of 1–7L ReS$_2$ on quartz substrate.
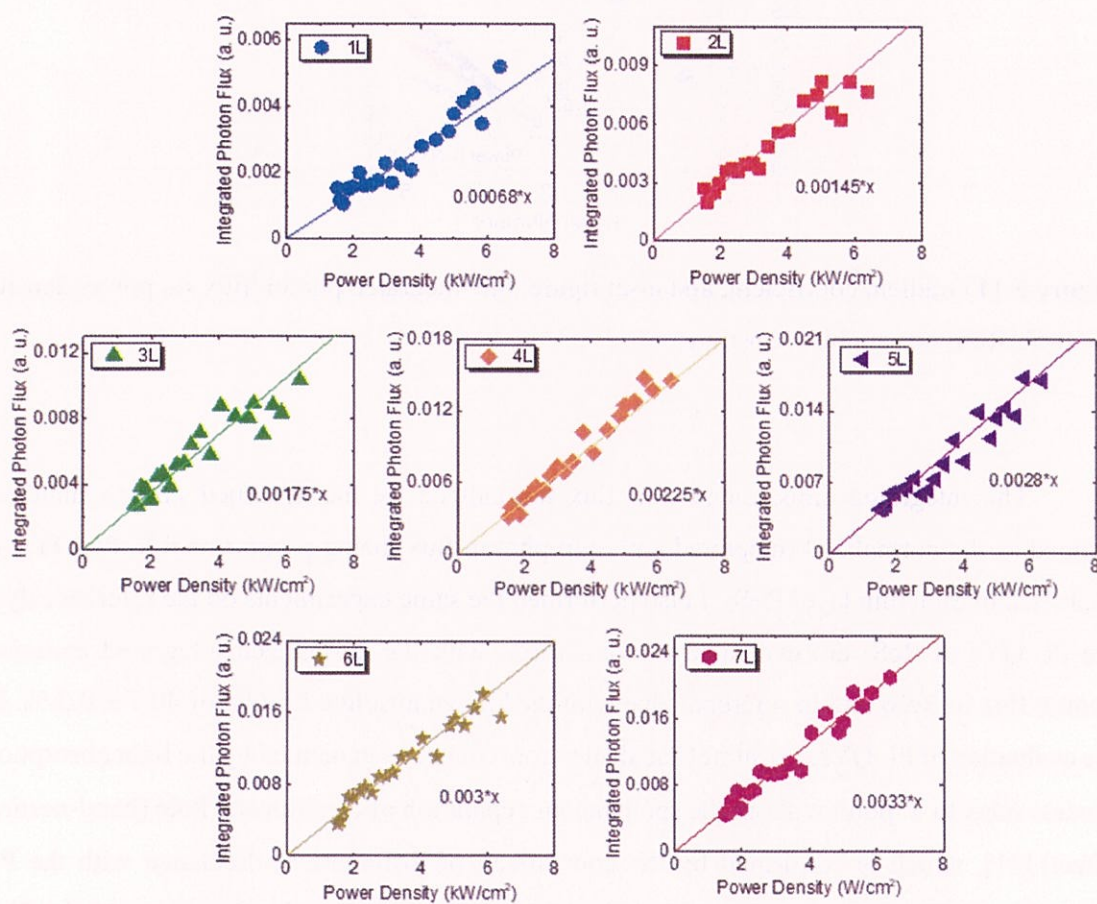
Figure 5.10 Integrated photon flux vs. power density of 1–7L ReS$_2$.

Figure 5.9 shows the gradient coefficient as a function of layer number 1–7L ReS2 on quartz substrate. The gradient coefficient is assigned from the solid line of the integrated photon flux (PL per s per unit area) with respect to the excitation power density, as example shown in Figure 5.10. In this study, I only consider the linear regime of the power excitation supplied to eliminate the effect of exciton-exciton annihilation as its will contribute to non-intrinsic PL quantum yield of semiconductor materials. In addition, Figure 5.11 shows the gradient coefficient with the inset figure exhibit the detail data related of 1–5L of ReS_2 on sapphire substrate.
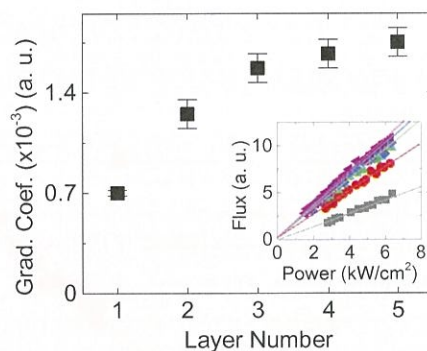
Figure 5.11 Gradient coefficient, and inset figure: the integrated photon flux vs. power density for 1–5L ReS_2 on sapphire substrate.

The integrated emission photon flux normalized by the absorbed photon numbers defined as the normalized integrated emission photon flux, being proportional to PL QYs, is evaluated in each thin layer ReS_2. I also performed the same experiments on the reference dye; the PL QYs of ReS_2 are evaluated in comparison with the normalized integrated emission photon flux in ReS_2 and in reference dye with the known absolute PL QY of 40.7 ± 0.3 %. In the evaluation of PL QYs, I assume that all electron-hole pairs generated by the light absorption process relax to Γ point without the spontaneous separation of electron and hole (band-nesting effect) [31], which is confirmed by the comparison of differential reflectance with the PL excitation (PLE) spectrum as shown in Figure 5.12. The differential reflectance and the PLE spectrum were seen to be matched with each other is indicate that there are no band nesting effect in thin-layered ReS_2 which oppositely observed for monolayer TMDs MX_2 (M = Mo, W; X = S, Se) previously.
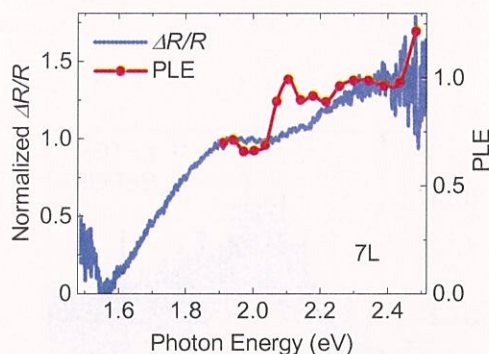
Figure 5.12 Differential reflectance ($\Delta R/R$) (blue line) and PL excitation (PLE) (red circle and line) spectra of 7L ReS_2 on the quartz substrate using the polarized excitation incident light at room temperature. The PLE spectrum is matched to the differential reflectance spectrum.
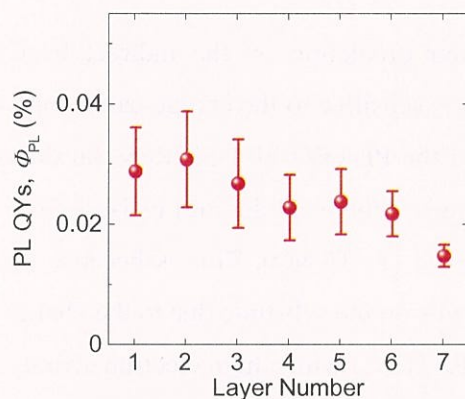
Figure 5.13 Layer number dependence of PL QYs of 1-7L ReS_2 on the quartz substrate.

Figure 5.13 shows the calculated PL QYs of 1-7L ReS_2 on the quartz substrate. The values of PL QYs almost keep constant in a low range from $0.02 – 0.04$ % (10^{-4}) in 1-7L ReS_2. The PL QYs in the order of 10^{-4} in thin layers ReS_2 are more than one-order smaller than those in mechanically exfoliated 1L MX_2 (M=Mo, W; X=S, Se) with direct band gap energy structures [22,195,217]. These experimental results strongly suggest that the thin layers (1-7L) ReS_2 are indirect band gap semiconductors. Noted that the energy structure change from direct to indirect semiconductor in 2L and 1L from the DFT calculation [209] has not been experimentally observed at room temperature.
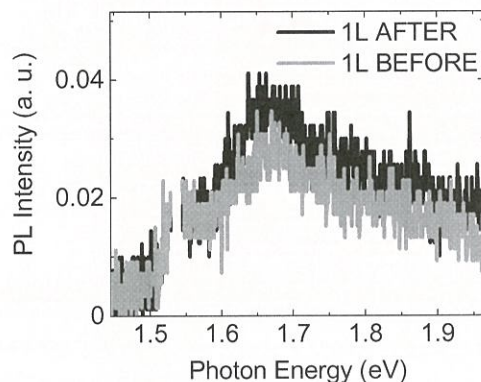
Figure 5.14 PL spectra of monolayer (1L) of ReS$_2$ before and after F$_4$-TCNQ treatment.

In order to validate our prediction on the indirect band gap nature of ReS$_2$, by manipulating the PL QYs that is sensitive to the charge carrier and electronic structure of the material, here I also evaluated the PL QYs of 1-5L ReS$_2$ on different substrates as well as performing the chemical treatment (chemical doping) to 1-5L ReS$_2$ using 2,3,5,6-tetrafluoro-7,7,8,8-tetracyanoquinodimethane (F$_4$-TCNQ). This is because, the thin-layered TMDs has been reported to strongly depends on the substrate due to the charge transfer effect [39], while the chemical doping with the F$_4$-TCNQ with a high electron affinity was reported successfully works as the hole dopant for *n*-type monolayer MoS$_2$ [38]. I noticed that the PL spectrum and its intensity are nearly no change in the 1L ReS$_2$ with a chemical doping of F$_4$-TCNQ (Figure 5.14), whereas those of 1L MoS$_2$ are significantly changed in the same experimental conditions [38].
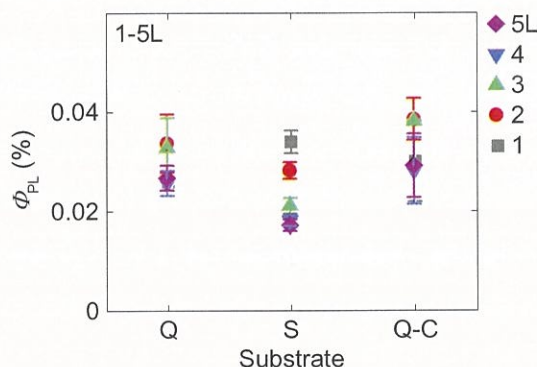
Figure 5.15 the PL QYs of 1-5L ReS$_2$ on the different substrates of quartz (Q), sapphire, Al$_2$O$_3$ (S), and chemically treated using F$_4$-TCNQ on quartz (Q-C).

Table 5.1 Values of PL QYs of 1-5L ReS$_2$ on the different substrates.

Substrate / Layer #	Quartz (Q) (%)	Sapphire, Al$_2$O$_3$ (S) (%)	F$_4$-TCNQ (Q-C) (%)
1	0.026 ± 0.003	0.034 ± 0.002	0.030 ± 0.008
2	0.034 ± 0.006	0.028 ± 0.002	0.038 ± 0.004
3	0.033 ± 0.006	0.021 ± 0.002	0.038 ± 0.001
4	0.026 ± 0.003	0.018 ± 0.001	0.028 ± 0.007
5	0.027 ± 0.002	0.017 ± 0.001	0.029 ± 0.006

The Figure 5.15 shows the summary of evaluated PL QYs of 1-5L ReS$_2$ on the various substrates (quartz, Q and Al$_2$O$_3$, S) and on the quartz with chemical treatment (Q-C). The detail values are shown in Table 5.1. The almost similar value of the reported PL QYs in the range of 0.02 -0.04 % (10^{-4}) of the substrate dependent as shown in Figure 5.15, I suggest that the conduction band minimum at middle of Γ-X point [206] is partially filled, because the thin layers ReS$_2$ is unintentionally n-type doped [203]. However, the mainly observed PL peaks of X$_1$ and X$_2$ are attributed to the recombination of bound electron-hole pairs (excitons) at Γ point [206]. The experimental results of insensitive PL QYs for the modulation of electron density also support the indirect band gap nature of thin layer ReS$_2$.

5.5. Chapter Summary

As a summary of this chapter, I have evaluated the PL QYs of thin layers rhenium disulfide (ReS$_2$) at room temperature by utilizing both the absolute and relative QY methods. The PL QYs in 1-7L ReS$_2$ independent on the layer numbers show the lower values of ~10^{-4} than those in the direct band gap 1L-MX$_2$ (M=Mo, W; X=S, Se). The experimental results of low PL QYs and their almost constant values suggest the indirect band gap electronic structures in 1-7L ReS$_2$. Moreover, the PL QYs being insensitive to the charge carrier transfer and n-type carrier doping also supports the indirect band gap nature of thin layers ReS$_2$. My findings will provide valuable information for the development of the electronic and optical device applications in thin layers ReS$_2$.

Chapter 6.   Summary and Future Outlook

6.1. Summary

In this thesis, I have studied the optical properties of atomically thin-layered two-dimensional (2D) transition metal dichalcogenides (TMDs) of group VI and VII with a chemical formula of MX_2 (M = Mo, W, Re; X = S, Se). Through optical spectroscopic techniques, for instance, photoluminescence (PL), differential reflectance spectra, I have properly evaluated the PL quantum yields (QYs) of monolayer MoS_2, $MoSe_2$, WS_2 and WSe_2, as well as ReS_2 at room temperature.

The PL QYs defined as the ratio of emitted photon numbers to the absorbed photon numbers of semiconductor materials, are very crucial for determination of efficiency and development performance of a semiconductor light-emitting device. In the initial stage, I have developed the evaluation method of PL QYs in the monolayer WSe_2 utilizing both absolute and relative methods using a highly-emissive reference dye of 3-borylbithiophene derivative ($C_{58}H_{49}BN_2S_4$). The reference dye of $C_{58}H_{49}BN_2S_4$ in the PMMA matrix was chosen instead of standard fluorescence reference dye of Rhodemine 6G (R6G) is due to high absolute PL QYs values in the solid form, and the emission wavelength of the dye is matched with the PL emission of monolayer TMDs, MX_2.

I also have determined the effective exciton radiative lifetime of monolayer TMDs at room temperature. The radiative lifetime of elementary excitation, electron-hole pair (exciton) is very important in semiconductor physics as they reflects to the strength of light-matter interaction, and inversely proportional to the oscillator strength of optical transition. In this thesis, I have revealed the exciton radiative lifetime of monolayer MoS_2, $MoSe_2$, WS_2, and WSe_2 of > 10 ns, from the PL QYs of $10^{-2} - 10^{-3}$ and PL decay time of several hundred picosecond, in the basis of long radiative lifetime of bright exciton at low temperature limit, a finite exciton coherence area and the population of dark exciton states.

Moreover, I have determined the indirect band gap nature of thin-layered ReS_2 from mono to seven layers (1 – 7L) at room temperature with employing the PL QYs, where the PL QY is a sensitive probe to the change of electronic structure in a material. The low PL QYs in the range of 10^{-4} independent on the thickness of ReS_2 suggests the indirect band gap nature of

atomically thin ReS_2, which provides the valuable information for the optical applications of atomically thin-layered ReS_2.

6.2. Future Outlook

For future outlook, the developed new method of evaluation PL QY in this study, specifically for atomically thin-layered material can be significant and important to a new thin-layered material with controversial or under debate in research field, either being direct or indirect band gap semiconductor nature. This thus can provide valuable information to determine the specific potential application of the thin-layered material itself to be a good and high efficiency light-emitting device or long-range photodetector which take advantage from the former and latter band gap nature, respectively.

In spite of promising the potential optoelectronic applications, the challenge of atomically thin-layered materials is to understand the fundamental quantum physics behind all the phenomena happens and the characteristic features owned. Thus, the information on intrinsic value such as exciton radiative lifetime of a semiconductor material, is critical to the physical understanding behind the phenomena happen and the special features own by the material itself. Thus, the next development and enhancement in optoelectronic device performance can be achieved and realized. When I can resolve and attain the minimum defect density of atomically thin-layered 2D semiconductor providing the minimum non-radiative decay recombination rate, the information on PL QYs will play essential roles to the accomplishing goals of high performance optical devices application.

Bibliography

[1]   B. Richard and B. Earl, *Nanotechnology for Dummies*, 2nd ed. (Wiley Publishing, 2005).

[2]   K. S. Novoselov, A. K. Geim, S. V. Morozov, D. Jiang, Y. Zhang, S. V. Dubonos, I. V. Grigorieva, and A. A. Firsov, Science (80-.). **306**, 666 (2004).

[3]   C. Berger, Z. Song, T. Li, X. Li, A. Y. Ogbazghi, R. Feng, Z. Dai, N. Alexei, M. E. H. Conrad, P. N. First, and W. A. De Heer, J. Phys. Chem. B **108**, 19912 (2004).

[4]   K. S. Novoselov, A. K. Geim, S. V Morozov, D. Jiang, M. I. Katsnelson, I. V Grigorieva, S. V Dubonos, and A. A. Firsov, Nature **438**, 197 (2005).

[5]   Y. Zhang, Y. Tan, H. L. Stormer, and P. Kim, Nature **438**, 201 (2005).

[6]   J. C. Meyer, A. K. Geim, M. I. Katsnelson, K. S. Novoselov, T. J. Booth, and S. Roth, Nature **446**, 60 (2007).

[7]   S. V. Morozov, K. S. Novoselov, M. I. Katsnelson, F. Schedin, D. C. Elias, J. A. Jaszczak, and A. K. Geim, Phys. Rev. Lett. **100**, (2008).

[8]   K. S. Novoselov and A. H. Castro Neto, Phys. Scr. 14006 (2012).

[9]   B. Radisavljevic, A. Radenovic, J. Brivio, V. Giacometti, and A. Kis, Nat. Nanotechnol. **6**, 147 (2011).

[10] R. S. Sundaram, M. Engel, A. Lombardo, R. Krupke, A. C. Ferrari, P. Avouris, and M. Steiner, Nano Lett. **13**, 1416 (2013).

[11] L. Britnell, R. M. Ribeiro, A. Eckmann, R. Jalil, B. D. Belle, A. Mishchenko, Y. Kim, R. V Gorbachev, T. Georgiou, S. V Morozov, A. N. Grigorenko, A. K. Geim, C. Casiraghi, A. H. C. Neto, and K. S. Novoselov, **340**, (2013).

[12] O. Lopez-Sanchez, E. Alarcon Llado, V. Koman, A. Fontcuberta I Morral, A. Radenovic, and A. Kis, ACS Nano **8**, 3042 (2014).

[13] Z. Wang, Q. Su, G. Q. Yin, J. Shi, H. Deng, J. Guan, M. P. Wu, Y. L. Zhou, H. L. Lou, and Y. Q. Fu, Mater. Chem. Phys. **147**, 1068 (2014).

[14] A. Castellanos-Gomez, J. Phys. Chem. Lett. **6**, 4280 (2015).

[15] G. Eda and S. A. Maier, ACS Nano **7**, 5660 (2013).

[16] M. Chhowalla, H. S. Shin, G. Eda, L.-J. Li, K. P. Loh, and H. Zhang, Nat. Chem. **5**, 263 (2013).

[17] H. Wang, H. Feng, and J. Li, Small **10**, 2165 (2014).

[18] K. S. Novoselov, D. Jiang, F. Schedin, T. J. Booth, V. V Khotkevich, S. V Morozov, and A. K. Geim, Proc. Natl. Acad. Sci. U. S. A. **102**, 10451 (2005).

[19] J. Kang, W. Cao, X. Xie, D. Sarkar, W. Liu, and K. Banerjee, in *Proc. SPIE* (2014), p. 908305.

[20] R. V. Gorbachev, I. Riaz, R. R. Nair, R. Jalil, L. Britnell, B. D. Belle, E. W. Hill, K. S. Novoselov, K. Watanabe, T. Taniguchi, A. K. Geim, and P. Blake, Small 7, 465 (2011).

[21] T. T. Tran, K. Bray, M. J. Ford, M. Toth, and I. Aharonovich, Nat. Nanotechnol. 11, 37 (2016).

[22] K. F. Mak, C. Lee, J. Hone, J. Shan, and T. F. Heinz, Phys. Rev. Lett. 105, 136805 (2010).

[23] Q. Wang, S. Ge, X. Li, J. Qiu, Y. Ji, J. Feng, and D. Sun, ACS Nano 7, 11087 (2013).

[24] A. M. Jones, H. Yu, N. J. Ghimire, S. Wu, G. Aivazian, J. S. Ross, B. Zhao, J. Yan, D. G. Mandrus, D. Xiao, W. Yao, and X. Xu, Nat. Nanotechnol. 8, 634 (2013).

[25] A. Taube, A. Łapińska, J. Judek, and M. Zdrojek, Appl. Phys. Lett. 107, 13105 (2015).

[26] D. Tan, H. E. Lim, F. Wang, N. B. Mohamed, S. Mouri, W. Zhang, Y. Miyauchi, M. Ohfuchi, and K. Matsuda, Nano Res. 10, 546 (2017).

[27] D. Tan, W. Zhang, X. Wang, K. Sandhaya, Y. Miyauchi, and K. Matsuda, Nanoscale 12425 (2017).

[28] A. Castellanos-Gomez, L. Vicarelli, E. Prada, J. O. Island, K. L. Narasimha-Acharya, S. I. Blanter, D. J. Groenendijk, M. Buscema, G. a. Steele, J. V. Alvarez, H. W. Zandbergen, J. J. Palacios, and H. S. J. van der Zant, 2D Mater. 1, 25001 (2014).

[29] H. Liu, A. T. Neal, Z. Zhu, Z. Luo, X. Xu, T. David, and P. D. Ye, ACS Nano 8, 4033 (2014).

[30] L. Zyga, *Scientists Enhance Light Emission in 2D Semiconductors by a Factor of 100* (2013).

[31] D. Kozawa, R. Kumar, A. Carvalho, K. Kumar Amara, W. Zhao, S. Wang, M. Toh, R. M. Ribeiro, A. H. Castro Neto, K. Matsuda, and G. Eda, Nat. Commun. 5, 4543 (2014).

[32] X. Marie and B. Urbaszek, Nat. Mater. 14, 860 (2015).

[33] A. Splendiani, L. Sun, Y. Zhang, T. Li, J. Kim, C. Y. Chim, G. Galli, and F. Wang, Nano Lett. 10, 1271 (2010).

[34] P. Tonndorf, R. Schmidt, R. Schneider, J. Kern, M. Buscema, G. a. Steele, A. Castellanos-Gomez, H. S. J. van der Zant, S. Michaelis de Vasconcellos, and R. Bratschitsch, Optica 2, 347 (2015).

[35] A. C. Ferrari, J. C. Meyer, V. Scardaci, C. Casiraghi, M. Lazzeri, F. Mauri, S. Piscanec, D. Jiang, K. S. Novoselov, S. Roth, and A. K. Geim, Phys. Rev. Lett. 97, 1 (2006).

[36] R. Mas-Ballesté, C. Gómez-Navarro, J. Gómez-Herrero, and F. Zamora, Nanoscale 3,

20 (2011).

[37] H. Li, Q. Zhang, C. C. R. Yap, B. K. Tay, T. H. T. Edwin, A. Olivier, and D. Baillargeat, Adv. Funct. Mater. **22**, 1385 (2012).

[38] S. Mouri, Y. Miyauchi, and K. Matsuda, Nano Lett. **13**, 5944 (2013).

[39] M. Buscema, G. A. Steele, H. S. J. van der Zant, and A. Castellanos-Gomez, Nano Res. **7**, 561 (2014).

[40] A. B. Kaul, J. Mater. Res. **29**, 348 (2014).

[41] S. Tongay, H. Sahin, C. Ko, A. Luce, W. Fan, K. Liu, J. Zhou, Y.-S. Huang, C.-H. Ho, J. Yan, D. F. Ogletree, S. Aloni, J. Ji, S. Li, J. Li, F. M. Peeters, and J. Wu, Nat. Commun. **5**, 3252 (2014).

[42] S. Horzum, D. Çaklr, J. Suh, S. Tongay, Y. S. Huang, C. H. Ho, J. Wu, H. Sahin, and F. M. Peeters, Phys. Rev. B - Condens. Matter Mater. Phys. **89**, 1 (2014).

[43] K. Keyshar, Y. Gong, G. Ye, G. Brunetto, W. Zhou, D. P. Cole, K. Hackenberg, Y. He, L. Machado, M. Kabbani, A. H. C. Hart, B. Li, D. S. Galvao, A. George, R. Vajtai, C. S. Tiwary, and P. M. Ajayan, Adv. Mater. **27**, 4640 (2015).

[44] D. A. Chenet, O. B. Aslan, P. Y. Huang, C. Fan, A. M. van der Zande, T. F. Heinz, and J. C. Hone, Nano Lett. **15**, 5667 (2015).

[45] O. B. Aslan, D. A. Chenet, A. M. Van Der Zande, J. C. Hone, and T. F. Heinz, ACS Photonics **3**, 96 (2016).

[46] I. Gutiérrez-Lezama, B. A. Reddy, N. Ubrig, and A. F. Morpurgo, 2D Mater. **3**, 45016 (2016).

[47] M. Rahman, K. Davey, and S. Z. Qiao, Adv. Funct. Mater. **27**, (2017).

[48] J. C. Wildervanck and F. Jellinek, J. Less-Common Met. **24**, 73 (1971).

[49] K. Friemelt, M.-C. Lux-Steiner, and E. Bucher, J. Appl. Phys. **74**, 5266 (1993).

[50] H. H. Murray, S. P. Kelly, R. R. Chianelli, and C. S. Day, Inorg. Chem. **33**, 4418 (1994).

[51] C. M. Fang, G. A. Wiegers, H. C, and R. A. de Groot, J. Phys. Condens. Matter **9**, 4411 (1997).

[52] C. H. Ho, Y. S. Huang, K. K. Tiong, and P. C. Liao, J. Phys. Condens. Matter **11**, 5367 (1999).

[53] C. H. Ho, P. C. Yen, Y. S. Huang, and K. K. Tiong, J. Phys. Condens. Matter **13**, 8145 (2001).

[54] C. Ho, P. Yen, Y. Huang, and K. Tiong, Phys. Rev. B **66**, 2 (2002).

[55] D. Hou, Y. Ma, J. Du, J. Yan, C. Ji, and H. Zhu, J. Phys. Chem. Solids **71**, 1571 (2010).

[56] L. Der-Yuh, H. Tung-Pai, W. Fan-Lei, L. Chih-Ming, H. Ying-Sheng, and T. Kwong-

Kau, Solid State Phenom. **170**, 135 (2011).

[57] C. H. Ho, Y. S. Huang, K. K. Tiong, and P. C. Liao, Phys. Rev. B **58**, 16130 (1998).

[58] D. Wolverson, S. Crampin, A. S. Kazemi, A. Ilie, and S. J. Bending, ACSNano **8**, 11154 (2014).

[59] L. Hart, S. Dale, S. Hoye, J. L. Webb, and D. Wolverson, Nano Lett. **16**, 1381 (2016).

[60] S. Zhang, N. Mao, N. Zhang, J. Wu, L. Tong, and J. Zhang, ACS Nano **11**, 10366 (2017).

[61] H. Yang, H. Jussila, A. Autere, H.-P. Komsa, G. Ye, X. Chen, T. Hasan, and Z. Sun, ACS Photonics **4**, 3023 (2017).

[62] C. Lee, X. Wei, J. W. Kysar, and J. Hone, Science (80-.). **321**, 385 (2008).

[63] T. Korn, S. Heydrich, M. Hirmer, J. Schmutzler, and C. Schller, Appl. Phys. Lett. **99**, 102109 (2011).

[64] L. Li, Y. Yu, G. J. Ye, Q. Ge, X. Ou, H. Wu, and D. Feng, Nat. Nanotechnol. **9**, 372 (2014).

[65] Y. Zhao, Y. Chen, Y.-H. Zhang, and S.-F. Liu, Mater. Chem. Phys. **189**, 215 (2016).

[66] A. Castellanos-Gomez, Nat. Photonics **10**, 202 (2016).

[67] F. Iyikanat, H. Sahin, R. T. Senger, and F. M. Peeters, APL Mater. **2**, (2014).

[68] K. Matsuda, J. Phys. Soc. Japan **84**, 1 (2015).

[69] G. Wang, A. Chernikov, M. M. Glazov, T. F. Heinz, X. Marie, T. Amand, and B. Urbaszek, arXiv (2017).

[70] A. Ramasubramaniam, Phys. Rev. B **86**, 115409 (2012).

[71] A. Chernikov, T. C. Berkelbach, H. M. Hill, A. Rigosi, Y. Li, O. B. Aslan, D. R. Reichman, M. S. Hybertsen, and T. F. Heinz, Phys. Rev. Lett. **113**, 76802 (2014).

[72] J. S. Ross, P. Klement, A. M. Jones, N. J. Ghimire, J. Yan, M. G., T. Taniguchi, K. Watanabe, K. Kitamura, W. Yao, D. H. Cobden, and X. Xu, Nat Nano **9**, 268 (2014).

[73] L. Yuan and L. Huang, Nanoscale **7**, 7402 (2015).

[74] H. Wang, C. Zhang, and F. Rana, Nano Lett. **15**, 339 (2015).

[75] M. Amani, D.-H. Lien, D. Kiriya, J. Xiao, A. Azcatl, J. Noh, S. R. Madhvapathy, R. Addou, S. Kc, M. Dubey, K. Cho, R. M. Wallace, S.-C. Lee, J.-H. He, J. W. Ager, X. Zhang, E. Yablonovitch, and A. Javey, Science (80-.). **350**, 1065 (2015).

[76] C. Würth, G. Markus, P. Jutta, S. Monika, and U. Resch-Genger, Anal. Chem. **83**, 3431 (2011).

[77] U. Resch-Genger and K. Rurack, Pure Appl. Chem. **85**, 2005 (2013).

[78] A. C. Phillips, *Introduction to Quantum Mechanics* (Wiley Publishing, 2003).

[79] Malrahil, *ICS PHYS: Elementary Excitations in Crystal* (2017).

[80] http://coolchemistrystuff.yolasite.com/, (2008).

[81] B. L. Huetinck and S. Adams, *Quick Review: Physics* (2001).

[82] J. H. Shirley, Phys. Rev. **138**, 979 (1965).

[83] L. Holmes, *Introduction to Nano-Materials* (2015).

[84] R. Angus, in *Mater. Sci. Semicond.* (2008), pp. 21–72.

[85] S. Bremner, *Review of Semiconductors* (2009).

[86] A. Peyghambarian, N., Koch, S. W. & Mysyrowicz, Opt. Laser Technol. (1993).

[87] C. K. Dass, Two-Dimensional Coherent Spectroscopy of Monolayer Transition Metal Dichalcogenides, The University of Texas at Austin, 2015.

[88] M. M. A. Khan, *Chapter 3 : Introduction to the Quantum Theory of Solids* (2016).

[89] S.-Y. Kuo, *Introduction to Photoluminescence Spectroscopy* (2004).

[90] B. Van Zeghbroeck, *Principles of Electronic Devices* (2011).

[91] F. Mark, *Optical Properties of Solids*, 2nd Editio (2010).

[92] D. Kozawa, Behavior of Photocarrier in Atomically Thin Two-Dimensional Semiconducting Materials for Optoelectronics, Kyoto University, Japan, 2015.

[93] K. Skorupska, *Optical Properties of Semiconductors Optical Properties of Semiconductors* (2011).

[94] L. Zhou, Study on the Optical Properties of Atomically Thin Layer Materials WSe2, Kyoto University, Japan, 2015.

[95] M. A. Lampert, Phys. Rev. Lett. **1**, 450 (1958).

[96] A. Singh, G. Moody, K. Tran, M. E. Scott, V. Overbeck, G. Berghäuser, J. Schaibley, E. J. Seifert, D. Pleskot, N. M. Gabor, J. Yan, D. G. Mandrus, M. Richter, E. Malic, X. Xu, and X. Li, Phys. Rev. B **93**, 1 (2016).

[97] Y. You, X.-X. Zhang, T. C. Berkelbach, M. S. Hybertsen, D. R. Reichman, and T. F. Heinz, Nat. Phys. **11**, 477 (2015).

[98] G. Plechinger, P. Nagler, J. Kraus, N. Paradiso, C. Strunk, C. Schüller, and T. Korn, Phys. Status Solidi - Rapid Res. Lett. **9**, 457 (2015).

[99] I. Kylanpaa and H. P. Komsa, Phys. Rev. B **92**, 1 (2015).

[100] C. D. Spataru, S. Ismail-Beigi, R. B. Capaz, and S. G. Louie, Phys. Rev. Lett. **95**, 1 (2005).

[101] S. Chen, M. Yoshita, A. Ishikawa, T. Mochizuki, S. Maruyama, H. Akiyama, Y. Hayamizu, L. N. Pfeiffer, and K. W. West, Sci. Rep. **3**, 1941 (2013).

[102] C. V. RAMAN and K. S. KRISHNAN, Nature **121**, 501 (1928).

[103] C. V. RAMAN and K. S. KRISHNAN, Nature **121**, 711 (1928).

[104] G. S. Bumbrah and R. M. Sharma, Egypt. J. Forensic Sci. **6**, 209 (2016).

[105] J. Kreisel, *Introduction to Raman Scattering* (2014).

[106] S.G.Przhbel'skii, Gt. Sov. Encycl. (1970).

[107] B. Sapkota, *Polarization, Scattering, Absorption of Light* (2015).

[108] N. Manset, *Polarization of Light : Part I : Different Polarization States of Light* (2001).

[109] H. Wang, H. Feng, and J. Li, Small **10**, 2165 (2014).

[110] J. Li, Y. L. Zhong, and D. Zhang, J. Phys. Condens. Matter **27**, 315301 (2015).

[111] Q. H. Wang, K. Kalantar-Zadeh, A. Kis, J. N. Coleman, and M. S. Strano, Nat. Nanotechnol. **7**, 699 (2012).

[112] S. J. McDonnell and R. M. Wallace, Thin Solid Films **616**, 482 (2016).

[113] Y. Ding, Y. Wang, J. Ni, L. Shi, S. Shi, and W. Tang, Phys. B Condens. Matter **406**, 2254 (2011).

[114] W. Zhao, Z. Ghorannevis, L. Chu, M. Toh, C. Kloc, P.-H. Tan, and G. Eda, ACS Nano **7**, 791 (2013).

[115] J. S. Park, A. Reina, R. Saito, J. Kong, G. Dresselhaus, and M. S. Dresselhaus, Carbon N. Y. **47**, 1303 (2009).

[116] H. Zeng and X. Cui, Chem. Soc. Rev. **44**, 2629 (2015).

[117] X. Zhang, X.-F. Qiao, W. Shi, J.-B. Wu, D.-S. Jiang, and P.-H. Tan, Chem. Soc. Rev. **44**, 2757 (2015).

[118] X. Zhang, T. Qing-hai, W. Jiang-bin, S. Wei, and T. Ping-heng, Nanoscale **8**, 6435 (2016).

[119] Y. Lin, X. Ling, L. Yu, S. Huang, A. L. Hsu, Y. H. Lee, J. Kong, M. S. Dresselhaus, and T. Palacios, Nano Lett. **14**, 5569 (2014).

[120] A. R. Kim, Y. Kim, J. Nam, H. S. Chung, D. J. Kim, J. D. Kwon, S. W. Park, J. Park, S. Y. Choi, B. H. Lee, J. H. Park, K. H. Lee, D. H. Kim, S. M. Choi, P. M. Ajayan, M. G. Hahm, and B. Cho, Nano Lett. **16**, 1890 (2016).

[121] C. Lee, H. Yan, L. Brus, T. Heinz, J. Hone, and S. Ryu, ACS Nano **4**, 2695 (2010).

[122] H. Li, J. Wu, Z. Yin, and H. Zhang, Acc. Chem. Res. **47**, 1067 (2014).

[123] H. Li, G. Lu, Y. Wang, Z. Yin, C. Cong, Q. He, L. Wang, F. Ding, T. Yu, and H. Zhang, Small **9**, 1974 (2013).

[124] M. S. Dresselhaus, *Solid State Physics Part II: Optical Properties of Solids* (2001).

[125] K. F. Mak, K. He, C. Lee, G. H. Lee, J. Hone, T. F. Heinz, and J. Shan, Nat. Mater. **12**, 207 (2013).

[126] M. Amani, P. Taheri, R. Addou, G. H. Ahn, D. Kiriya, D. H. Lien, J. W. Ager, R. M.

Wallace, and A. Javey, Nano Lett. **16**, 2786 (2016).

[127] S. Z. Butler, S. M. Hollen, L. Cao, Y. Cui, J. A. Gupta, H. R. Guti??rrez, T. F. Heinz, S. S. Hong, J. Huang, A. F. Ismach, E. Johnston-Halperin, M. Kuno, V. V. Plashnitsa, R. D. Robinson, R. S. Ruoff, S. Salahuddin, J. Shan, L. Shi, M. G. Spencer, M. Terrones, W. Windl, and J. E. Goldberger, ACS Nano **7**, 2898 (2013).

[128] T. C. Berkelbach, M. S. Hybertsen, and D. R. Reichman, Phys. Rev. B **88**, 45318 (2013).

[129] H. Wang, C. Zhang, W. Chan, C. Manolatou, S. Tiwari, and F. Rana, Phys. Rev. B **93**, 45407 (2016).

[130] T. Cheiwchanchamnangij and W. R. L. Lambrecht, Phys. Rev. B **85**, 205302 (2012).

[131] C. Zhang, H. Wang, W. Chan, C. Manolatou, and F. Rana, Phys. Rev. B **89**, 205436 (2014).

[132] D. Y. Qiu, F. H. Da Jornada, and S. G. Louie, Phys. Rev. Lett. **111**, 1 (2013).

[133] S. Sim, J. Park, J. G. Song, C. In, Y. S. Lee, H. Kim, and H. Choi, Phys. Rev. B - Condens. Matter Mater. Phys. **88**, 1 (2013).

[134] D. Lagarde, L. Bouet, X. Marie, C. R. Zhu, B. L. Liu, T. Amand, P. H. Tan, and B. Urbaszek, Phys. Rev. Lett. **112**, 47401 (2014).

[135] S. Mouri, Y. Miyauchi, M. Toh, W. Zhao, G. Eda, and K. Matsuda, Phys. Rev. B **90**, 155449 (2014).

[136] G. Liu, D. Xiao, Y. Yao, X. X. De, W. Yao, and D. Xiao, Chem. Soc. Rev. **44**, 2577 (2015).

[137] J. P. Echeverry, B. Urbaszek, T. Amand, X. Marie, and I. C. Gerber, Phys. Rev. B **93**, 1 (2016).

[138] Y. Li, A. Chernikov, X. Zhang, A. Rigosi, H. M. Hill, A. M. Van Der Zande, D. A. Chenet, E. M. Shih, J. Hone, and T. F. Heinz, Phys. Rev. B **90**, 205422 (2014).

[139] K. P. Dhakal, D. L. Duong, J. Lee, H. Nam, M. Kim, M. Kan, Y. H. Lee, and J. Kim, Nanoscale **6**, 13028 (2014).

[140] W. Yao, D. Xiao, and Q. Niu, Phys. Rev. B **77**, 1 (2008).

[141] D. Xiao, G. Bin Liu, W. Feng, X. Xu, and W. Yao, Phys. Rev. Lett. **108**, 1 (2012).

[142] K. Kosmider, J. W. González, and J. Fernández-Rossier, Phys. Rev. B **88**, 245436 (2013).

[143] X. X. Zhang, Y. You, S. Y. F. Zhao, and T. F. Heinz, Phys. Rev. Lett. **115**, 1 (2015).

[144] A. Carvalho, R. M. Ribeiro, and A. H. Castro Neto, Phys. Rev. B **88**, 115205 (2013).

[145] W. Zhao, R. M. Ribeiro, and G. Eda, Acc. Chem. Res. **48**, 91 (2015).

[146] Z. Fei, B. Wang, C. H. Ho, F. Lin, J. Yuan, Z. Zhang, and C. Jin, Nano Res. **10**, 1 (2017).

[147] X. Wang, A. M. Jones, K. L. Seyler, V. Tran, Y. Jia, H. Zhao, H. Wang, L. Yang, X.

Xu, and F. Xia, Nat. Nanotechnol. **10**, 517 (2015).

[148] X. Wang and S. Lan, Adv. Opt. Photonics **8**, 618 (2016).

[149] A. Ziletti, A. Carvalho, D. K. Campbell, D. F. Coker, and A. H. Castro Neto, Phys. Rev. Lett. **114**, 26 (2015).

[150] J. O. Island, G. A. Steele, H. S. J. van der Zant, and A. Castellanos-Gomez, 2D Mater. **2**, 11002 (2015).

[151] A. Favron, E. Gaufrès, F. Fossard, A.-L. Phaneuf-L'Heureux, N. Y.-W. Tang, P. L. Lévesque, A. Loiseau, R. Leonelli, S. Francoeur, and R. Martel, Nat. Mater. **14**, 826 (2015).

[152] H.-X. Zhong, S. Gao, J. J. Shi, and L. Yang, Phys. Rev. B **92**, 115438 (2015).

[153] R. He, J. A. Yan, Z. Yin, Z. Ye, G. Ye, J. Cheng, J. Li, and C. H. Lui, Nano Lett. **16**, 1404 (2016).

[154] Y. Lin, H. Komsa, C. Yeh, B. Tornjom, L. Zheng-Yong, H. Ching-Hwa, H. Ying-Sheng, C. Po-Wen, A. V. Krasheninnikov, and S. Kazu, ACS Nano **9**, 11249 (2015).

[155] C. Würth, M. Grabolle, J. Pauli, M. Spieles, and U. Resch-genger, Nat. Protoc. **8**, 1535 (2013).

[156] N. C. Greenham, I. D. W. Samuel, G. R. Hayes, R. T. Phillips, Y. A. R. R. Kessener, S. C. Moratti, A. B. Holmes, and R. H. Friend, Chem. Phys. Lett. **241**, 89 (1995).

[157] T. S. Ahn, R. O. Al-Kaysi, A. M. Müller, K. M. Wentz, and C. J. Bardeen, Rev. Sci. Instrum. **78**, 86105 (2007).

[158] K. Suzuki, A. Kobayashi, S. Kaneko, K. Takehira, T. Yoshihara, H. Ishida, Y. Shiina, S. Oishi, and S. Tobita, Phys. Chem. Chem. Phys. **11**, 9850 (2009).

[159] J. Á. Silva-guillén, P. San-jose, and R. Roldán, Appl. Sci. **6**, 284 (2016).

[160] Y. Tsuboi, F. Wang, D. Kozawa, K. Funahashi, S. Mouri, Y. Miyauchi, T. Takenobu, and K. Matsuda, Nanoscale **7**, 14476 (2015).

[161] Y.-M. He, G. Clark, J. R. Schaibley, Y. He, M.-C. Chen, Y.-J. Wei, X. Ding, Q. Zhang, W. Yao, X. Xu, C.-Y. Lu, and J.-W. Pan, Nat. Nanotechnol. **10**, 497 (2015).

[162] A. Srivastava, M. Sidler, A. V. Allain, D. S. Lembke, A. Kis, and A. Imamoğlu, Nat. Nanotechnol. **10**, 491 (2015).

[163] M. Koperski, K. Nogajewski, A. Arora, V. Cherkez, P. Mallet, J.-Y. Veuillen, J. Marcus, P. Kossacki, and M. Potemski, Nat. Nanotechnol. **10**, 503 (2015).

[164] C. Chakraborty, L. Kinnischtzke, K. M. Goodfellow, R. Beams, and a. N. Vamivakas, Nat. Nanotechnol. **10**, 507 (2015).

[165] A. Arora, M. Koperski, K. Nogajewski, J. Marcus, C. Faugeras, and M. Potemski,

Nanoscale **7**, 10421 (2015).

[166] A. Wakamiya, K. Mori, and S. Yamaguchi, Angew. Chemie Int. Ed. **46**, 4273 (2007).

[167] R. Lv, J. A. Robinson, R. E. Schaak, D. Sun, Y. Sun, T. E. Mallouk, and M. Terrones, Acc. Chem. Res. **48**, 56 (2015).

[168] G. Eda, Y. Y. Lin, C. Mattevi, H. Yamaguchi, H. A. Chen, I. S. Chen, C. W. Chen, and M. Chhowalla, Adv. Mater. **22**, 505 (2010).

[169] R. Zondervan, F. Kulzer, S. B. Orlinskii, and M. Orrit, J. Phys. Chem. A **107**, 6770 (2003).

[170] R. Sasai, N. Iyi, T. Fujita, F. L. Arbeloa, V. M. Martínez, K. Takagi, and H. Itoh, Langmuir **20**, 4715 (2004).

[171] T. O. Kaariainen, D. C. Cameron, and M. Tanttari, Plasma Process. Polym. **6**, 631 (2009).

[172] R. Katoh, K. Suzuki, A. Furube, M. Kotani, and K. Tokumaru, J. Phys. Chem. C **113**, 2961 (2009).

[173] T. C. Berkelbach, M. S. Hybertsen, and D. R. Reichman, Phys. Rev. B - Condens. Matter Mater. Phys. **88**, 1 (2013).

[174] E. H. Bogardus and H. B. Bebb, Phys. Rev. **176**, 993 (1968).

[175] G. Bastard, E. E. Mendez, L. L. Chang, and L. Esaki, Phys. Rev. B **26**, 1974 (1982).

[176] L. Johnson, S. K. Emil, and O. V. M., Phys. Rev. B **33**, 5512 (1986).

[177] J. S. Ross, S. Wu, H. Yu, N. J. Ghimire, A. M. Jones, G. Aivazian, J. Yan, D. G. Mandrus, D. Xiao, W. Yao, and X. Xu, Nat. Commun. **4**, 1474 (2013).

[178] Z. Yin, H. Li, H. Li, L. Jiang, Y. Shi, Y. Sun, G. Lu, Q. Zhang, X. Chen, and H. Zhang, ACS Nano **6**, 74 (2012).

[179] O. Lopez-Sanchez, D. Lembke, M. Kayci, A. Radenovic, and A. Kis, Nat. Nanotechnol. **8**, 497 (2013).

[180] X. Liu, T. Galfsky, Z. Sun, F. Xia, and E. Lin, Nat. Photonics **9**, 30 (2015).

[181] R. Gillen and J. Maultzsch, IEEE J. Sel. Top. Quantum Electron. **23**, 9000512 (2016).

[182] PicoQuant, Www.picoquant.com (n.d.).

[183] T. Kato and T. Kaneko, ACS Nano **8**, 12777 (2014).

[184] N. Dong, Y. Li, Y. Feng, S. Zhang, X. Zhang, C. Chang, J. Fan, L. Zhang, and J. Wang, Sci. Rep. **5**, 14646 (2015).

[185] J. J. Olivero and R. L. Longbothum, J. Quant. Spectrosc. Radiat. Transf. **17**, 233 (1977).

[186] S. Koirala, S. Mouri, Y. Miyauchi, and K. Matsuda, Phys. Rev. B **93**, 75411 (2016).

[187] M. Selig, G. Berghäuser, A. Raja, P. Nagler, C. Schüller, T. F. Heinz, T. Korn, A. Chernikov, E. Malic, and A. Knorr, Nat. Commun. **7**, 13279 (2016).

[188] G. Moody, C. Kavir Dass, K. Hao, C.-H. Chen, L.-J. Li, A. Singh, K. Tran, G. Clark, X. Xu, G. Berghäuser, E. Malic, A. Knorr, and X. Li, Nat. Commun. **6**, 8315 (2015).

[189] P. Dey, J. Paul, Z. Wang, C. E. Stevens, C. Liu, A. H. Romero, J. Shan, D. J. Hilton, and D. Karaiskaj, Phys. Rev. Lett. **116**, 127402 (2016).

[190] S. Mouri, Y. Miyauchi, and K. Matsuda, Appl. Phys. Express **9**, (2016).

[191] G. Wang, L. Bouet, D. Lagarde, M. Vidal, A. Balocchi, T. Amand, X. Marie, and B. Urbaszek, Phys. Rev. B **90**, 75413 (2014).

[192] B. Zhu, X. Chen, and X. Cui, Sci. Rep. **5**, 9218 (2015).

[193] J. Feldmann, G. Peter, E. O. Gobel, P. Dawson, K. Moore, C. Foxon, and R. J. Elliott, Phys. Rev. Lett. **59**, 2337 (1987).

[194] Y. Miyauchi, H. Hirori, K. Matsuda, and Y. Kanemitsu, Phys. Rev. B **80**, 081410(R) (2009).

[195] C. Jin, J. Kim, K. Wu, B. Chen, E. S. Barnard, J. Suh, Z. Shi, S. G. Drapcho, J. Wu, P. J. Schuck, S. Tongay, and F. Wang, Adv. Funct. Mater. **27**, 1601741 (2017).

[196] M. Palummo, M. Bernardi, and J. C. Grossman, Nano Lett. **15**, 2794 (2015).

[197] T. Takagahara, Solid State Com **78**, 279 (1991).

[198] C. Robert, D. Lagarde, F. Cadiz, G. Wang, B. Lassagne, T. Amand, A. Balocchi, P. Renucci, S. Tongay, B. Urbaszek, and X. Marie, Phys. Rev. B **93**, 205423 (2016).

[199] T. Godde, D. Schmidt, J. Schmutzler, M. Aßmann, J. Debus, F. Withers, E. M. Alexeev, O. Del Pozo-Zamudio, O. V. Skrypka, K. S. Novoselov, M. Bayer, and A. I. Tartakovskii, Phys. Rev. B **94**, 165301 (2016).

[200] K. Friemelt, L. Kulikova, L. Kulyuk, a. Siminel, E. Arushanov, C. Kloc, and E. Bucher, J. Appl. Phys. **79**, 9268 (1996).

[201] C. H. Ho, P. C. Liao, Y. S. Huang, T. R. Yang, and K. K. Tiong, J. Appl. Phys. **81**, 6380 (1997).

[202] C. H. Ho and C. E. Huang, J. Alloys Compd. **383**, 74 (2004).

[203] E. Liu, Y. Fu, Y. Wang, Y. Feng, H. Liu, X. Wan, W. Zhou, B. Wang, L. Shao, C.-H. Ho, Y.-S. Huang, Z. Cao, L. Wang, A. Li, J. Zeng, F. Song, X. Wang, Y. Shi, H. Yuan, H. Y. Hwang, Y. Cui, F. Miao, and D. Xing, Nat. Commun. **6**, 6991 (2015).

[204] M. Hafeez, L. Gan, H. Li, Y. Ma, and T. Zhai, Adv. Funct. Mater. **26**, 4551 (2016).

[205] H. Tian, J. Tice, R. Fei, V. Tran, X. Yan, L. Yang, and H. Wang, Nano Today **11**, 763 (2016).

[206] Q. Zhao, Y. Guo, Y. Zhou, X. Xu, Z. Ren, J. Bai, and X. Xu, J. Phys. Chem. C **121**, 23744 (2017).

[207] R. Mitra, B. Jariwala, A. Bhattacharya, and A. Das, Nanotechnology **29**, 145706 (2018).

[208] C. Würth, D. Geißler, and U. Resch-Genger, Zeitschrift Fur Phys. Chemie **229**, 153 (2015).

[209] M. Gehlmann, I. Aguilera, G. Bihlmayer, S. Nemšák, P. Nagler, P. Gospodarič, G. Zamborlini, M. Eschbach, V. Feyer, F. Kronast, E. Młyńczak, T. Korn, L. Plucinski, C. Schüller, S. Blügel, and C. M. Schneider, Nano Lett. **17**, 5187 (2017).

[210] F. Liu, S. Zheng, X. He, A. Chaturvedi, J. He, W. L. Chow, T. R. Mion, X. Wang, J. Zhou, Q. Fu, H. J. Fan, B. K. Tay, L. Song, R. H. He, C. Kloc, P. M. Ajayan, and Z. Liu, Adv. Funct. Mater. **26**, 1169 (2016).

[211] M. Zhao, W. Zhang, M. Liu, C. Zou, K. Yang, Y. Yang, Y. Dong, L. Zhang, and S. Huang, Nano Res. **9**, 3772 (2016).

[212] M. M. Benameur, B. Radisavljevic, J. S. Héron, S. Sahoo, H. Berger, and A. Kis, Nanotechnology **22**, 125706 (2011).

[213] E. Lorchat, G. Froehlicher, and S. Berciaud, ACS Nano **10**, 2752 (2016).

[214] K. F. Mak, M. Y. Sfeir, Y. Wu, C. H. Lui, J. A. Misewich, and T. F. Heinz, Phys. Rev. Lett. **101**, 196405 (2008).

[215] N. B. Mohamed, F. Wang, H. E. Lim, W. Zhang, S. Koirala, S. Mouri, Y. Miyauchi, and K. Matsuda, Phys. Status Solidi **254**, 1600563 (2017).

[216] J. J. Olivero and R. L. Longbothum, J. Quant. Spectrosc. Radiat. Transf. **17**, 233 (1977).

[217] N. B. Mohamed, H. E. Lim, F. Wang, S. Koirala, S. Mouri, K. Shinokita, Y. Miyauchi, and K. Matsuda, Appl. Phys. Express **11**, 15201 (2018).

[218] I. Pelant and J. Valenta, *Luminescence Spectroscopy of Semiconductors* (2012).

Scientific Contributions

The name of the author is bold and underlined.

Peer-Reviewed Articles

1. **<u>Nur Baizura Mohamed</u>**, Keisuke Shinokita, Hong En Lim, Dezhi Tan, Yuhei Miyauchi, and Kazunari Matsuda, "Photoluminescence Quantum Yields for Atomically Thin-Layered ReS_2: Identification of Indirect Band Gap Semiconductors", *submitted.*

2. **<u>Nur Baizura Mohamed</u>**, Hong En Lim, Feijiu Wang, Sandhaya Koirala, Shinichiro Mouri, Keisuke Shinokita, Yuhei Miyauchi, and Kazunari Matsuda, "Long Radiative Lifetimes of Excitons in Monolayer Transition-Metal Dichalcogenides MX_2 (M = Mo, W; X = S, Se)", *Applied Physics Express* **2018**, 11, 015201.

3. Fengjiu Yang, Hong En Lim, Feijiu Wang, Masashi Ozaki, Jiewei Liu, **<u>Nur Baizura Mohamed</u>**, Keisuke Shinokita, Yuhei Miyauchi, Atsushi Wakamiya, Yasujiro Murata, and Kazunari Matsuda, "Roles of Polymer Layer in Enhanced Photovoltaic Performance of Perovskite Solar Cells via Interface Engineering", *Advanced Material Interfaces* **2017**, 131, 1701256.

4. **<u>Nur Baizura Mohamed</u>**, Feijiu Wang, Hong En Lim, Wenjin Zhang, Sandhaya Koirala, Shinichiro Mouri, Yuhei Miyauchi, and Kazunari Matsuda, "Evaluation of Photoluminescence Quantum Yield of Monolayer WSe_2 using Reference Dye of 3-Borylbithiophene Derivative", *Physica Status Solidi B: Solid State Physics* **2017**, 254 (2), 1600563.

5. Dezhi Tan, Hong En Lim, Feijiu Wang, **<u>Nur Baizura Mohamed</u>**, Shinichiro Mouri, Wenjin Zhang, Yuhei Miyauchi, Mari Ohfuchi, and Kazunari Matsuda, "Anisotropic Optical and Electronic Properties of Two-Dimensional Layered Germanium Sulfide", *Nano Research* **2017**, 10 (2), 546-555.

Conference Presentations

International Conferences

1. **Nur Baizura Mohamed**, Feijiu Wang, Sandhaya Koirala, Hong En Lim, Shinichiro Mouri, Yuhei Miyauchi, and Kazunari Matsuda, "Photoluminescence Quantum Yield and Long Exciton Radiative Lifetime in Monolayer Two-Dimensional Transition Metal Dichalcogenides", *The 43ʳᵈ International Symposium on Compound Semiconductors (ISCS)*, TuC4-5, Toyama International Conference Center, Toyama, Japan, 26th – 30th June 2016 (Oral).

2. **Nur Baizura Mohamed**, Yuhei Miyauchi, and Kazunari Matsuda, "Fundamental Study of Novel Atomically Thin-Layered Materials", *Japan-UK Seminar on Energy Materials and Sciences*, University of Oxford, United Kingdom, 25th – 26th February 2016 (Oral).

Local Conferences

1. **Nur Baizura Mohamed**, Feijiu Wang, Sandhaya Koirala, Hong En Lim, Shinichiro Mouri, Yuhei Miyauchi, and Kazunari Matsuda, "Photoluminescence Quantum Yield and Effective Exciton Radiative Lifetime in Monolayer Transition Metal Dichalcogenides", *The 77ᵗʰ Japan Society Applied Physics (JSAP) Autumn Meeting*, E 13p-A37-7, Toki Messe, Niigata Convention Center, Niigata, Japan, 13th – 16th September 2016 (Oral).

2. **Nur Baizura Mohamed**, Feijiu Wang, Sandhaya Koirala, Hong En Lim, Shinichiro Mouri, Yuhei Miyauchi, and Kazunari Matsuda, "Photoluminescence Quantum Yield and Exciton Radiative Lifetime in Monolayer WSe$_2$", *The 50ᵗʰ Fullerences-Nanotubes-Graphene General Symposium (FNTG)*, 2P-44, University of Tokyo, Ito International Research Center, Tokyo, Japan, 20th – 22nd February 2016 (Poster).

3. **Nur Baizura Mohamed**, Feijiu Wang, Shinichiro Mouri, Sandhaya Koirala, Yuhei Miyauchi, and Kazunari Matsuda, "Bound Exciton Emission in Photoluminescence Spectrum of Monolayer WSe$_2$", *The 49ᵗʰ Fullerences-Nanotubes-Graphene General Symposium (FNTG)*, 1P-31, Kitakyushu International Conference Center, Fukuoka, Japan, 7th – 9th September 2015 (Poster).

Acknowledgements

Firstly, I would like to thanks to Ministry of Higher Education Malaysia (KPT) and Universiti Teknologi MARA (UiTM) Malaysia for the scholarship and scheme sponsor throughout my three years Ph.D. study in Kyoto University, Japan.

My deeply gratitude is express to my supportive advisor, Professor Kazunari Matsuda for all his guidance and advice ever since I am not yet officially become his student, and also because of his acceptance, then I am here to receive an honor chance to further my study under his supervision, thus gain valuable life experiences in Japan.

I'd also like to exhibit my great appreciation to Professor Yuhei Miyauchi and Professor Keisuke Shinokita for sharing their good comprehension and insight knowledges about physics and nanomaterials. Highly thanks to my best home-country companion, Dr. Hong En Lim who always be my critical reader and spontaneous ideas generator. My pleasure also goes to my current and former group members; Dr. Shinichiro Mouri, Dr. Daichi Kozawa, Dr. Feijiu Wang, Dr. Dezhi Tan and Dr. Sandhaya Koirala for sharing experiences and expertise in their research field, I had grateful help and cooperation with the students, Saki Okudaira who consistently be my *Nihongo* interpreter, Wenjin Zhang, Xiaofan Wang, Takao Yamaoka, Fengju Yang, Masafumi Shimasaki, Kengo Hachiya, Ken Kiyama, Shohei Yanagawa, Yusuke Hasegawa, Shun Aota, Takashi Nakamura and the members from Professor Tatsuya Hinoki's group. I would like to thanks also to Shiori Fujiwara and Reine Sakamoto who kindly take a good care of the administrative things.

Last but not least, my significant dedication to my lovely husband, Mohd Fadli Mokhtar and my adorable daughter, Nur Amna Fahima Mohd Fadli who always be by my side along the hardness and enjoyable time in Japan, and to all my friends and members of my big family, especially to my late father, Mohamed Abdullah, for their love and encouragement.

Terima kasih Allah.

Nur Baizura Mohamed
ヌール バイズーラ ビンティ モハメド
MAY 2018